One Ring to Find Them All

Detection and Separation of Rotating Acoustic Features with Circular Microphone Arrays

vorgelegt von
Dipl.-Ing.
Gert Herold
ORCID: 0000-0001-5284-051X

an der Fakultät V – Verkehrs- und Maschinensysteme
der Technischen Universität Berlin
zur Erlangung des akademischen Grades

Doktor der Ingenieurwissenschaften
– Dr.-Ing. –

genehmigte Dissertation

Promotionsausschuss:

Vorsitzender: Prof. Dr.-Ing. Paul Uwe Thamsen
Gutachter: Prof. Dr.-Ing. Ennes Sarradj
Univ.-Prof. Dr. techn. Dr. h.c. Manfred Kaltenbacher

Tag der wissenschaftlichen Aussprache: 1. November 2021

Berlin 2021

Abstract

Sound emissions by rotating machinery are often connected to rotating acoustic sources. Efficient control of these emissions – whether by simply reducing them or by shaping their spectral characteristics – requires knowledge about the underlying sound generating mechanisms as well as the contribution of separate sources to the total radiation. The detection of sound sources is subject of ongoing research. In the presence of multiple sources, using microphone array methods for their spatial separation is state of the art.

In this thesis, several novel data processing methods are presented whose application provides new insights based on acoustic measurements with circular array arrangements. Aside from the localization of rotating sound sources, it is shown how these measurements can be used for the detection of occurring rotational speeds and for the isolation of different spectral characteristics. Most importantly, the presented data processing allows the separation of acoustic features even if multiple sources with different rotational speeds are present in one data set.

The general applicability of the methods and their limitations are investigated with the help of simulated acoustic data. For demonstrating their practical capabilities, two experimental setups featuring axial fans are evaluated: one with a microphone ring array measuring the sound radiated into a freefield and the other with a ring of wall-mounted microphones within a cylindrical duct. It is shown that with the new methods, previously inaccessible knowledge about present acoustic sources and the underlying sound generating mechanisms can be gained.

Kurzfassung

Die Schallabstrahlung rotierender Maschinen steht häufig im Zusammenhang mit rotierenden Schallquellen. Eine effiziente Beeinflussung der Emissionen – sei es deren bloße Reduktion oder eine gezielte Veränderung der spektralen Charakteristika – setzt die Kenntnis von zugrundeliegenden Schallentstehungsmechanismen und des Anteils einzelner Quellen an der Gesamtabstrahlung voraus. Schallquellendetektion ist Gegenstand aktueller Forschung. Bei Vorhandensein mehrerer Quellen ist der Einsatz von Mikrofonarrayverfahren für deren räumliche Trennung Stand der Technik.

In der vorliegenden Arbeit werden mehrere neuartige Datenverarbeitungsmethoden vorgestellt, deren Anwendung neue Erkenntnisse auf Basis akustischer Messungen mit ringförmigen Array-Anordnungen liefert. Neben der Lokalisierung von rotierenden Schallquellen wird gezeigt, wie diese Messungen zur Detektion auftretender Rotationsgeschwindigkeiten und zur Trennung unterschiedlicher spektraler Anteile genutzt werden können. Vor allem aber ist die Trennung akustischer Merkmale mithilfe der vorgestellten Datenverarbeitungsschritte auch dann möglich, wenn mehrere Quellen mit unterschiedlichen Rotationsgeschwindigkeiten in einem Datensatz auftreten.

Mit Hilfe simulierter akustischer Daten werden die generelle Anwendbarkeit der Methoden sowie deren Grenzen untersucht. Zur Demonstration der Praxistauglichkeit werden zwei Versuche mit Axialventilatoren ausgewertet. Im ersten wird die Schallabstrahlung ins Freifeld mit einem darin befindlichen Mikrofonringarray ausgewertet. Im zweiten Versuch wird das Schallfeld in einem zylindrischen Strömungskanal mit einem Ring aus wandbündigen Mikrofonen gemessen. Es wird gezeigt, dass mit den neuen Methoden bislang unzugängliche Informationen über die vorhandenen Schallquellen und die zugrundeliegenden Schallentstehungsmechanismen gewonnen werden können.

Danke

An Professor Ennes Sarradj,
für das Vertrauen in meine Ideen,
die vielen Freiheiten und die
hilfreichen Wegweiser.

An Professor Manfred Kaltenbacher,
für die Begutachtung der Arbeit und
die angenehme Diskussion in der
wissenschaftlichen Aussprache.

An Professor Paul Uwe Thamsen,
für den Vorsitz im
Promotionsausschuss
und die schwerste Frage ☺.

An ebm-papst Mulfingen,
besonders Marc Schneider,
Erik Reichert und Jürgen Schöne,
für die ersten zwei Jahre mit
rotierenden Schallquellen und den
fortwährenden Informationsaustausch.

An meine Kollegen in Cottbus
und Berlin, für die spannenden
gemeinsamen Projekte, die
gegenseitige Hilfsbereitschaft
und das tolle Arbeitsklima.

An Florian Krömer,
für zwei unglaublich
ergiebige Messtage, mit
Schallgeschwindigkeiten
von manchmal über 350 $\frac{m}{s}$.

An Benjamin Pardowitz,
Maximilian Behn und Ulf Tapken,
für die Kanalmessdaten und die
Datenverarbeitungsansätze.

An Christof Ocker,
für die spannenden Gespräche
über Moden und Matrizen.

An Christine und Bernd Herold,
für ihre Unterstützung in allen
Lebenslagen.

An Vroni, Jakob und Marlene,
für ihre Geduld, ihre Hilfe,
ihre Neugier, ihre Liebe.

Contents

Nomenclature

Acronyms

...-M	... in the mode domain
...-S	... in the spatial domain
BPF	blade passing frequency
CLEAN-SC	high-resolution array algorithm
CSM	cross-spectral matrix
DFT	discrete Fourier transform
DRAP	CSM diagonal reconstruction using alternating projections
DREF	CSM diagonal reconstruction through energy fitting
FFT	fast DFT (*fast Fourier transform*)
PSF	point spread function
RMS	root mean square (quadratic mean)
RSD	rotational speed detection
SNR	signal-to-noise ratio
VPF	vane passing frequency
VRA	virtual rotating array (method)

Latin letters

a, b	two arbitrary mode indices
A_f	amplitude in the rotational speed spectrum
B	number of fan rotor blades
c	speed of sound
$\boldsymbol{C}$	cross-spectral matrix
$\boldsymbol{C}_{\mathrm{abs}}$	matrix with magnitudes of CSM
$\boldsymbol{C}_{\mathrm{th},(n)}$	de-noised magnitude-CSM iteration step
$\boldsymbol{d}$	main diagonal of CSM
$d_{[\mathrm{something}]}$	diameter of [something]
f	frequency
f	frequency index
f_{mod}	rotational speed modulation frequency
f_{rot}	rotational speed
f_{s}	sampling frequency
$f_{\circlearrowleft} / f_{\circlearrowright}$	frequency in the rotating/stationary reference frame (mode domain)
$\mathcal{F}_f$	temporal Fourier transform
$\mathcal{F}_m$	spatial Fourier transform

g_l	microphone weighting factor
$\boldsymbol{h}$	steering vector
$\boldsymbol{h}_{l/m}$	steering vector in spatial/mode domain
j	imaginary unit
K	number of blocks for CSM averaging
l	microphone index
$l_{\circlearrowleft}/l_{\text{⏻}}$	microphone index in the rotating/stationary reference frame
L_p	sound pressure level
M	number of microphones
m	mode index
Ma	Mach number
N_s	number of time samples
p	sound pressure
$\boldsymbol{p}_{l/m}$	vector with sound pressures at microphones/in modes
p_out	sound pressure from beamforming
p_rot	sound pressure at a channel in the rotating reference frame
$r_{s,0}$	distance between focus point and reference position
$r_{s,l}$	distance between focus point and microphone
r_source	radial position of a sound source
s	focus point index
t	time
$\mathfrak{t}$	time sample index
u	DREF initial diagonal normalization factor
V	number of fan stator vanes
$\dot{V}$	volume flow
w	weighting factor for interpolation between microphone signals
$\boldsymbol{x}_l$	microphone position
$\boldsymbol{x}_s$	focus point position

Greek letters

γ_{ij}	CSM coherence
$\gamma_{P_{1\%}}$	first percentile (lowest values) of all coherences in a CSM
Δf_rot	rotational speed modulation amplitude
$\Delta L_{p,4}$	level difference of source 4 to the other sources
$\Delta L_{p,\mathrm{s}}$	specific level error
$\Delta t_{s,0}$	sound travel time from focus point to reference position
$\Delta t_{s,l}$	sound travel time from focus point to microphone
Δm	difference between two mode indices
λ	wave length
$\boldsymbol{\sigma}$	uncorrelated noise in the signals
φ	angular position / rotation angle
Φ	flow rate coefficient

0. Introduction

Rotating technical devices have become an indispensable part of our everyday lives. From household appliances, fans, motors and gearboxes to wind turbines and turbofan engines. And wherever rotating components are not encapsulated and interact with the environment, sound sources occur that also rotate. Often, sound generated in this way is undesirable and perceived as noise.

The best way to avoid noise pollution is to take primary measures, i. e. to prevent the generation of noise through suitable modifications. To design these efficiently, knowledge of the underlying physical mechanisms is necessary. For their identification and evaluation, it is advantageous to know the emission locations of the sound sources and, in the case of the occurrence of multiple sources, their respective characteristics. This information is not only helpful for a better understanding of noise generation, but also for identifying effective measures to prevent it.

For spatial separation of sound sources and characterization of sources in noisy environments, the use of signal processing methods based on synchronous measurements with multiple acoustic sensors, i. e. microphone arrays, has become standard. Applying such methods is appropriate when several sound sources occur simultaneously in a sound field. Methods such as beamforming [1] make it possible to discern important acoustic features, e. g. the distribution of sound sources and their individual spectral characteristics, which would remain hidden if measured with only a single sensor. Typical applications include measurements in engine test beds and wind tunnels, or, in the case of moving sources, vehicle pass-by and aircraft fly-over as well as wind turbine measurements [2].

Sound generation in rotating machinery such as axial fans has been subject of extensive research for several decades. Initially, the underlying mechanisms were mostly discussed based on theoretical considerations and evaluations of single-microphone measurements [3, 4]. In recent years, advanced array measuring techniques have been developed which allow the direct visualization of rotating phenomena previously only measured indirectly or described in theory [5–7]. The working principle relies on creating virtually rotating microphones based on a circular array of physical microphones, thus transforming sources rotating at a known speed into a stationary reference frame for further investigation. The *virtual rotating array* (VRA) method has been proven to be a valuable data evaluation tool in numerous applications [8–13].

However, it has been shown that the applicability of VRA algorithms is subject to limitations, e. g. with respect to the frequency range that can be evaluated [14–16]. Furthermore, although this method can transform data into different rotating reference frames, the totality of the data does not change. This means that, for instance, previously stationary sources are included in the data set as rotating sources after virtual rotation. The interpretation of evaluation results becomes even more complicated for cases in which multiple rotational speeds – which may not even all be documented – occur during a measurement.

The advancement and a better understanding of these aspects of the virtual rotating array method are the subject of this thesis. This leads to the following research questions:

1. What are the conditions under which the virtual rotating array method is suitable for observing rotating sources?
2. How can occurring rotational speeds be determined on the basis of acoustic array measurement data?
3. For sources with differing rotational speeds in a data set, how can their acoustic features be characterized separately?

This work is structured as follows: In Chapter 1, the theoretic background is presented. This includes a revisitation of acoustic beamforming and the state-of-the-art VRA methods. Aside from conventional beamforming formulations in the space-time and space-frequency domains, a formulation in the mode-frequency domain is also introduced. In addition, a new VRA formulation in the mode-time domain is derived, as are methods for de-noising acoustic data and detecting rotational speeds from microphone array measurements.

Chapter 2 introduces the data sets on the basis of which the methods are tested with regard to their performance. These data include simulated cases with multiple rotating point sources and array measurements of two fans in different environments.

Chapter 3 is dedicated to the demonstration and evaluation of the applicability of the methods. Based on the simulated data sets, theoretical requirements for successfully applying the methods as well as their capabilities and application limits are examined in more detail. The application of the presented methods for a detailed study of the occurring aeroacoustic phenomena is beyond the intended scope of this work. Nevertheless, it is shown based on the measured data that new insights into previously hidden acoustic features can indeed be gained with the help of the presented techniques.

Finally, the investigations made in this thesis, as well as important findings from them, are summarized in Chapter 4, which also discusses the answers to the above research questions.

1. The Fellowship of the Microphones

Theory and Methods

1.1. Acoustic beamforming

Microphone arrays are employed to sample the sound field spatially, i. e. at the discrete positions of multiple microphones in space. The objective of this sampling is usually to obtain information about the characteristics of multiple present sound sources. This includes their positions, but also the respective amount of sound energy emitted towards the sampled region. In addition to knowing the position of the sensors, it is necessary to have knowledge about the sound propagation from the sources to the receivers. This, in turn, depends on the type of source as well as the properties of the sound-carrying medium. Depending on the level of complexity of the method used for the data evaluation, some parameters can be determined via measurements (e. g. the temperature), while others have to be modeled based on assumptions (e. g. the exact temperature distribution in a region).

For the measurement of the sound field, the time-dependent sound pressure, i. e. the deviation of the current local pressure from the average static pressure, is recorded synchronously with the distributed microphones. This is usually done with a constant time sampling rate. There exist numerous methods for the calculation of sound source characteristics based on microphone array data, which, however, may differ considerably regarding the assumptions being made, the employed mathematical methods as well as the signal processing steps.

Several widely-used methods and some typical applications of microphone arrays in an aero-acoustic context were compiled by Merino-Martínez et al. [2]. Leclère et al. [17] propose a classification of array methods by the kind of used mathematical solving strategy.

1.1.1. Beamforming in space and time

An array consisting of M microphones at positions $\boldsymbol{x}_l$ synchronously records the sound pressure time signals $p(l, t)$. Shifting each signal according to the sound travel time $\Delta t_{s,l}$ from an arbitrary point in space (index s) to the respective microphones (index l) and subsequent summing of the delayed signals yields a filter which amplifies the signals emitted from this "focus" point and attenuates signals arriving from from other locations [18]. This is the basic idea of "delay-and-sum" beamforming. The sound travel time can be calculated from the measurable distance $r_{s,l} = \Delta t_{s,l} \cdot c$ between one focus point and one microphone. The speed of sound c is assumed to be constant along the sound path. Figure 1.1 illustrates an array setup as it is typically used in this thesis.

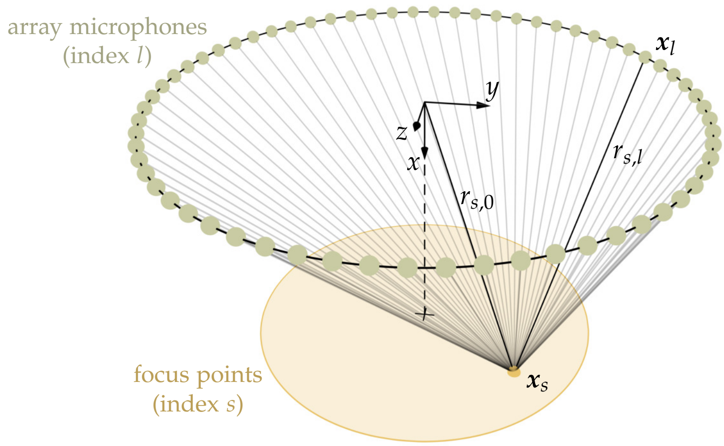

Figure 1.1. Schematic of the beamforming setup with a circular microphone array (green) and a region of interest (yellow). Visualization of the distances needed for "steering" the array to one exemplary focus point.

The time delay for signal shifting can also be calculated from the differences between the sound travel times from focus point to the microphones and from focus point to a reference position:

$$p_{\text{out}}(t) = \sum_{l=1}^{M} g_l \, p(l, t + \Delta t_{s,l} - \Delta t_{s,0}) \ . \tag{1.1}$$

The factor g_l for individual weighting of the microphones allows the manipulation of the filter's imaging properties.

Aside from the time-dependent sound pressure signal as calculated in Eq. (1.1), the average incident acoustic energy may be of interest. This is described by the sound pressure level, which is calculated via [19]:

$$L_p = 10 \lg \left(\frac{\tilde{p}^2}{\tilde{p}_0{}^2} \right) \text{dB} \ , \tag{1.2}$$

with the reference pressure for airborne sound $\tilde{p}_0 = 2 \times 10^{-5}$ Pa. With a uniform discretization of the time at a sampling rate f_s and with N_s discrete time samples, the squared effective sound pressure (or squared RMS values) of the calculated beamforming result can be calculated via

$$\tilde{p}^2 = \frac{1}{N_\text{s}} \sum_{t=0}^{N_\text{s}-1} p_{\text{out}}{}^2(t) \ . \tag{1.3}$$

Here, $t = t \cdot f_\text{s}$ marks the discrete number of the sample.

Due to the discrete and spatially limited sampling of the sound field, imaging artefacts such as an apparent spatial extent of point sources or even false secondary sources can occur. In part, the shape of these artefacts can be manipulated by the choice of the weighting factor g_l, which also influences the amplitudes of the reconstructed signals p_{out}. In the literature, different formulations to calculate this factor can be found.

Four commonly used formulations were compared by Sarradj [20] in terms of quantitative accuracy and correct source localization in the result when using planar array arrangements. It was found not only that the spatial resolution capability of planar microphone arrangements is considerably lower perpendicular to the array plane than parallel to it, but also that depending on the formulation, either the reconstruction of a source's position or its amplitude is not perfectly accurate.

Calculating the weighting factor via

$$g_{l,3} = \frac{1}{r_{s,0}\, r_{s,l} \sum_{i=1}^{M} {r_{s,i}}^{-2}} \tag{1.4}$$

ensures that focusing on the position of a monopole source present in the sound field will yield its correct amplitude. On the other hand, if the calculation is done via

$$g_{l,4} = \frac{1}{r_{s,l} \sqrt{M \sum_{i=1}^{M} {r_{s,i}}^{-2}}} \,, \tag{1.5}$$

the maximum amplitude in a map coincides with the actual source position. The numbering indices $_3$ and $_4$ correspond to the naming in the study by Sarradj [20].

1.1.2. Beamforming in space and frequency

It can be convenient to describe signals depending on frequency rather than on time, especially if the quantities of interest do not change significantly during the observed period.

An evenly sampled time signal can be transformed into the frequency domain using a discrete Fourier transform (DFT) [21]:

$$p(f) = \frac{1}{\sqrt{N_\mathrm{s}}} \sum_{t=0}^{N_\mathrm{s}-1} p(t) \mathrm{e}^{-\mathrm{j}2\pi f \frac{t}{N_\mathrm{s}}} \equiv \mathcal{F}_f(p(t)) \,. \tag{1.6}$$

The resulting frequency index $f = -\frac{N_\mathrm{s}}{2} \ldots \frac{N_\mathrm{s}}{2}$ can be converted to a frequency via $f = \frac{f}{N_\mathrm{s}} \cdot f_\mathrm{S}$. Depending on convention, the Fourier transform is defined with different normalization factors. The factor $\frac{1}{\sqrt{N_\mathrm{s}}}$ ensures that the overall signal power remains the same after the transformation (see also appendix C). Similar to Eq. (1.1), the beamforming can be done in the frequency domain with

$$p_\mathrm{out}(f) = \sum_{l=1}^{M} g_l p_l(f)\; \mathrm{e}^{-\mathrm{j}2\pi f (\Delta t_{s,0} - \Delta t_{s,l})} \,. \tag{1.7}$$

Combining the weighting factors from equations (1.4) and (1.5) with the exponential terms of the sum elements from Eq. (1.7) via $h_l^* \equiv g_l \, \mathrm{e}^{-\mathrm{j}2\pi f(\Delta t_{s,0}-\Delta t_{s,l})}$ leads to the *steering vectors*

$$\boldsymbol{h}_{l,3}(f) = \begin{pmatrix} \frac{\mathrm{e}^{-\mathrm{j}2\pi f(\Delta t_{s,1}-\Delta t_{s,0})}}{r_{s,0}\, r_{s,1} \sum_{i=1}^{M} r_{s,i}{}^{-2}} \\ \frac{\mathrm{e}^{-\mathrm{j}2\pi f(\Delta t_{s,2}-\Delta t_{s,0})}}{r_{s,0}\, r_{s,2} \sum_{i=1}^{M} r_{s,i}{}^{-2}} \\ \vdots \\ \frac{\mathrm{e}^{-\mathrm{j}2\pi f(\Delta t_{s,M}-\Delta t_{s,0})}}{r_{s,0}\, r_{s,M} \sum_{i=1}^{M} r_{s,i}{}^{-2}} \end{pmatrix} \tag{1.8}$$

and

$$\boldsymbol{h}_{l,4}(f) = \begin{pmatrix} \frac{\mathrm{e}^{-\mathrm{j}2\pi f(\Delta t_{s,1}-\Delta t_{s,0})}}{r_{s,1} \sqrt{M \sum_{i=1}^{M} r_{s,i}{}^{-2}}} \\ \frac{\mathrm{e}^{-\mathrm{j}2\pi f(\Delta t_{s,2}-\Delta t_{s,0})}}{r_{s,2} \sqrt{M \sum_{i=1}^{M} r_{s,i}{}^{-2}}} \\ \vdots \\ \frac{\mathrm{e}^{-\mathrm{j}2\pi f(\Delta t_{s,M}-\Delta t_{s,0})}}{r_{s,M} \sqrt{M \sum_{i=1}^{M} r_{s,i}{}^{-2}}} \end{pmatrix} \tag{1.9}$$

respectively. They are specific to one frequency and one focus point and contain all information to "steer" the array to this focus point, i. e. the phase shift and microphone weighting based on the underlying sound propagation model. The Fourier-transformed data can be written in a vector as well:

$$\boldsymbol{p}_l(f) = (p_1(f), p_2(f), \ldots, p_M(f))^{\mathrm{T}}. \tag{1.10}$$

With implicit frequency dependency, Eq. (1.7) can then be written as:

$$p_{\mathrm{out}} = \boldsymbol{h}_l^{\mathrm{H}} \, \boldsymbol{p}_l \;, \tag{1.11}$$

where $^{\mathrm{H}}$ is the Hermitian transpose. The summation is done directly by the matrix multiplication.

Both steering vector formulations will be used for beamforming later on: Eq. (1.8) for the simulated cases, where it can be ensured that the sources lie within the focus area but it is important to evaluate the quantitative information, and Eq. (1.9) for the measured cases to ensure a good localization of the sources.

1.1.3. Beamforming in modes and frequency

A sound field can be described by the superposition of modes. The type and number of modes that can be resolved by discrete spatial sampling depends on the array geometry and the number of sensors respectively. For example, if the microphones are arranged in a circular and regular pattern (as in Fig. 1.1), modes that are shaped accordingly (i. e. azimuthal modes) can be resolved, where the maximum resolvable mode order corresponds to half the number of sensors. This is analogous to the Nyquist frequency resolution limit depending on a given temporal sampling frequency [22]. In principle, it is possible to increase the mode resolution by strategically placing the sensors in an irregular fashion [23], however, such geometries are not considered here.

Analogous to the transformation from the time into the frequency domain in Eq. (1.6), the transformation from the spatial into the mode domain can be done via a Fourier transform:

$$p(m,f) = \frac{1}{\sqrt{M}} \sum_{l=0}^{M-1} p(l,f)\, \mathrm{e}^{-\mathrm{j}2\pi m \frac{l}{M}} \equiv \mathcal{F}_m(p(l,f)) \,, \tag{1.12}$$

with the angular position $2\pi\frac{l}{M} = \varphi_l$ of the azimuthally evenly distributed microphones $l = 0 \ldots M-1$. While in Eq. (1.12), the sound pressure is described frequency-dependent, the space-mode transformation is equally valid in the time domain, as time and space (or frequencies and modes) can be regarded independently here.

Likewise, the steering vector (equations (1.8) and (1.9)) can be transformed into the mode domain:

$$\boldsymbol{h}_m \equiv \mathcal{F}_m(\boldsymbol{h}_l) \tag{1.13}$$

With Parseval's theorem (see appendix C)

$$\begin{aligned} \sum_{l=0}^{M-1} p(l,f)\, h(l,f)^* &= \sum_{m=-M/2}^{M/2-1} \mathcal{F}_m(p(l,f))\, \mathcal{F}_m(h(l,f))^* \\ &= \sum_{m=-M/2}^{M/2-1} p(m,f)\, h(m,f)^* \,, \end{aligned} \tag{1.14}$$

Equation (1.11) can be equivalently formulated in the mode domain:

$$p_{\text{out}} = \boldsymbol{h}_m^{\mathrm{H}}\, \boldsymbol{p}_m \,. \tag{1.15}$$

Since all transmission properties have been transformed into the mode-frequency domain, the scalar result of p_{out} still describes the sound pressure result for a point in space, which is implicitly defined by the sound travel distances or times calculated in the beginning.

1.1.4. Beamforming with the cross-spectral matrix

Beamforming in the frequency domain usually is formulated such that it directly yields the spatially filtered squared sound pressure magnitude $|p_{\text{out}}|^2$ as energetic quantity. For complex quantities, this can be achieved by multiplying with the complex conjugate:

$$|p_{\text{out}}|^2 = p_{\text{out}} \cdot p_{\text{out}}^* = \boldsymbol{h}^{\mathrm{H}}\, \boldsymbol{p} \cdot \boldsymbol{p}^{\mathrm{H}}\, \boldsymbol{h} \,. \tag{1.16}$$

Especially for stochastic signals ("noise"), it is useful to average over several measured values for the calculation of the result at one frequency. The product $\boldsymbol{p} \cdot \boldsymbol{p}^{\mathrm{H}}$ yields a matrix, in which the off-diagonal elements contain the phase differences between the respective channels. Therefore, the multiplication should be performed before the averaging:

$$\boldsymbol{C} = \frac{1}{K} \sum_{k=0}^{K-1} \boldsymbol{p}_k \, \boldsymbol{p}_k{}^{\mathrm{H}} \, . \tag{1.17}$$

The matrix $\boldsymbol{C}$ resulting from averaging K matrices is called the *cross-spectral matrix* (CSM). It can be calculated from $\boldsymbol{p}_l$ in the spatial domain (CSM-S) as well as from $\boldsymbol{p}_m$ in the mode domain (CSM-M). For a given focus point, the beamforming result at a specific frequency is then calculated via:

$$|p_{\mathrm{out}}|^2 = \boldsymbol{h}^{\mathrm{H}} \, \boldsymbol{C} \, \boldsymbol{h} \, . \tag{1.18}$$

The higher the number K of averaged cross spectra, the better the statistical accuracy of the CSM calculated according to Eq. (1.17) [24]. The number of averages can be increased at the expense of the frequency resolution using different methods [25].

According to the method introduced by Daniell [26], the complete time signals are transformed into the frequency domain, so that a very fine frequency resolution is achieved. Then the cross correlations between the channels are calculated. Now a nominally lower frequency resolution is defined and for each of the low-resolution frequencies, K neighboring high-resolution frequencies are determined. The respective associated cross-correlation matrices are then averaged.

In the context of array methods, the method introduced by Welch [27] is widely used. Here, the time signals are divided into K blocks of fixed length and Fourier-transformed. To avoid leakage effects, these blocks can be multiplied by a windowing function [24]. After block-wise cross-correlation, the resulting matrices are averaged for each frequency.

While the results calculated using Daniell's method are comparable [28], Welch's method has the advantage that less computer memory is required due to the successive calculation of DFTs of short time intervals. Furthermore, the estimation of the CSM can already be started before all time data are available. In further investigations, the CSM is therefore calculated according to this method.

1.1.5. De-noising of the CSM diagonal

The main diagonal of the cross-spectral matrix contains the autospectra of the M input *channels*. Depending on the calculation domain, this can be *microphones* or *modes*. The autospectra are purely real and do not contain any information about phase differences, but for each channel the squared RMS sound pressure. However, this may contain signals uncorrelated with other channels – such as pressure fluctuations caused by flow over the microphones – which manifest as unwanted noise. For this reason, it is common practice to omit the main diagonal from the calculations [1].

Alternatively, the CSM can be de-noised, i. e., together with assumptions about its internal structure, suitable procedures are used to compute a version of the CSM that no longer includes the interfering signals. Dinsenmeyer et al. [29] compared a variety of methods developed for this purpose. Assuming that any existing noise is no longer included in the cross correlations between different channels, i. e. it is only the main diagonal that contains the noise σ

$$\boldsymbol{C}_{\text{measured}} = \boldsymbol{C}_{\text{de-noised}} + \text{diag}({\sigma_1}^2, \ldots, {\sigma_M}^2) \ , \tag{1.19}$$

it is enough to correct the entries of the main diagonal.

Methods based on this were presented, among others, by Hald [30], Dougherty [31], Finez et al. [32], and Sijtsma et al. [33]. In the following, a two-step method for the reconstruction of the main diagonal is introduced. An exemplary comparison of the method presented here with the alternating projections diagonal reconstruction (DRAP) proposed by Leclère et al. [34] is done in appendix D.

The employed method is based on energetic considerations. Phase information is not helpful for this, so that initially only the magnitude information of the complex-valued CSM entries is used:

$$C_{\text{abs},ij} = |C_{\text{measured},ij}| \ . \tag{1.20}$$

For the first step, it is assumed that the signal-to-noise ratio (SNR) on the main diagonal $\boldsymbol{d} \equiv C_{\text{abs},i=j}$ is approximately the same for all channels. An estimate for its magnitude is obtained by searching for the largest value both off- and on-diagonal and calculating the ratio of the two:

$$u = \frac{\max(C_{\text{abs},i\neq j})}{\max(\boldsymbol{d})} \ . \tag{1.21}$$

Now the entries of the main diagonal are multiplied by this ratio:

$$\boldsymbol{d}_{(0)} = u \cdot \boldsymbol{d} \ . \tag{1.22}$$

In a first approximation, the acoustic energy contained in the main diagonal now corresponds to that present in the cross spectra.

For further approximation and in order to take into account possibly channel-specific SNRs, the diagonal entries are now adjusted through an iterative process. It is initialized using the corrected main diagonal from Eq. (1.22). From the diagonal $\boldsymbol{d}_n$ approximated in the n^{th} iteration, the theoretical RMS values of the individual channels are calculated:

$$\tilde{p}_{i,(n)} = \sqrt{d_{i,(n)}} \ . \tag{1.23}$$

With these, a theoretical cross-spectral magnitude matrix is generated:

$$C_{\text{th},ij,(n)} = \tilde{p}_{i,(n)} \cdot \tilde{p}_{j,(n)} \ . \tag{1.24}$$

Now, the differences between the off-diagonal entries of the theoretical magnitude CSM $\boldsymbol{C}_{\text{th},(n)}$ and those of the initial CSM $\boldsymbol{C}_{\text{abs}}$ are calculated and averaged along the rows (or columns):

$$\Delta d_{j,(n)} = \frac{1}{M-1} \sum_{i,i\neq j} \left(C_{\text{abs},ij} - C_{\text{th},ij,(n)} \right) \ . \tag{1.25}$$

The resulting vector $\Delta \boldsymbol{d}_{(n)}$ contains the approximate deviations of the current to the fully denoised squared sound pressure RMS values and can be used for further fitting the on- and off-diagonal energies:

$$\boldsymbol{d}_{(n+1)} = \boldsymbol{d}_{(n)} + \Delta \boldsymbol{d}_{(n)} \; . \tag{1.26}$$

The next step again consists of calculating the RMS values using Eq. (1.23), with prior setting all negative entries to zero. This process can be repeated a fixed number of iterations or until convergence. At the end, the original diagonal of the measured CSM is replaced by this "de-noised" version. The described procedure for reconstructing the diagonal is summarized in Algorithm 1.1 and shall be abbreviated "DREF" (*diagonal reconstruction through energy fitting*) for the remainder of this thesis.

Require: $\boldsymbol{C}$	▷ CSM for one frequency, incl. noise
$C_{\mathrm{abs},ij} \leftarrow \lvert C_{ij} \rvert$	▷ matrix with amplitudes of the CSM entries
$d \leftarrow C_{\mathrm{abs},i=j}$	▷ get CSM diagonal
$d_{\max} \leftarrow \max(d)$	▷ maximum of the diagonal
$o_{\max} \leftarrow \max(C_{\mathrm{abs},i\neq j})$	▷ maximum of off-diagonal values
$u \leftarrow o_{\max}/d_{\max}$	▷ energy correction factor
$d \leftarrow d \cdot u$	▷ 1st approximation of de-noised diagonal
while max. iterations or convergence not reached **do**	
$\tilde{p}_i \leftarrow \sqrt{d_i}$	▷ RMS sound pressure per channel
$C_{\mathrm{th}} \leftarrow \tilde{\boldsymbol{p}} \cdot \tilde{\boldsymbol{p}}^{\mathrm{T}}$	▷ theoretic "magnitude" CSM
$\Delta \boldsymbol{C} \leftarrow \boldsymbol{C}_{\mathrm{abs}} - \boldsymbol{C}_{\mathrm{th}}$	▷ deviations of all entries
$\Delta C_{i=j} \leftarrow 0$	▷ set diagonal to 0 for summing
$\Delta d_j \leftarrow 1/(M-1) \cdot \sum_{i=1}^{M} \Delta C_{ij}$	▷ average deviation per channel
$\boldsymbol{d} \leftarrow \boldsymbol{d} + \Delta \boldsymbol{d}$	▷ update diagonal
$d_{(d_i<0)} \leftarrow 0$	▷ set negative entries to zero
end while	
$C_{i=j} \leftarrow d_i$	▷ replace diagonal in orginal CSM
Return: $\boldsymbol{C}$	▷ de-noised CSM for one frequency

Algorithm 1.1. DREF method for denoising the CSM diagonal.

The iterative part can also be executed without the initial diagonal normalization by Eq. (1.21). While the system will still converge, this might impact the rate of convergence. Furthermore, the initial estimate through normalization may already yield a good approximation of the diagonal. In principle, it is possible to alternatively use the ratio $C_{\mathrm{abs},ij}/C_{\mathrm{th},ij,(n)}$ in Eq. (1.25) and the resulting vector entries as correction factors in (1.26). Furthermore, it is conceivable to use Eq. (1.25) as cost function for arbitrary minimization algorithms. However, the method as proposed here already provides sufficient convergence behavior for practical applications. This is shown in appendix D.

At this point it is important to mention that it makes a difference whether the CSM calculation and the subsequent diagonal reconstruction is done in the spatial (DREF-S) or in the mode domain (DREF-M).

Beamforming does provide the same result when using the full, non-denoised CSM. However, after reconstructing the main diagonal, there can be significant differences. For this purpose it helps to realize that off-diagonal inter-channel phase differences which vary over time ("incoherences") average out if the number of single cross correlations is sufficiently high (see also section 1.1.4). As mentioned above, such transient phase differences can be caused by flow-induced noise in the spatial domain. In the mode domain, variable phase differences between modes also occur when sources are non-stationary in the current frame of reference (see also section 1.2.2). This means that with the DREF-M method, interfering influences of rotating sources – i. e. "rotation noise" – can be reduced.

On first glance, this may appear similar to a cyclostationary signal processing approach, where multiple time segments of the duration of one revolution are averaged, thereby decreasing the contribution of random noise [35]. While the results obtained by the two methods may be similar in some cases, in general they are not, as the underlying philosophies differ. With the methods proposed here, an arbitrary rotation is transformed into the stationary domain, and *any* source rotating at a different speed is considered rotation noise. Therefore, e. g. the contribution of sources rotating at multiples of the considered rotation will remain part of the result with a cyclostationary approach, whereas with DREF-M, it will be decreased.

1.1.6. A high-resolution array method in the frequency domain

Mapping the sound source distribution using classic beamforming with Eq. (1.18) on an area discretized with multiple focus points will result in the sound map containing imaging artefacts – even with perfect input data. This is illustrated in Figure 1.2, where an exemplary evaluation is done for simulated data with one point source at 12 o'clock.

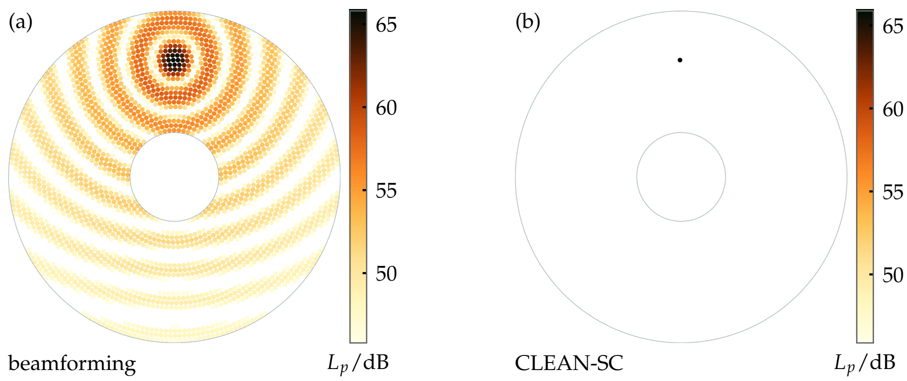

Figure 1.2. Example sound maps for a simulated point source, evaluated at 4 kHz narrow band with (a) frequency domain beamforming and (b) CLEAN-SC. The thin blue lines mark the limits of the evaluated focus area.

With mere beamforming in the frequency domain (Fig. 1.2a), the maximum in the map coincides with the source position, however, the source appears to extend over the neighboring focus points. Furthermore, a repeating pattern of additional local maxima is visible around the source. The size and shape of these artefacts (i. e. *beam width* and *side lobes*) depend on the evaluated frequency, the sound source and propagation model, the focus area, and the array geometry. Since these parameters can be assumed to be known, the image theoretically generated by a point source can be calculated. This is the *point spread function* (PSF), and it can be used to inversely deduce the underlying source distribution based on a beamforming map [36, 37]. Inverse methods generally provide good results with significantly enhanced resolution of the source distribution. However, their application requires the focus region considered to sometimes extend well beyond the area of interest and requires long computation times compared to other methods [17, 38].

With the assumption that maxima in a beamforming map coincide with a source position, the source map can be "cleaned up" by subtracting the corresponding PSFs [39]. With the CLEAN-SC method, Sijtsma [40] extended this idea by allowing arbitrary PSFs, but requiring that they be coherent with the found maxima. This is done by identifying subspaces in the CSM that correspond to the maxima and iteratively subtracting the PSFs defined by these subspaces from the original map, possibly revealing previously masked sources. All found maxima are then compiled in a new map. It shall be noted that while the algorithm was developed to identify spatial coherence ("-SC") and works with the microphone cross-spectra, it can also be applied in combination with the CSM in the mode domain.

The map resulting from the point source example given here is shown in Figure 1.2b and contains, as expected, one point. The simulation and evaluation parameters used here correspond to the simulations described in sections 2.1 and 3.1.

1.2. Virtual rotating array

In general, there are two different principles to compensate for a rotation of sources using array methods: either through a continuous adjustment of the focus (i. e. the time shift) or by implementing a transformation into a frame of reference which is rotating synchronously to the sources and in which the sensor positions are stationary.

The first principle can be applied to arbitrary source movements and has also been used for rotating sources [41, 42]. Since the distances between focus points and microphones change continuously, only adapted time domain array methods can be applied here.[1] Therefore, the advantages of doing the calculations in the frequency domain – such as the de-noising of the data using the CSM (see section 1.1.5) or the application of several high-resolution array methods (see section 1.1.6), cannot be exploited. While there are time domain based methods for increasing the spatial resolution by deconvolving the classic beamforming results [43–45], these are not as time-efficient as, for instance, CLEAN-SC. In addition, it should be noted that already for the non-deconvolved beamforming, the required computational time in the time domain exceeds that in the frequency domain by two orders of magnitude [14].

With an array moving synchronously to the sources, these are stationary in the moving frame of reference, so that beamforming methods in the frequency domain can be applied. The principle of source-synchronous rotation can be implemented e. g. by an array which actually rotates [46]. However, this implies high constructional effort and is not always possible. In practice, a simpler option is to track the movement of the sources and then interpolate data measured with a stationary array according to the movement using suitable techniques. A disadvantage compared to continuous focus adjustment is the limitation to measurement

[1]This means that in equations (1.1) and (1.4)/(1.5), the respective time dependencies $\Delta t_{s,\ldots}(t)$ and $r_{s,\ldots}(t)$ have to be considered.

configurations where the motion of the considered sources follows trajectories to which a sufficient number of "virtual sensors" can be interpolated to be at a constant distance.

Such a configuration is, however, relatively easy to realize for many rotating measuring objects via an array consisting of microphones arranged on one or more rings. For this, the center of each ring needs to lie on the rotation axis and the plane of the ring needs to be perpendicular to it (e. g. corresponding to the setup shown in Fig. 1.1). Recent investigations by Jekosch and Sarradj [47] showed that a successful virtual rotation can also be done with the sensors being non-uniformly distributed in a plane, although resulting in a reduced spatial resolution capability of the virtual array. If the microphones are uniformly distributed on a ring, data interpolation for realization of sensors stationary relative to the sources is very efficient [5, 7]. In the following sections, two methods for implementing such a *virtual rotating array* (VRA) are presented.

1.2.1. VRA in the spatial domain

The principle of the virtual rotating array in the spatial domain is based on an interpolation of time signals measured at discrete positions with time-varying weighting. The starting point is an array consisting of M microphones uniformly distributed in a ring. The individual microphones are numbered by $l = 0 \ldots M-1$.

The rotation is described by the time-varying angle $\varphi(t)$. The sound pressure in the co-rotating frame of reference can then be described by

$$p_{\mathrm{rot}}(l_{\circlearrowleft}, t) = p(l_{\circlearrowright} + M \cdot \frac{\varphi(t)}{2\pi}, t) \ . \tag{1.27}$$

The discrete microphone positions are denoted by $l_{\circlearrowright}$ for the stationary reference frame and by $l_{\circlearrowleft}$ for the rotating reference frame (see Fig. 1.3). Independent of the reference system, $0 \leq l < M$ is always valid for the spatial index l. This means that values lying outside this interval are to be interpreted according to the ring arrangement: $p(l) \equiv p(l + nM), n \in \mathbb{Z}$.

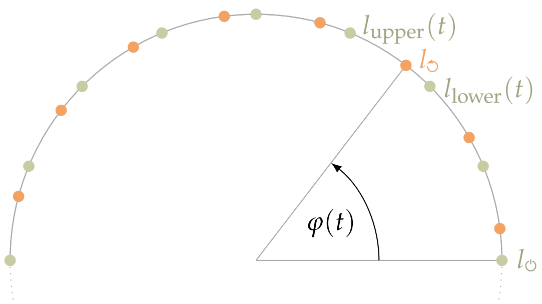

Figure 1.3. Schematic of the VRA relations in the spatial domain (physical microphones in green, virtual microphones in orange).

Since the sound field is sampled only at discrete positions, the evaluation of Eq. (1.27) usually involves an interpolation of signals. A simple possibility for this is the linear interpolation from the signals of immediately neighboring microphones [7]:

$$p_{\mathrm{rot}}(l_{\circlearrowleft}, t) = w_{\mathrm{lower}}\, p(l_{\mathrm{lower}}, t) + w_{\mathrm{upper}}\, p(l_{\mathrm{upper}}, t) \tag{1.28}$$

with the microphone indices

$$\begin{aligned} l_{\mathrm{lower}}(t) &= \left\lfloor l_{\circlearrowleft} + M \cdot \frac{\varphi(t)}{2\pi} \right\rfloor \bmod M \\ l_{\mathrm{upper}}(t) &= \left\lfloor l_{\circlearrowleft} + M \cdot \frac{\varphi(t)}{2\pi} + 1 \right\rfloor \bmod M \end{aligned} \tag{1.29}$$

and the weighting factors

$$\begin{aligned} w_{\mathrm{upper}}(t) &= M \cdot \frac{\varphi(t)}{2\pi} - \left\lfloor M \cdot \frac{\varphi(t)}{2\pi} \right\rfloor . \\ w_{\mathrm{lower}}(t) &= 1 - w_{\mathrm{upper}}(t) \end{aligned} \tag{1.30}$$

This method for the realization of a virtual rotating array in the spatial domain (VRA-S) is applicable in practice and has been used in several investigations on the sound radiation of rotating machinery [8–11, 48].

Assuming spatial periodicity of the signal over the circumference, a Whittaker-Shannon interpolation [49], in which the signals of all microphones are included in the result, can be used instead of the simple linear interpolation. The weighting to be performed then is described in more detail in appendix A. The resulting signals then correspond to the virtual rotation in the mode domain [13, 50], which is described in more detail in the following section.

1.2.2. VRA in the mode domain

The implementation of a virtual rotation is also possible with data transformed into the mode domain. Methods for this were described by Lowis and Joseph [51] and by Pannert and Maier [6], who realized the virtual rotation by a frequency shift according to the considered rotation frequency, i. e. in the mode-*frequency* domain. However, a computation in the frequency domain has the disadvantages of not only being constrained to constant rotational speeds, but also requiring a finer frequency resolution, which has to be realized by using accordingly longer time intervals [14, 15].

Therefore, the approach adopted here considers the virtual rotation in the mode-*time* domain. For this, the rotation in the spatial domain with Eq. (1.27) is transformed into the mode domain using Eq. (1.12):

$$\begin{aligned} p_{\mathrm{rot}}(m, t) &= \mathcal{F}_m(p_{\mathrm{rot}}(l_{\circlearrowleft}, t)) \\ &= \frac{1}{\sqrt{M}} \sum_{\forall l} p(l_{\circlearrowleft} + M \cdot \frac{\varphi(t)}{2\pi}, t)\, \mathrm{e}^{-\mathrm{j}2\pi m \frac{l_{\circlearrowleft}}{M}} . \end{aligned} \tag{1.31}$$

As described in the previous section, the rotating microphone position $l_{\circlearrowleft}$ and the stationary microphone position $l_{\circlearrowright}$ can be converted into each other via the current rotation angle $\varphi(t)$:

$$l_{\circlearrowleft} = l_{\circlearrowright} + M \cdot \frac{\varphi(t)}{2\pi} \quad \Rightarrow \quad l_{\circlearrowright} = l_{\circlearrowleft} - M \cdot \frac{\varphi(t)}{2\pi} \tag{1.32}$$

Inserting Eq. (1.32) into Eq. (1.31) yields

$$\begin{aligned} p_{\mathrm{rot}}(m,t) &= \frac{1}{\sqrt{M}} \sum_{\forall l} p(l_{\circlearrowleft},t)\, \mathrm{e}^{-\mathrm{j}\,2\pi\, m \frac{1}{M}\left(l_{\circlearrowleft} - M\cdot \frac{\varphi(t)}{2\pi}\right)} \\ &= \mathrm{e}^{\mathrm{j}\,2\pi\, m \frac{1}{M} M \cdot \frac{\varphi(t)}{2\pi}} \cdot \frac{1}{\sqrt{M}} \sum_{\forall l} p(l_{\circlearrowleft},t)\, \mathrm{e}^{-\mathrm{j}\,2\pi\, m \frac{l_{\circlearrowleft}}{M}} \end{aligned} \tag{1.33}$$

and with the definition of the DFT from Eq. (1.12) finally

$$p_{\mathrm{rot}}(m,t) = \mathrm{e}^{\mathrm{j}\, m\, \varphi(t)} \cdot p(m,t)\ . \tag{1.34}$$

Thus, the virtual rotation in the mode domain (VRA-M) can be realized directly without further interpolation simply by multiplying the time signal by the phase shift $\mathrm{e}^{\mathrm{j}\, m\, \varphi(t)}$. The signals can now be transformed back into the spatial domain for further calculations using microphone time data. Alternatively, the data can be directly processed in the mode domain, e. g. for beamforming according to section 1.1.3.

Via transformation into the frequency domain, Eq. (1.34) can be transformed into the formulation for virtual rotation in the mode-frequency domain. A derivation of this is described in appendix B.

1.2.3. Spatial resolution limitations of VRA

According to the Nyquist-Shannon sampling theorem, imaging errors (*aliasing*) occur in a discrete sampling process when the signal of interest contains frequencies that are above half the sampling rate [22]. Similarly, a successful virtual rotation requires a spatial sampling with at least two sensors per wavelength.

Based on this consideration, Lehmann et al. [16] performed investigations on the maximum frequency observable with the VRA for different source positions and microphone arrangements. In the following, a similar model for determining the sampling limits is developed, which also takes into account an omnidirectional wave characteristic as well as arbitrary relative positions of the microphones to a rotating source.

The array is a ring with a radius r_{array} and consists of M microphones. Its center is positioned at $(0,0,0)^{\mathrm{T}}$.

Two arbitrary adjacent microphones are then located at

$$\boldsymbol{x}_1 = \begin{pmatrix} 0 \\ r_{\mathrm{array}}\, \sin(\varphi) \\ r_{\mathrm{array}}\, \cos(\varphi) \end{pmatrix} \quad \text{and} \quad \boldsymbol{x}_2 = \begin{pmatrix} 0 \\ r_{\mathrm{array}}\, \sin(\varphi+\alpha) \\ r_{\mathrm{array}}\, \cos(\varphi+\alpha) \end{pmatrix}\ , \tag{1.35}$$

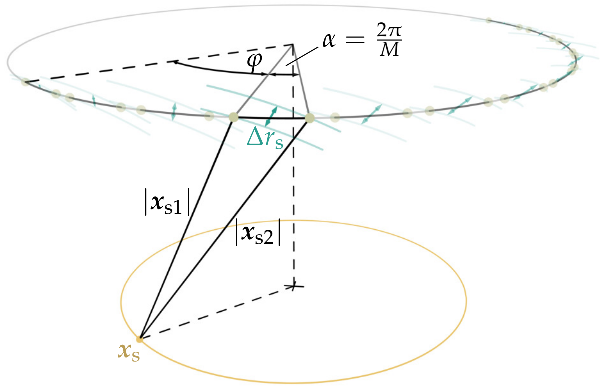

Figure 1.4. Geometric relations for determining the VRA resolution limit.

where the angle $\alpha = \frac{2\pi}{M}$ denotes the azimuthal offset of the two microphones (see Fig. 1.4). With the position of the point source at $\boldsymbol{x}_s$, the vectors between the source and the two microphones are calculated via

$$\boldsymbol{x}_{s1} = \boldsymbol{x}_1 - \boldsymbol{x}_s \quad \text{and} \quad \boldsymbol{x}_{s2} = \boldsymbol{x}_2 - \boldsymbol{x}_s \,. \tag{1.36}$$

The lengths of these two vectors correspond to the respective sound travel lengths in a medium at rest. Since they have the same origin, the smallest resolvable wavelength can be determined from the length difference:

$$\frac{\lambda}{2} \overset{!}{>} \Big| |\boldsymbol{x}_{s1}| - |\boldsymbol{x}_{s2}| \Big| = \Delta r_s \,. \tag{1.37}$$

This difference depends on the relative position of the source to the microphones, depending on the angle φ at which the rotation is currently located. Therefore, for determining the *globally* smallest resolvable wavelength, it is necessary to find the φ at which the distance difference Δr_s becomes maximal.

$$\lambda_{\min} = 2 \cdot \max_{\varphi} \Delta r_s \,. \tag{1.38}$$

This can be done, e. g., by a discrete search with a sufficiently fine step size of φ. In the case considered here, it is sufficient to restrict the search to the interval $\varphi \in [0, \pi[$, since by taking the absolute value in Eq. (1.37), the curve is mirrored. The highest frequency which can be resolved without aliasing is then

$$f_{\max} = \frac{c}{\lambda_{\min}} \,. \tag{1.39}$$

It is worth noting that the assumption of a stationary medium does not generally apply. For one, in connection with rotating machines, often the medium is moved as well which changes the effective lengths of the sound paths. But already in the case without flow, the virtual rotation in the moving reference frame implicitly leads to a rotation imposed on the medium, as described in section 1.3. A general suitability of the described method for estimating the application limits is investigated in section 3.1.

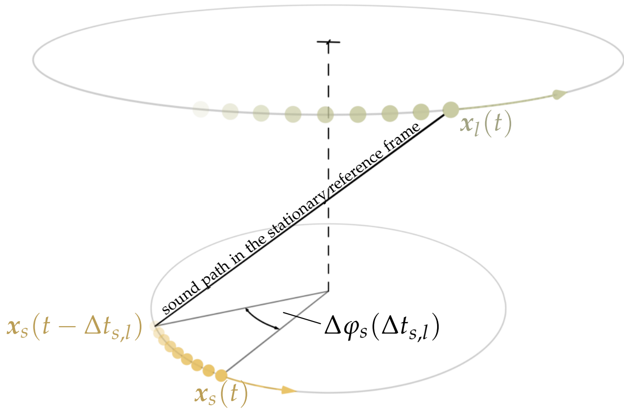

Figure 1.5. Effective sound path from an exemplary focus-point (yellow) to a synchronously rotating microphone (green).

1.3. Considering a rotating medium

In the rotating frame of reference, the flow of the medium in which sound is propagating is superimposed with a rotation in the opposite direction. Therefore, the sound travel times from assumed source positions (i. e. focus points, see section 1.1.2) to the microphones differ from those in a resting medium. For a successful sound source detection, this has to be taken into account.

Several methods can be used for implementing this. Lowis and Joseph [52] as well as Pannert and Maier [6] derive a transfer function in the mode-frequency domain for this. Ocker and Pannert [53] propose a ray tracing method based on acoustic analogies to general relativity. Sarradj et al. [54] also describe a ray tracing algorithm that can in principle be applied to arbitrary steady-state flow fields [55]. Herold and Sarradj [7], together with the VRA in the spatial domain, use an iterative method with a relatively simple approach described below.

The basic assumption is that the sound travel time from a (rotating) focus point $\boldsymbol{x}_s$ to a (virtually rotating) microphone $\boldsymbol{x}_l$ does not change over the entire observation period. This is the case when the rotational speed is constant. In the case without rotation and flow, the sound travel time is calculated via the speed of sound from the Euclidean distance between the measurement point and the focus point:

$$\Delta t_{s,l}(f_{\text{rot}} = 0) = \frac{1}{c} \cdot |\boldsymbol{x}_l - \boldsymbol{x}_s| \; . \tag{1.40}$$

If both points rotate, this is no longer the case. In the stationary reference frame, the sound path is still a straight line (see Fig. 1.5). However, the location at which the sound wave arriving at the microphone at time t was emitted at the retarded time $t - \Delta t_{s,l}$ does not correspond to the current position of the focus point $\boldsymbol{x}_s(t)$, since that has moved further during the travel time of the sound. Therefore, the following applies:

$$\Delta t_{s,l} = \frac{1}{c} \cdot |\boldsymbol{x}_l(t) - \boldsymbol{x}_s(t - \Delta t_{s,l})| \; . \tag{1.41}$$

In the cases considered here, only rotations about the x axis occur. Therefore, it is sufficient to consider the change of the angle:

$$\boldsymbol{x}_s(t - \Delta t_{s,l}) = \begin{pmatrix} x_{s1} \\ \rho_s \cdot \sin(\varphi_s(t) - \Delta\varphi_s(\Delta t_{s,l})) \\ \rho_s \cdot \cos(\varphi_s(t) - \Delta\varphi_s(\Delta t_{s,l})) \end{pmatrix} . \tag{1.42}$$

The angular displacement $\Delta\varphi_s(\Delta t_{s,l})$ is calculated depending on the rotational frequency f_{rot} with

$$\Delta\varphi_s(\Delta t_{s,l}) = 2\pi f_{\mathrm{rot}} \cdot \Delta t_{s,l} . \tag{1.43}$$

It becomes clear from equations (1.41), (1.42) and (1.43) that the sound travel time cannot be calculated analytically since $\Delta t_{s,l}$ occurs both inside and outside the argument of the angular functions. A method for the numerical approximation is described in Algorithm 1.2.

Require: $\boldsymbol{x}_l, \boldsymbol{x}_s, f_{\mathrm{rot}}, c$
$\rho_s \leftarrow \sqrt{{x_{s3}}^2 + {x_{s2}}^2}$ ▷ radius of focus point
$\varphi_s \leftarrow \mathrm{atan2}(x_{s3}, x_{s2})$ ▷ angle of focus point using quadrant-aware arctangent
$\Delta t_{s,l} \leftarrow |\boldsymbol{x}_l - \boldsymbol{x}_s|/c$ ▷ initialize sound travel time with Eq. (1.40)
while not converged **do**
  $\Delta\varphi_s \leftarrow 2\pi f_{\mathrm{rot}} \cdot \Delta t_{s,l}$ ▷ angular shift after Eq. (1.43)
  $x_{s3} \leftarrow \rho_s \cdot \cos(\varphi_s - \Delta\varphi_s)$ ▷ update focus point with Eq. (1.42)
  $x_{s2} \leftarrow \rho_s \cdot \sin(\varphi_s - \Delta\varphi_s)$
  $\Delta t_{s,l} \leftarrow |\boldsymbol{x}_l - \boldsymbol{x}_s|/c$ ▷ update sound travel time with Eq. (1.40)
end while
Return: $\Delta t_{s,l}$ ▷ sound travel time from $\boldsymbol{x}_s$ to $\boldsymbol{x}_l$

Algorithm 1.2. Method for the calculation of sound travel time in a rotating medium.

In the context of fluid machinery, it is sometimes helpful to be able to consider an axial flow. For this purpose, Eq. (1.41) can be extended. The corresponding formulation is described in appendix E. In practice, the prerequisite of constant rotation cannot always be fulfilled. However, small variations in rotational speed do not substantially degrade the result [14]. The performance of this iterative method for compensating a medium rotation was shown to be comparable to that of a ray tracing approach [54].

1.4. Rotational speed from acoustic data

Prerequisite for a meaningful virtual rotation as described in sections 1.2.1 and 1.2.2 is knowledge about the rotational speed f_{rot} of the sources of interest or, more to the point, their current rotation angle

$$\varphi(t) = 2\pi \int_0^t f_{\mathrm{rot}}(\tau)\,\mathrm{d}\tau . \tag{1.44}$$

In practice, it is usually determined using optical or magnetic sensors, which, for instance, deliver one trigger signal per completed revolution. By recording multiple subsequent trigger instants, a time-dependent rotation angle can then be interpolated.

However, this method is only feasible for tracking such acoustic sources that rotate synchronously with a suitably detectable object – e. g. a fan blade with a reflector attached to it. While sources that rotate differently can be filtered out as described in section 1.1.5, it may well be of interest that they are present at all and what their rotation characteristics are. A method that determines occurring rotational frequencies based solely on acoustic measurement data from a microphone ring array has already been presented [56] and will be extended below.

As mentioned in section 1.2.2, the transformation from the rotating into the stationary frame of reference can be realized by shifting the spectrum in the mode-frequency domain by the term $m\, f_{\mathrm{rot}}$ [51]:

$$p(m, f_{\circlearrowright}) = p(m, f_{\circlearrowleft} + m\, f_{\mathrm{rot}}) \; . \tag{1.45}$$

For stationary sources, similar spectral characteristics can be assumed to be present in all modes, although the magnitude and phase may differ depending on the mode order and source position. The same is true for non-stationary (i. e. rotating) sources, for which, however, the mode spectrum is shifted according to Eq. (1.45).

This also means that for any two modes a and b with $\Delta m = b - a$, similar characteristics are shifted by $\Delta m \cdot f_{\mathrm{rot}}$. Thus, a cross-correlation of the two mode spectra

$$\int_{-\infty}^{\infty} p^*(a, f) \cdot p(b, f + \Delta m\, f_{\mathrm{rot}})\, \mathrm{d}f \equiv (p(a, f) \star p(b, f))(\Delta m\, f_{\mathrm{rot}}) \tag{1.46}$$

yields a maximum for those $(\Delta m\, f_{\mathrm{rot}})$, at which the frequency f_{rot} corresponds to the rotational speed of a source present in the measured data. The cross correlation ($\star$) in Eq. (1.46) can also be written as a convolution ($*$), which can be transformed into a product using the Fourier transform:

$$\begin{aligned} p(a, f) \star p(b, f) &= p(a, f) * p(b, -f)^* \\ &= p(a, f) * p(-b, f) \\ &= \mathcal{F}_f^{-1}(\mathcal{F}_f(p(a, f)) \cdot \mathcal{F}_f(p(-b, f))) \\ &= \mathcal{F}_f(\mathcal{F}_f^{-1}(p(a, f)) \cdot \mathcal{F}_f^{-1}(p(-b, f))) \\ &= \mathcal{F}_f(p(a, t) \cdot p(-b, t)) \; . \end{aligned} \tag{1.47}$$

This means that information about occurring rotational speeds can be determined simply by applying a DFT after the multiplication of time signals in the mode domain.

The achievable frequency resolution depends not only on the sampling rate, but also on the length of the time segment under consideration. The longer the time signal, the higher the achievable frequency resolution. However, if it is desired to also detect temporal fluctuations of the rotational speed, shorter time segments have to be used, which reduces the frequency resolution. On the other hand, the effective resolution of the rotational speeds increases with higher distances between the mode pairs, since the discretely found maximum is divided by Δm to finally obtain the rotational speed. In general, an evaluation of several mode pairs per considered time interval can improve the detection by combining the respective single spectra to an overall result.

For this purpose, the following procedure is proposed: The signals are first transformed into the mode-time domain and divided into time segments which may overlap. Prior to further processing, it may be necessary to apply high-pass filtering [56]. Then, equation (1.47) is calculated for several Δm and the respective mode pairs. Depending on Δm, different multiples of the actual rotational speeds are found. For combining these, the frequency resolution of the results from lower Δm is increased according to the highest one considered. This can be done by suitable interpolation techniques, such as the Whittaker-Shannon interpolation mentioned in section 1.2.1. It can be implemented here simply by appending zeros to the time signal before the DFT [25].

Require: $p(m,t), \boldsymbol{\Delta m}, i_{f,\min}, i_{f,\max}$ ▷ sound pressure ($M \times N_\mathrm{s}$ matrix), regarded mode differences (vector), indices for frequency limits
$p(m,t) \leftarrow \text{high pass}(p(m,t))$ ▷ get rid of noisy low-frequency data
$N_\mathrm{s} \leftarrow \text{length}(p(m,t))$ ▷ number of time samples
$A_f[i_{f,\min} \dots i_{f,\max}] \leftarrow \mathbf{0}$ ▷ intitialize rotational speed amplitudes with zeros
for all Δm in $\boldsymbol{\Delta m}$ **do**
  $\boldsymbol{p}_a, \boldsymbol{p}_{-b} \leftarrow$ mode pairs with Δm ▷ identify suitable pairs, ascending order
  $N_m \leftarrow$ number of mode pairs
  $\boldsymbol{p}_{\Delta m} \leftarrow \boldsymbol{p}_a \circ \boldsymbol{p}_{-b}$ ▷ element-wise multiplication
  $N_\mathrm{s,new} \leftarrow \lfloor N_\mathrm{s} \cdot \max(\boldsymbol{\Delta m}) / \Delta m \rfloor$ ▷ number of samples after zero-padding
  $\boldsymbol{p}_{\Delta m} \leftarrow \text{zero-padding}(\boldsymbol{p}_{\Delta m}, N_\mathrm{s,new} - N_\mathrm{s})$
  $\boldsymbol{P}_{\Delta m} \leftarrow \mathcal{F}_f(\boldsymbol{p}_{\Delta m})[i_{f,\min} \dots i_{f,\max}]$ ▷ use subrange from DFT result with rotational speeds of interest
  $w_\varphi \leftarrow 0$
  for $n = 1 \dots N_m - 1$ **do**
    $\Delta\varphi_P(f) \leftarrow \arg(P_{\Delta m,n}(f) \cdot P_{\Delta m,n+1}(f)^*)$ ▷ calculate phase shifts for all f
    $w_\varphi \leftarrow w_\varphi + |\Delta\varphi_P|$ ▷ sum absolute phase shifts
  end for
  $\boldsymbol{P}_{\Delta m,\mathrm{abs}} \leftarrow |\boldsymbol{P}_{\Delta m}| / \operatorname{Median}_f(|\boldsymbol{P}_{\Delta m}|)$ ▷ normalize amplitudes by median along f
  $A_f \leftarrow A_f + 1/w_\varphi \cdot \sum_{n=1}^{N_m} P_{\Delta m,\mathrm{abs},n}$ ▷ sum and weight result for this Δm and add to overall result
end for
Return: A_f ▷ rotational speed spectrum

Algorithm 1.3. The rotational speed detection method.

The magnitude values of the obtained spectra are now summed for each Δm. This corresponds to an arithmetic averaging without normalization with the number of samples. Since only relative values (i. e. the position of the maxima) are of interest for finding the rotational speeds, the normalization step can be omitted. Instead, each spectrum is normalized with its own median. Under the assumption that with only a few occurring discrete speeds the median lies within the range of background noise, the maxima of the mode pairs are weighted more strongly where the detected speeds emerge more clearly from the background.

For adjacent mode pairs (e. g. for $\Delta m = 2$: $(4,6)$ and $(5,7)$), the phases of the complex amplitudes at the rotational speeds lie close to each other, while the phase at frequencies away from the speed is generally arbitrary. This can be exploited by determining and averaging the difference in phase frequency response for all adjacent mode pairs, resulting in minima at the rotational speeds. Those can the be used to reciprocally weight the summed magnitude spectrum for a better signal-to-noise ratio.

Algorithm 1.3 summarizes the proposed signal processing for determining rotational speeds.

1.5. Summary and interaction of the methods

The methods presented in this chapter allow different variants of concatenated processing of acoustic signals. Based on sound pressure time data measured at several positions on a ring, stationary and rotating sources can be mapped, occurring rotational speeds can be determined, and acoustic spectra can be cleaned from interfering influences.

Figure 1.6 shows possible links between the different data processing blocks. The input blocks are highlighted in green, intermittent signal processing in yellow, and red indicates the final data processing step for a desired output. For display purposes, no distinction between necessary and optional input is made here; e. g. the steering vector calculation always requires the microphone positions $\boldsymbol{x}_l$ and focus grid positions $\boldsymbol{x}_s$ as input, whereas information on a rotation of the medium is only needed if it has to be taken into account. Furthermore, some interconnections, such as the $\mathcal{F}_m$ blocks for the transformation into the mode domain depending on the array geometry $\boldsymbol{x}_l$, have been left out for better clarity. The application of CLEAN-SC is not explicitly mentioned but can be done together with the beamforming methods in the frequency domain.

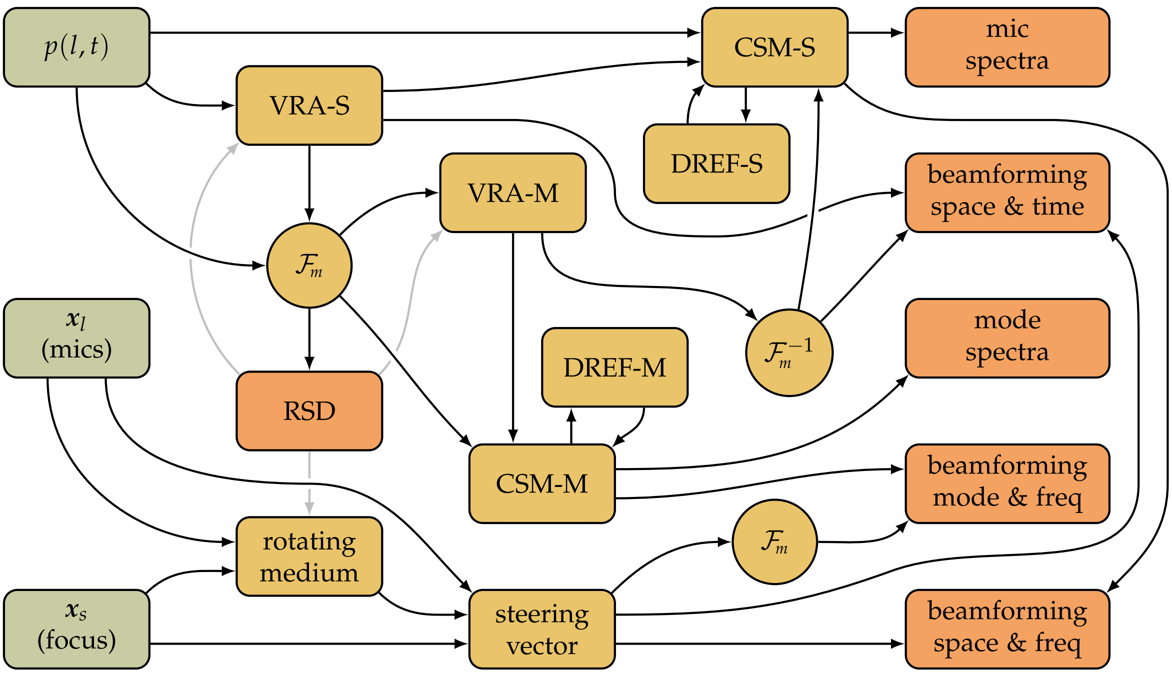

Figure 1.6. Diagram with possible data processing chains of the presented methods.

An exemplary conventional signal processing chain consists of the direct transformation of the measurement data into the frequency domain for the calculation of the CSM-S, the determination of the steering vectors from the microphone positions together with the selected focal points and subsequent beamforming in the frequency domain. If the data set contains rotating sources which are to be mapped, the calculation of the CSM can be preceded by a transformation into the mode domain with subsequent application of the new virtual rotation method (VRA-M) and transformation back into the spatial domain. Before beamforming, the now rotating medium in the reference frame has to be taken into account in the calculation of the steering vector.

For information about whether a data set contains rotating and/or stationary sources, the sound pressure time data can be used for rotational speed detection (RSD) after transformation into the mode domain. As indicated by the gray arrows in Fig. 1.6, it is conceivable to use the speeds determined in this way for the virtual rotation. For the VRA evaluations carried out here, however, rotational speeds derived from trigger signals were used, as this also yields the current angular position.

If the overall spectral characteristics in the sound field are of interest, but the measurements suffer from noisy microphone data, e. g. because they are positioned within the flow, this noise can be reduced in the output by calculating the CSM-S, applying the proposed diagonal reconstruction method DREF-S, and averaging the resulting microphone spectra. Similarly, rotation noise due to sources rotating at speeds different from those currently observed can be filtered out using the CSM-M and DREF-M with subsequent averaging of the mode spectra.

The application of some signal processing chains to several simulated and measured data sets featuring rotating data sets is described in Chapter 3.

2. The Two Fans

Simulated and Measured Data

In the following sections, several simulated and experimental data sets containing rotating sources are described. All measurements and simulations were performed with arrays consisting of microphones evenly distributed on a ring. With the help of the data sets introduced here, the procedures described in Chapter 1 are tested with respect to their applicability in Chapter 3.

2.1. Simulated data sets

In order to perform accurate qualitative as well as quantitative investigations, data with known source distributions are generated by simulation. The used configuration as well as the basic parameters of the first described data set correspond to the “Microphone Array Benchmark b11 – Subcase a” for rotating sources [57]. The software *Acoular* [58, 59] is used to simulate the data as well as for later evaluation.

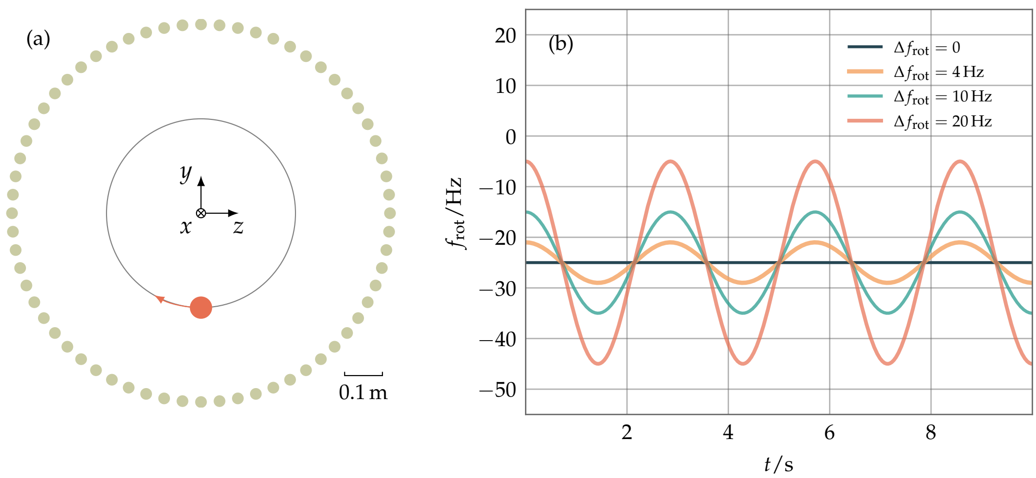

Figure 2.1. Simulated data set “Sim-1”: (a) Schematic of the basic simulation setup. Microphones in light green, source in red. (b) Temporal modulation of the rotational speed for exemplary Δf_{rot}.

The setup consists of an array of 64 microphones uniformly distributed on a ring (diameter $d_{\mathrm{array}} = 1\,\mathrm{m}$). The sources travel on circular trajectories in a plane 0.5 m away and parallel to the ring. The sources are simulated as monopoles, each emitting uncorrelated white noise. They rotate about the same axis around which the microphones are arranged.

Figure 2.1a shows the basic scenario described in the *b11* benchmark, which will be referred to as "Sim-1" here. On the radius $r_{\mathrm{source}} = 0.25\,\mathrm{m}$, a source rotates clockwise with the constant rotational speed of 1500 rpm, or, with the rotation direction being defined positive in counter-clockwise direction here, $f_{\mathrm{rot}} = -25\,\mathrm{Hz}$. From this, the following studies are derived, each varying one parameter to investigate its respective influence:

- Sim-1a: radius of the circular path of the source
- Sim-1b: number of microphones in the ring
- Sim-1c: temporal modulation of the rotational speed

The time-dependent modulation of the rotational speed is shown in Fig. 2.1b for exemplary amplitudes. The modulation frequency is $f_{\mathrm{mod}} = 0.35\,\mathrm{Hz}$. The variation is sinusoidal, and it deviates from the mean rotational speed up to $\Delta f_{\mathrm{rot}} = 20\,\mathrm{Hz}$. The time dependent rotation angle is then calculated via [60]

$$\varphi(t) = 2\pi f_{\mathrm{rot}} \cdot t + \frac{\Delta f_{\mathrm{rot}}}{f_{\mathrm{mod}}} \sin(2\pi f_{\mathrm{mod}} \cdot t) \ . \tag{2.1}$$

A tacho signal is generated for tracking the rotation, providing a peak at each full revolution.

For further investigations, simulated data sets featuring four sources of different rotational speed are used. One of the sources is stationary, another is moving counter-clockwise and two are moving clockwise, with one of them rotating with slightly varying speed. This scenario "Sim-2" is shown in Fig. 2.2 and has been used in a similar form for previous speed detection experiments [56]. In the initial setup, all sources radiate white noise at the same level. In sub-scenario Sim-2a, the level of source 4 is varied to be up 20 dB below that of the other sources. For scenario Sim-2b, all sources are simulated with a different spectral characteristic, as shown in Fig. 2.2b.

The parameters of the simulations as well as their variation are summarized in Table 2.1.

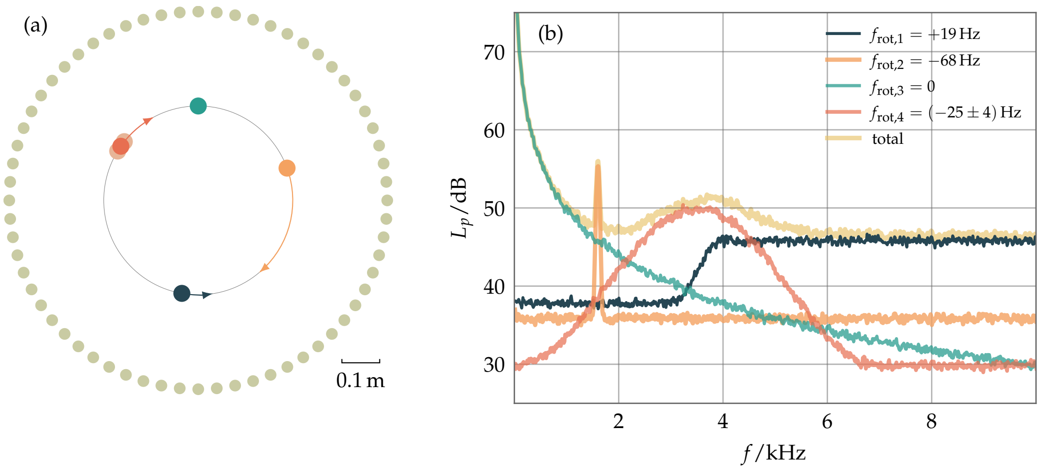

Figure 2.2. Simulated data set "Sim-2": 4 point sources with different rotational speeds (see Table 2.1). (a) Schematic view of the setup (y-z plane). (b) Stationary spectral characteristics of the sources in Sim-2b, averaged over all microphones.

Table 2.1. Parameters of the simulated data sets.

microphone array	$M = 64^*$
	$d_{\mathrm{array}} = 1\,\mathrm{m}$
	center aligned with rotational axis
sampling rate	$f_s = 48\,000\,\mathrm{Hz}$
signal	$10\,\mathrm{s}$, white noise*
	$L_p(1\,\mathrm{m}) = 94\,\mathrm{dB}^*$
tacho signal	1 trigger per revolution
environment	freefield
speed of sound	$c = 343\,\frac{\mathrm{m}}{\mathrm{s}}$
distance to source plane	$0.5\,\mathrm{m}$
source track radius	$r_{\mathrm{source(s)}} = 0.25\,\mathrm{m}^*$
rotational speed	$f_{\mathrm{rot}} = -25\,\mathrm{Hz}^*$ ↻
*Standard value is changed in some simulations.	
Sim-1	one rotating source
Sim-1a	$0 \leq r_{\mathrm{source}} \leq 0.61\,\mathrm{m}$
Sim-1b	$3 \leq M \leq 128$
Sim-1c	$f_{\mathrm{rot}} = -25\,\mathrm{Hz} \pm \Delta f_{\mathrm{rot}}$
	$0 \leq \Delta f_{\mathrm{rot}} \leq 20\,\mathrm{Hz}$
Sim-2	4 rotating sources
	$f_{\mathrm{rot,1}} = +19\,\mathrm{Hz}$ ↺
	$f_{\mathrm{rot,2}} = -68\,\mathrm{Hz}$ ↻
	$f_{\mathrm{rot,3}} = 0\,\mathrm{Hz}$
	$f_{\mathrm{rot,4}} = (-25 \pm 4)\,\mathrm{Hz}$ ↻
Sim-2a	$L_{p,4} = L_{p,[1,2,3]} + \Delta L_{p,4}$
	$-20\,\mathrm{dB} \geq \Delta L_{p,4} \geq 0\,\mathrm{dB}$
Sim-2b	spectra see Fig. 2.2 (right)

2.2. Measurements of a fan under freefield conditions

As part of a measurement campaign in the axial fan test chamber at Friedrich-Alexander University Erlangen-Nürnberg, a forward-skewed axial fan with nine blades was measured acoustically at various operating points [11]. The measurements took place in a standardized test rig constructed according to DIN EN ISO 5801 [61], shown in Fig. 2.3. The walls as well as the ceiling are lined with sound-absorbing material. The operating point of the fan is adjustable via an auxiliary fan and a butterfly damper.

Similar to the simulation setup, the microphone array consists of 64 microphones arranged in a ring. The ring diameter is 1 m; the array plane is 0.45 m away from the fan hub and 0.5 m away from the blade center plane (see Fig. 2.4).The methodology for the design of the fan and its blades is described in detail by Zenger et al. [62]. Important parameters are summarized in Table 2.2.

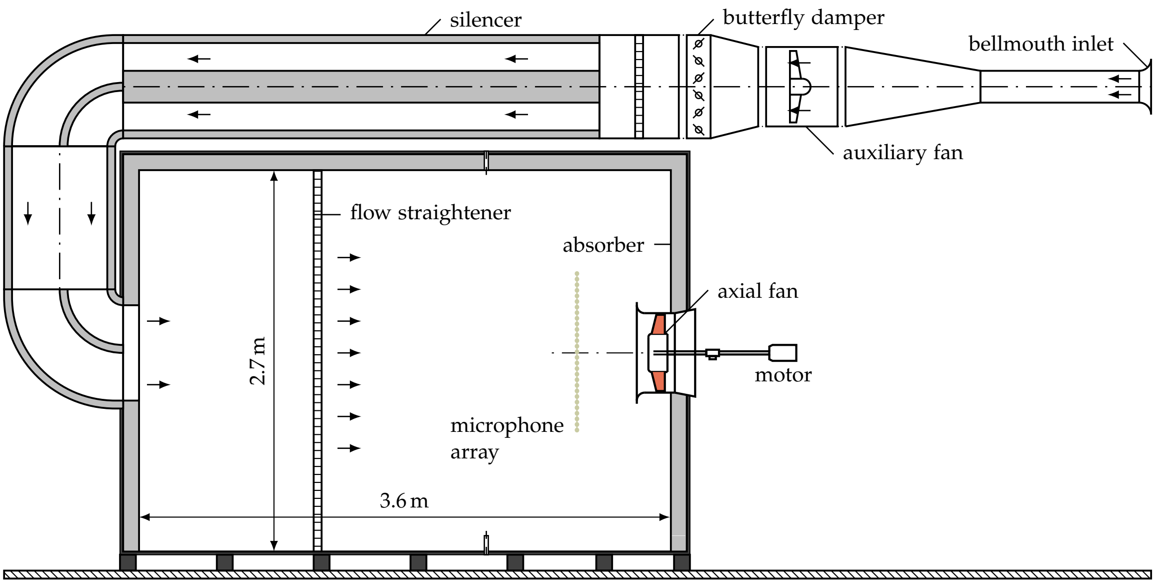

Figure 2.3. Schematic representation of the freefield fan test rig [9].

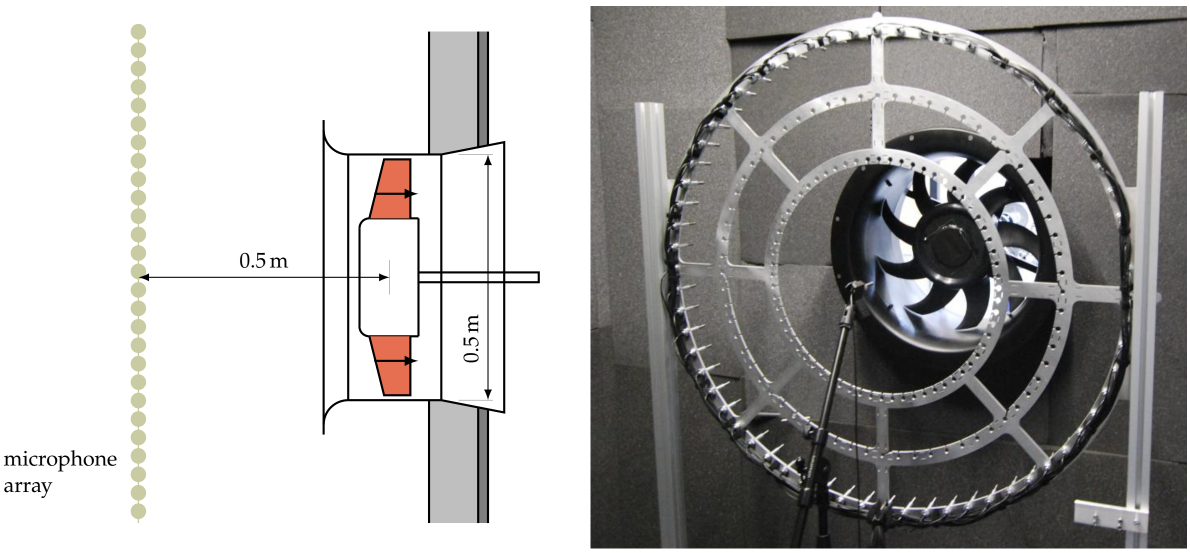

Figure 2.4. Setup of the microphone array with the freefield fan [11].

The flow rate coefficient is a dimensionless measure of the volume flow $\dot{V}$ and is given by

$$\Phi = \frac{4\,\dot{V}}{\pi^2 \cdot {d_{\mathrm{fan}}}^3 \cdot f_{\mathrm{rot}}} \,. \tag{2.2}$$

At the design operating point, the flow rate coefficient is $\Phi = 0.18$ and the efficiency is close to its maximum. At lower flow rates, stalls can occur at the leading edges of the blades, which can result in increased noise generation [9, 11]. Here, measurements at the flow rate coefficients $\Phi_1 = 0.18$ and $\Phi_2 = 0.105$ are evaluated.

Table 2.2. Important parameters of the experimental data sets.

	freefield fan	**ducted fan**
microphone array	$M = 64$	$M = 47$
	axially centered ring	wall-mounted ring
	$d_{\mathrm{array}} = 1\,\mathrm{m}$	$d_{\mathrm{duct}} = 0.4536\,\mathrm{m}$
sampling rate	$f_{\mathrm{s}} = 48\,000\,\mathrm{Hz}$	$f_{\mathrm{s}} = 65\,536\,\mathrm{Hz}$
measurement time	30.5 s	60 s
tacho signal	1 trigger per revolution	1 trigger per revolution
environment	semi-freefield	cylindrical duct, $Ma = 0.04$
speed of sound	$c = 348.5\,\frac{\mathrm{m}}{\mathrm{s}}$	$c = 343.4\,\frac{\mathrm{m}}{\mathrm{s}}$
distance to rotor plane	0.5 m	0.2 m
rotor (stator)	9 blades (4 struts)	$B = 18\ (V = 32)$
	$d_{\mathrm{fan}} = 0.495\,\mathrm{m}$	$d_{\mathrm{rotor}} = 0.4524\,\mathrm{m}$
	$d_{\mathrm{hub}} = 0.248\,\mathrm{m}$	$d_{\mathrm{hub}} = 0.2805\,\mathrm{m}$
tip clearance	2.5 mm	0.6 mm
flow rate coefficient	$\Phi_1 = 0.18, \Phi_2 = 0.105$	$\Phi = 0.19$
rotational speed f_{rot}	−24.8 Hz ↻	+50.024 Hz ↺

2.3. Measurements of a fan in a cylindrical duct

As part of a measurement campaign of the German Aerospace Center (DLR), measurements were carried out on a low-speed axial fan stage. The fan consists of a rotor with 18 blades and a stator with 32 vanes and is part of a ducted fan test rig shown in figures 2.5 and 2.6. The channel is about 8 m long and has an anechoic termination at the outlet.

The section containing the 47 microphones and the rotor has a diameter of 453.6 mm. The wall-flush mounted microphones are arranged in a ring at a distance of 200 mm from the rotor plane. The rotor has a diameter of 452.4 mm and a hub-to-tip ratio of 0.62. It rotates at a rotational speed of about 50 Hz. Table 2.2 summarizes the configuration parameters.

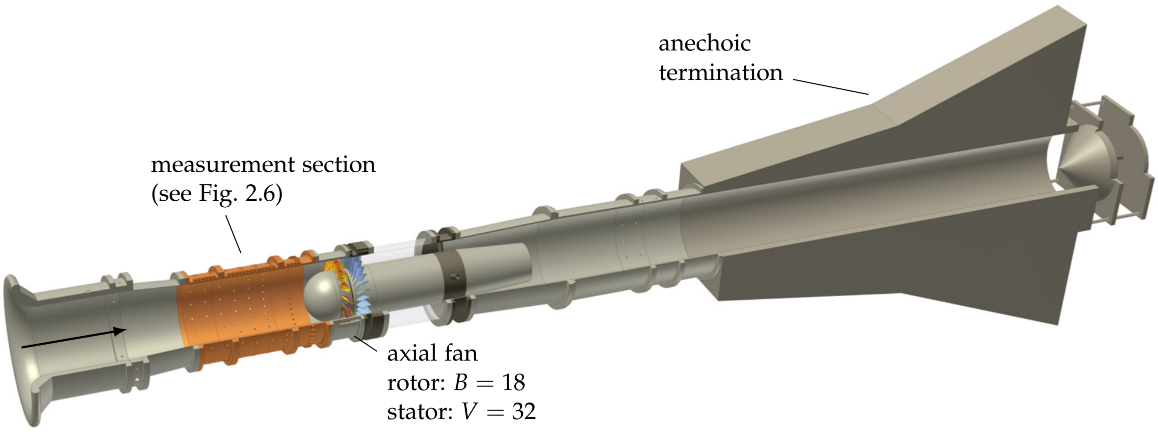

Figure 2.5. Schematic of the ducted fan test rig (total length: ca. 8 m) [63].

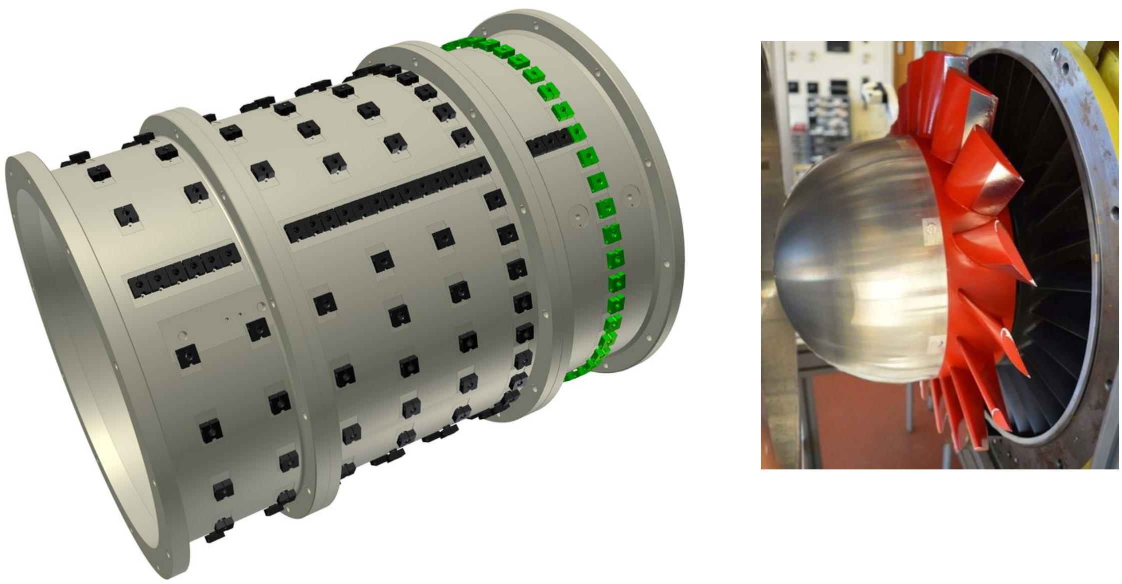

Figure 2.6. Measurement section and view of the rotor [64]. Used microphone positions depicted in green.

3. The Return of the Ring

Applications and Results

In the following sections, the methods and algorithms introduced in Chapter 1 are applied to the data sets described in Chapter 2. First, the general capability of the virtual rotating array methods are demonstrated and their limits of application are investigated in section 3.1. In section 3.2 , the algorithm for the rotational speed detection is validated by using it to reproduce known rotational speeds in the data sets. Furthermore, it is applied to measured data sets where not all rotations were tracked, identifying additional rotating source mechanisms. Finally, section 3.3 demonstrates the application of the diagonal reconstruction algorithm for the separation of sources and spectral characteristics.

3.1. Application of the VRA algorithms

The virtual rotating array methods – in spatial or mode domain – promise to translate rotating sources into a reference frame where these sources can be regarded as stationary. As is shown in the following, both methods work in principle. They are, however, subject to limitations due to the finite spatial sampling of the sound field. These limitations shall be studied using the simulated data sets in section 2.1.

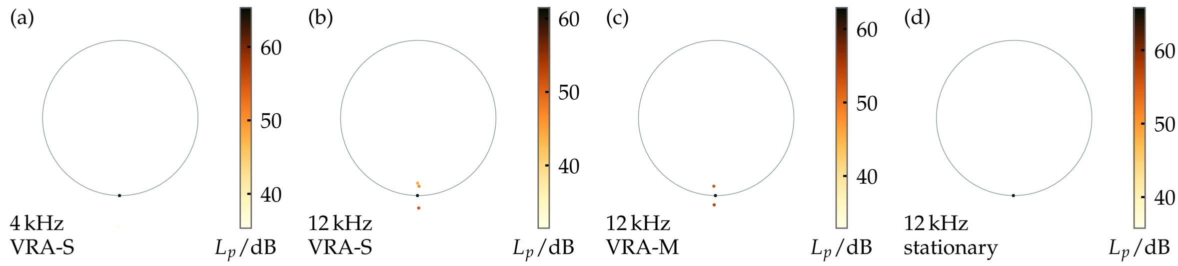

Figure 3.1. CLEAN-SC sound maps for the case Sim-1 (a-c), evaluated with VRA-S und VRA-M at two different frequencies (11.72 Hz narrow band). (d) stationary sound map for non-moving source. The thin ring marks the path of the rotating sources.

One case where the VRA methods fail is illustrated in Fig. 3.1. It shows exemplary sound maps of one rotating broadband point source (Sim-1) calculated with the CLEAN-SC algorithm. Applying the VRA in the spatial domain appears to work fine at a frequency of 4 kHz, where the source is found as a distinct point at its correct position. However, at 12 kHz (Fig. 3.1b), artefacts at lower and higher radii appear, and the source at the actual position exhibits a lower level, indicating energy leakage at this frequency. The same qualitative effect can be seen when processing the data with VRA in the mode domain (Fig. 3.1c). For comparison, the same data processing and evaluation at 12 kHz without the virtual rotation is done on a stationary source with the same characteristics in Fig. 3.1d. Here, the artefacts are absent, pointing to the VRA processing as their origin. Similar effects have been demonstrated earlier [14, 65].

One objective of this study is to not only identify artefacts as such but to investigate (and later predict) under which circumstances they appear. For this, an abstract measure of the "failing" of the method is needed. Such a measure is provided by the *specific level error* [38], which is defined by the difference between sound pressure level as summed over a chosen source area in a sound map and the expected sound pressure level within this area:

$$\Delta L_{p,\mathrm{s}} = L_{p,\mathrm{integrated}} - L_{p,\mathrm{expected}} \; . \tag{3.1}$$

The area for integration of the level here is selected to be a circle of 5 cm diameter. If less energy is found in the integration area than is expected from the source, the value of $\Delta L_{p,\mathrm{s}}$ becomes negative. With the simulations evaluated here, the maximum possible level error is $\Delta L_{p,\mathrm{s}} = 0\,\mathrm{dB}$, which indicates a good source reconstruction.

Another measure for the performance of the VRA method is the CSM coherence [16]:

$${\gamma_{ij}}^2 = \frac{|C_{ij}|^2}{C_{ii} \cdot C_{jj}} \tag{3.2}$$

For each frequency, this yields a $M \times M$ matrix of values between 0 and 1, where values below 1 in a noise-free CSM indicate a loss of coherence between channels. With the simulated data sets regarded here, an occurrence of low values means that the virtual rotation is no longer capable of interpolating correct values at all microphones at this frequency. For an easy understanding of when the VRA fails, not all M^2 coherence values are regarded individually. Instead, only their "worst" one percent, i. e. the first percentile $\gamma_{P_{1\%}}$, is selected to be representative for the performance.

Important parameters for the data processing and evaluation are summarized in Table 3.1.

Table 3.1. Evaluation parameters for FFT and beamforming.

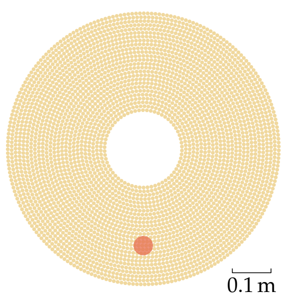

FFT block size (sim, freefield)	4096 (narrow band 11.72 Hz)
FFT block size (ducted fan)	16384 (narrow band 4 Hz)
FFT window	von Hann, 50 % overlap
focus grid	annulus in the rotor plane
resolution	$\Delta yz \approx 0.01\,\mathrm{m}$
extent (see left)	$r_{\mathrm{min}} = 0.1\,\mathrm{m},\ r_{\mathrm{max}} = 0.35\,\mathrm{m}$
extent for Sim-1a (var. r_{source})	$r_{\mathrm{min}} = 0\,\mathrm{m},\ r_{\mathrm{max}} = 0.66\,\mathrm{m}$
integration area sim.	$d_{\mathrm{int}} = 0.05\,\mathrm{m}$
steering vector	sim: Eq. (1.8), fan: Eq. (1.9)
CLEAN-SC loop gain	0.6

3.1.1. Influence of the radial source position on VRA + beamforming

If a omnidirectional point source was positioned directly at the center of rotation, all sensors would see the exact same signal. Any virtual rotation would therefore work perfectly, as only identical values were interpolated. As has been shown above, with sources on a circular trajectory, however, the virtual rotation fails for higher frequencies.

For a detailed overview how the performance of the VRA methods depending on the radius is, Sim-1a with varied source trajectory radius (see section 2.1) is evaluated with the two VRA methods and CLEAN-SC. With the knowledge of the source position, the resulting sound maps are evaluated using the specific level error. The results are shown in Fig. 3.2a & b. In addition to the color scale of $\Delta L_{p,s}$, the theoretic VRA-specific Nyquist frequency limit according to Eq. (1.39) is plotted in green.

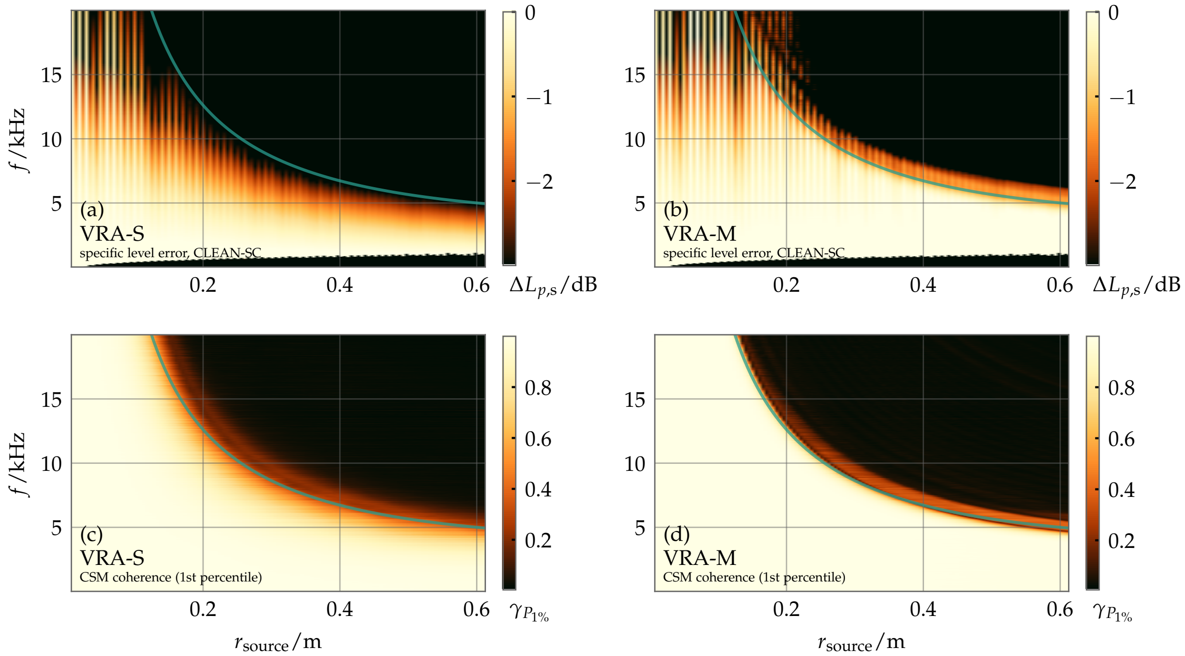

Figure 3.2. Application limits of the VRA methods depending on radial source position (Sim-1a), evaluated with 2 different metrics. Light areas mark a good performance of the method. Green lines: theoretic frequency limit according to Eq. (1.39).

In general, both the specific level error and the theoretic frequency limit are in accordance with each other: the higher the radial position of the source, the lower the maximum frequency where a successful detection can be expected. Furthermore, it appears that the frequency limit as indicated by the level error is a little higher for the VRA-M method than for VRA-S. Two other phenomena can be seen: over a broad range of radii, the level error suddenly drops for frequencies below about 1 kHz, and for higher frequencies, it repeatedly decreases and increases for every other radial position. The reason for both is the evaluation using CLEAN-SC. The former is caused by CLEAN-SC's poor performance at low frequencies [38]. To explain the latter phenomenon, it shall be noted here that the radius variation step lies below the distance of neighboring focus points (on is about half the other). This means it repeatedly happens that the exact source position is not part of the discrete set of focus points. However, CLEAN-SC only looks for beamforming maxima at these points. The reconstructed level is then significantly underestimated for higher frequencies, as the “width” of the beam narrows with increasing frequency, leading to lower levels at positions that do not coincide with the exact source location.

The evaluation of the CSM coherence criterion confirms these findings (Fig. 3.2c & d). The grid-/beamforming-specific artefacts are not present here, and the theoretic frequency limit is a good approximation of the actual VRA limitation. VRA-S shows a coherence loss earlier than VRA-M, the latter following the theoretic limit almost exactly. It appears, however, that at higher radii, the theoretic limit is predicting a higher frequency for the VRA method to still be working than actually is the case.

3.1.2. Influence of the number of microphones on VRA + beamforming

Intuitively, it can be said that, the higher the number of microphones used, the better the VRA methods will work, as less “guessing” through interpolation is necessary. This section is concerned with estimating the minimum number of microphones required for a given frequency of interest.

The simulations for this were done with a source moving on a circle with a radius of $r_{\mathrm{source}} = 0.25\,\mathrm{m}$. As is shown in the previous section, the maximum evaluable frequency also depends on this. However, the general findings are expected to still be applicable. The number of microphones in the simulations were varied from $M = 3$ up to $M = 128$ (Sim-1b). The results for the specific level error and the CSM coherence are shown in Fig. 3.3.

The theoretic frequency limit predicts a linear relation between the maximum resolvable frequency and number of microphones. For the VRA-M method, the prediction fits well with the CSM coherence (Fig. 3.3d). For higher frequencies / number of microphones, the CSM coherence suggests that the method will fail at frequencies slightly lower than the theoretically predicted limit. Regarding the specific level error, there is an apparent region (between 10 Hz - 15 Hz / 25 - 50 microphones) where the reconstruction seems to somewhat “work again” (Fig. 3.3b). As this lies within a region where the CSM is no longer reliable, this can be considered an false positive due to coincidental artefacts within the integration area for the specific level error.

The performance of VRA-S method is inferior to that of VRA-M here as well. Moreover, while the upper frequency limit does increase with higher number of microphones, the slope is not as steep as that of the theoretically achievable frequency limit (Fig. 3.3a & c).

3.1.3. Influence of rotational speed variation on VRA + beamforming

In realistic measurements, it is not always possible to keep the rotational speed perfectly constant. Therefore, it is of interest how a varying rotational speed might affect the reconstruction result. This is investigated with Sim-1c, where the rotational speed is varied between $f_{\mathrm{rot}} \pm \Delta f_{\mathrm{rot}}$.

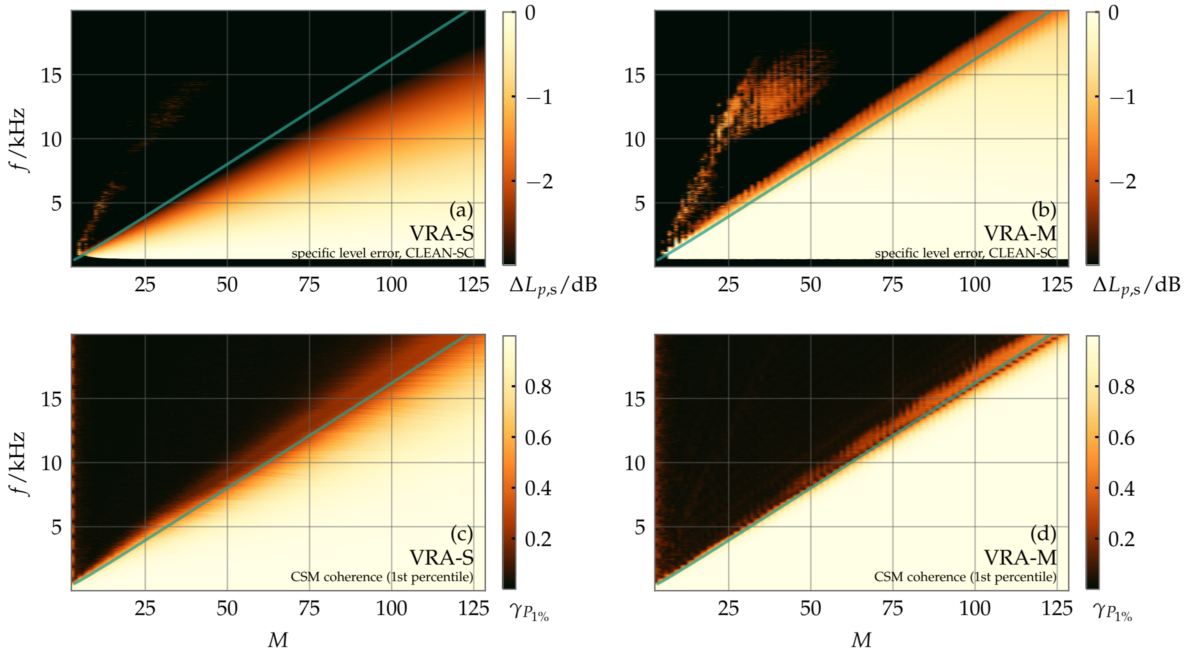

Figure 3.3. Application limits of the VRA methods depending on number of microphones (Sim-1b), evaluated with 2 different metrics. Light areas mark a good performance of the method. Green lines: theoretic frequency limit according to Eq. (1.39).

It shall be noted that while the virtual rotation is capable of taking into account a varying rotational speed, only an average rotation of the medium can be considered for the evaluation with frequency domain beamforming methods. Furthermore, the specific implementation of the VRA-M method used for the evaluation estimates the angular position of the virtual array at the time the recorded or simulated signal starts by extrapolating the rotational speed detected after the first trigger instant back in time. In the simulations here, the first trigger is set to occur after half a revolution. Thus, the estimate of the initial angle deviates with increasing rotational speed variation, leading to an angular offset of the detected source location. This is compensated here by shifting the integration area according to this offset. As the rotational speed variation of the measured cases is well below 0.1 %, this is of no concern for the experimental data sets.

In Fig. 3.4, the specific level error and CSM coherence are displayed depending in frequency and rotational speed variation Δf_{rot}. As in the the evaluations in the previous sections, the VRA-S method starts to fail at lower frequencies than VRA-M, which works well up to the theoretic frequency limit in most cases.

Regarding the dependence on the speed variation, performance dips occurring about every 3 Hz in the $\Delta L_{p,s}$ evaluation can be observed (Fig. 3.4a & b). These appear when the angular offset of the source localization passes from one discrete focus point to the next, causing CLEAN-SC to detect a lower level. This is similar to the decreased levels described in section 3.1.1.

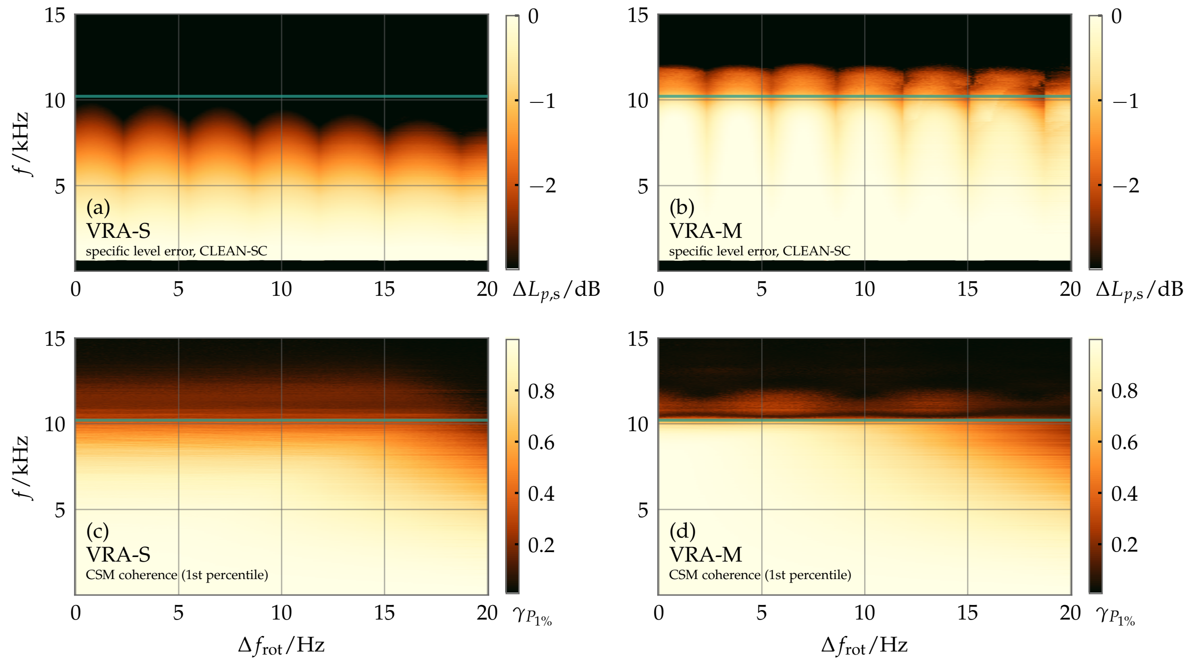

Figure 3.4. Application limits of the VRA methods depending on the rotational speed variation (Sim-1c), evaluated with 2 different metrics. Light areas mark a good performance of the method. Green lines: theoretic frequency limit according to Eq. (1.39).

The CSM coherence remains constant up to $\Delta f_{\text{rot}} \approx 10\,\text{Hz}$, above which it starts to decrease at higher frequencies (Fig. 3.4c & d). This shows that the virtual rotating array method can produce reliable results even with significantly varying rotational speed, given that the rotation is permanently tracked.

3.1.4. VRA & beamforming of the freefield fan

For a demonstration of the capability of the VRA-M method with subsequent beamforming applied to experimental data, a measurement of the freefield fan (see section 2.2) at its design flow rate coefficient $\Phi = 0.18$ is evaluated. Figure 3.5 shows an exemplary sound map at the 4 kHz third-octave band as well as integrated spectra for the leading and trailing edge subregions.

In the sound map, the major sound emission at the displayed frequency band can be identified to originate from the tip region of the blades, mostly towards the leading edges. Further source regions are visible at the leading edges close to the hub, extending towards the blade centers. These and further phenomena as well as possible underlying sound generation mechanisms have been discussed in earlier publications [10, 11], where the VRA-S method was employed. Additional sound maps are shown in the appendix in section F.2.

Integrating the calculated sound energy over regions of interest allows the plotting of region-specific spectra, which is done in Fig. 3.5 for the leading and trailing edge regions of the fan

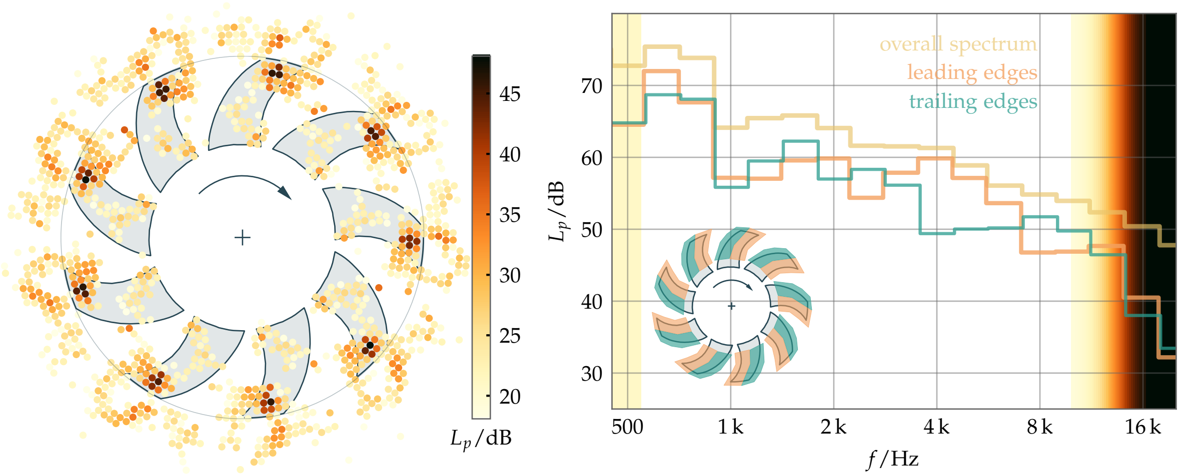

Figure 3.5. Fan in freefield, $\Phi = 0.18$, VRA-M, CLEAN-SC. Left: sound map (4 kHz third-octave band). Right: Integrated third-octave band spectra of leading and trailing edges (integration areas indicated). Values in shaded frequency ranges not reliable.

blades. This helps identifying the dominant source region for each frequency band. In the case at hand, for instance, the leading edges are major contributors to the sound emission between 3 kHz and 6 kHz, whereas between 8 kHz and 10 kHz, the trailing edge regions dominate. A more detailed discussion, evaluating the results for further blade geometries and under different operating conditions has been done in a publication using the VRA-S method [11]. There, the limits of application of the VRA method are visible as well, however could not be identified as clearly as it is now possible with the investigation done in section 3.1.1.

The frequencies at which a reliable evaluation of the map is no longer possible are highlighted in the spectrum here by the shaded frequency ranges. At the 500 Hz third-octave band, the CLEAN-SC algorithm is not capable of finding all sources at their correct position with the used array setup. The light-to-dark gradient on the right marks the frequencies where the VRA-M method is not longer reliable because of the radial position of the sources: At 9.9 kHz, the blade-tip part of the integration sectors reaches the theoretical frequency limit for the 64-channel microphone ring, and at 16.4 kHz, the entirety of the sectors lies outside the radius where the virtual rotation works without aliasing.

3.1.5. VRA & spectra of the ducted fan

The transformation from the spatial into the mode domain plays an important role in duct acoustics, as the azimuthal modes constitute eigenforms of the sound field in a cylindrical duct [66]. The principle of the virtual rotation in the mode domain can be nicely illustrated via the mode spectra as shown in Fig. 3.6. Here, the data of the ducted fan measured with a ring of 47 microphones (see section 2.3) is transformed from the space-time into mode-frequency domain.

The features that can be seen in the spectra are similar to those in the mode sound power spectra calculated by Tapken et al. [63] and Behn et al. [67] – from the same measurement, but using a different set of sensors. The most prominent features are the cut-on frequencies,

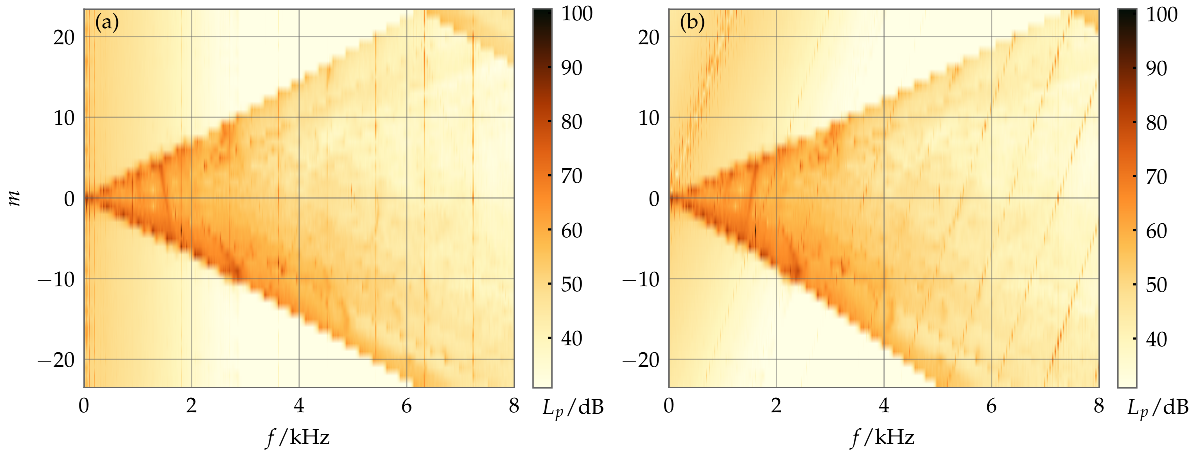

Figure 3.6. Narrow band mode spectra of the ducted fan in (a) the stationary and (b) the rotating frame of reference ($f_{\mathrm{rot}} = 50\,\mathrm{Hz}$).

i. e. for each mode the frequency above which that mode can propagate (and carry energy) in the duct. This frequency is higher for higher mode orders. Below the cut-on frequency, the mode amplitude decreases exponentially along the duct. The decay also scales with the frequency, which is visible in the mode spectra, as below the cut-on frequencies, the levels are lower with increasing frequency.

Furthermore, the spectra shown in Fig. 3.6a exhibit additional cut-on characteristics above 6.5 kHz within already propagating modes. These are believed to belong to higher mode orders which cannot be spatially resolved by the used array and thus lead to aliasing [21].

In Fig. 3.6a, the multiples of the blade-passing frequency (BPF) at 900 Hz are well visible as tonal components present in multiple modes. These tones become diagonally distributed with the rotor-synchronous virtual rotation in the mode domain, as positive modes are shifted to higher frequencies and negative modes to lower frequencies. This can be seen in the according mode spectra shown in Fig. 3.6b. By contrast, there can now be seen an alignment of tones at 1.6 kHz and, more faintly, at its multiples. This is the vane passing frequency (VPF), which occurs because in the now rotating frame of reference, the stator is moving and the rotor is stationary [8].

Another distinct feature in the mode spectra is a narrow band region at around 1.5 kHz for $m = 0$, which is visible in all cut-on modes but does not align in either the stationary or rotating frame of reference. The dis-alignment is, however, exactly reversed for both domains, indicating a source mechanism rotating at about half of the speed of the fan. Tapken et al. [63] suggested this to be caused by flow separations at the rotor hub or by turbulences carried downstream from the air intake.

For a better understanding of the sound field composition in the duct and the origin of occurring tonal components, the f_{rot}-f diagram can be of use [13]. It can be generated by virtually rotating the data not only with the rotor speed, but with a number of evenly distributed rotational speeds. The resulting mode spectra are then summed over the modes for each rotational speed and the sound pressure levels are represented depending on the

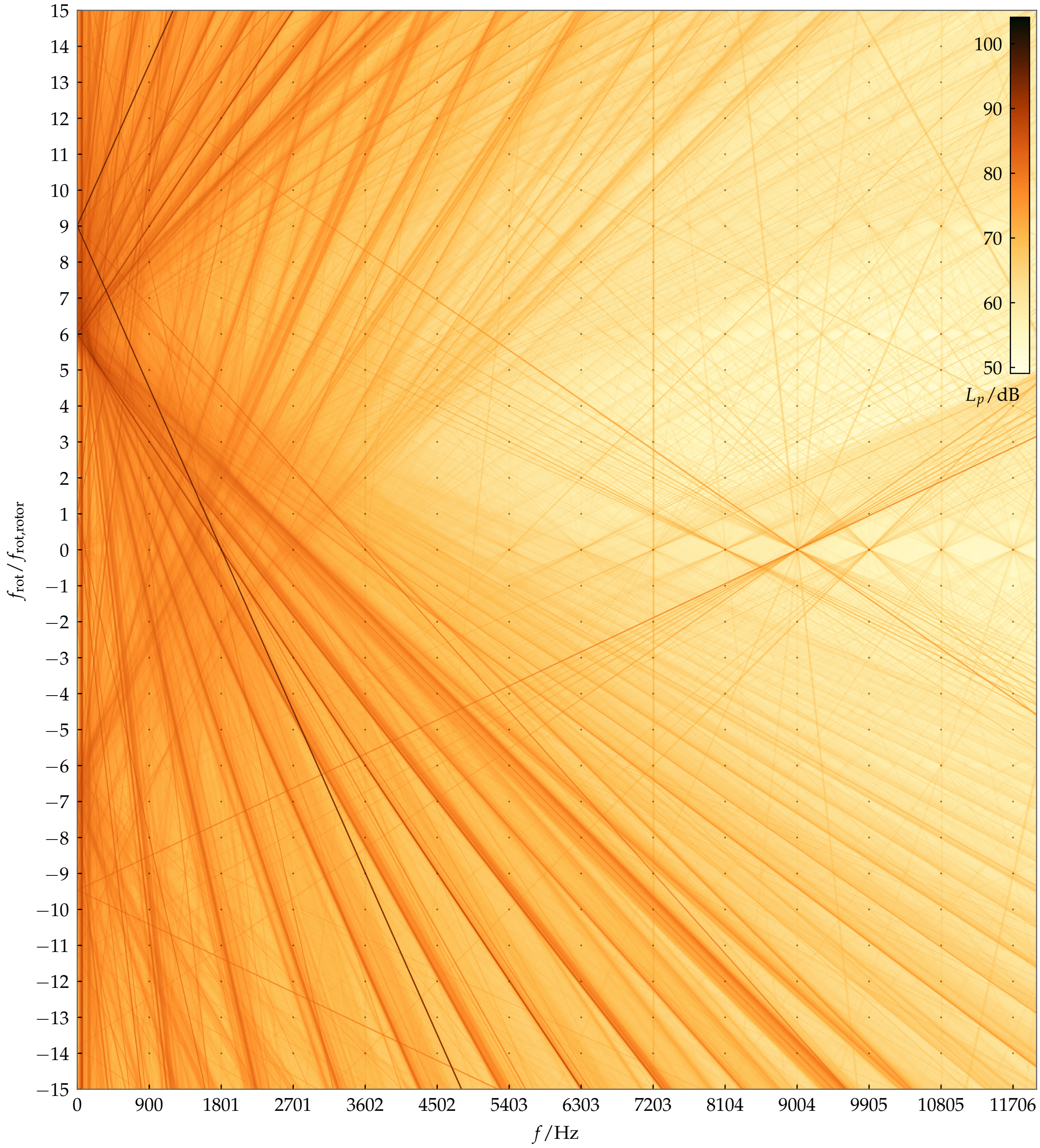

Figure 3.7. f_{rot}-f diagram of the ducted fan. The ticks on the x-axis mark the BPF and its multiples, the ticks on the y-axis mark the rotor speed multiples.

frequencies on the x- and the rotational speeds on the y-axis. For the case at hand, this diagram is displayed in Fig. 3.7.

The visible features have been discussed in detail previously [13]. The lines in this diagram are associated with tonal components carried by a mode. The slope of each line is specific to a mode.

The diamond-shaped features around $f_{\mathrm{rot}} = 0$ at frequencies above 6 kHz are artefacts that can be attributed to aliasing due to the limited spatial resolution of the sound field measurement. Tones "converging" towards a rotational speed in several modes indicate a sound generating mechanism rotating with that speed. Most prominent are:

- $f_{\mathrm{rot}} = 9 \cdot f_{\mathrm{rot,rotor}}$: Tyler-Sofrin mode[2] $m = -4$
- $f_{\mathrm{rot}} = 6 \cdot f_{\mathrm{rot,rotor}}$: multiple modes, dominant $m = -6$
- $f_{\mathrm{rot}} \approx -6 \cdot f_{\mathrm{rot,rotor}}$, $f_{\mathrm{rot}} \approx -7 \cdot f_{\mathrm{rot,rotor}}$

Minor tonal components can also be seen originating from $f_{\mathrm{rot}} = 1 \cdot f_{\mathrm{rot,rotor}}$ and $f_{\mathrm{rot}} = 0$ Rotational speeds of broadband components are not as easily identified in this diagram. Their detection is discussed in section 3.2.3.

3.2. Application of the rotational speed detection

In the following sections, the rotational speed detection (RSD) as described in section 1.4 shall be applied to simulated and measured data sets. The RSD algorithm allows several parameters, whose respective influence on the performance will not be discussed in detail here. Instead, an exemplary set of parameters is chosen, and the calculated detection results will be discussed.

Table 3.2. Parameters for the time-dependent RSD evaluations.

	simulations & freefield fan	ducted fan
frequency resolution	$\Delta f = 0.2$ Hz	$\Delta f = 0.2$ Hz
f_{rot} detection range	-500 Hz ... 500 Hz	-700 Hz ... 700 Hz
time step	$\frac{1}{48}$ s (1000 samples)	$\frac{1}{64}$ s (1024 samples)
time segment length	$\frac{1}{5}$ s (9600 samples)	$\frac{1}{4}$ s (16384 samples)
max. mode considered	± 26	± 22
Δm considered	$(1, 3, 5, 7, 9)$	$(1, 3, 5, 7, 9)$
high pass	2500 Hz	0 Hz / 10 000 Hz

The parameters used for the RSD calculations are summarized in Table 3.2. The choice of parameters follows some general guidelines:

1. The duration of the time segments used for a single RSD is selected to be longer than the time between instants for subsequent detections. This leads to data evaluated multiple times in overlapping blocks. Larger segments allow a higher frequency resolution and a better signal-to-noise ratio (SNR), whereas short time steps allow a fine-grained detection of sources that change their rotation over time.

[2] As described by Tyler and Sofrin [66], duct modes excited by rotor-stator interactions can be calculated by $m = n\,B + k\,V$ and the respective rotational speed of the mode via $f_{\mathrm{rot},m,n} = \frac{n\,B\,f_{\mathrm{rot,rotor}}}{m}$. The factors n and k are arbitrary integers, e. g., the mode $m = -4$ is excited with $(n, k) = (-2, 1)$.

2. Multiple modes are considered, as they all are expected to hold information on the rotation. The highest modes may be omitted, however, as aliasing effects could become important here (see also section 3.1.5).

3. Higher mode-pair deltas (Δm) may be considered, as this increases SNR as well as the effective frequency resolution (by factor of Δm). However, choosing Δm to high will also lead to aliasing effects. Furthermore, a high number of considered deltas significantly increases the calculation time.

4. Since in actual measurements, rotational speeds might be masked by dominant non-rotating sources or reflections [56], applying a band pass filter to select frequencies where less disturbances are expected can be of value.

5. The purpose of the limited f_{rot} detection range is mainly the efficient handling of computer memory. However, since in the RSD algorithm the median of the data is used as a "base line", it should be made sure that the range limits sufficiently exceed the expected rotational speeds.

3.2.1. RSD on simulated data

For the simulated data sets, the rotational speeds of all sources are exactly known. However, for the following evaluations, at no point apart from verification purposes was this information ever used.

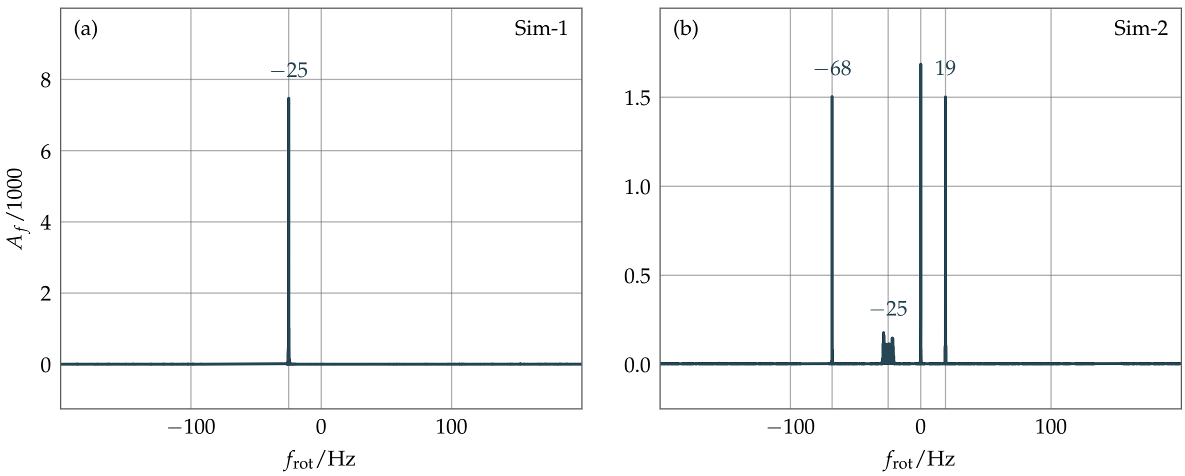

Figure 3.8. RSD for the simulated cases with (a) one (Sim-1) and (b) four rotating sources (Sim-2). Here, one time segment of 10 s duration is considered.

In Fig. 3.8, simulated data sets with one rotating source (Sim-1) and four different rotating sources (Sim-2) are evaluated applying the RSD method on a single time segment containing the whole signal duration (10 s). The "amplitude" of the rotational speed A_f is a relative measure, indicating how significantly the respective rotational speed emerges from the background noise.

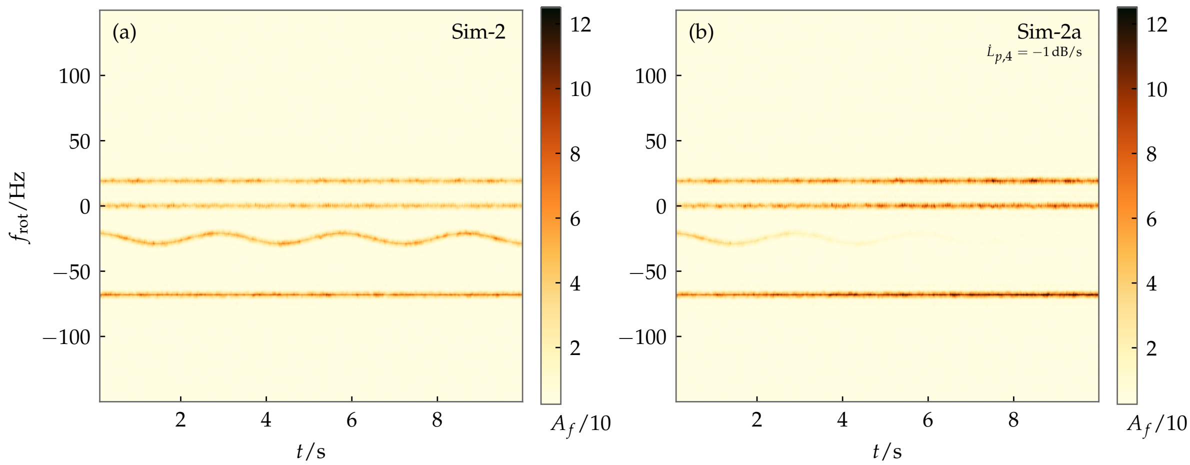

Figure 3.9. Time-dependent RSD for the cases (a) Sim-2 and (b) Sim-2a (source 4 level decreasing by 1 $\frac{\mathrm{dB}}{\mathrm{s}}$). Evaluation parameters in Tab. 3.2.

For the case of a single rotating source emitting white noise (Fig. 3.8a), a strong peak at $f_{\mathrm{rot}} = -25\,\mathrm{Hz}$ can be identified, which corresponds to the rotational speed used in the simulations. With four independently rotating sources, all occurring speeds can be detected as well (Fig. 3.8b). Even thought all sources are simulated with the same level and distance to the microphones, the calculated RSD amplitudes differ. The stationary source at $f_{\mathrm{rot},3} = 0\,\mathrm{Hz}$ is found with the highest amplitude ($A_f = 1700$). The two sources rotating at $f_{\mathrm{rot},2} = -68\,\mathrm{Hz}$ and $f_{\mathrm{rot},1} = 19\,\mathrm{Hz}$ share the same amplitude with $A_f = 1500$. The non-rotating source yielding a higher amplitude can be assumed to be due to a high correlation when the mode spectra are not shifted against each other, so that de-correlations due to, for instance, aliasing effects at high frequencies have no influence here. For non-stationary sources, artefacts in the stationary spectrum will lead to lower RSD amplitudes. The source with a varying rotation of $f_{\mathrm{rot},4} = (25 \pm 4)\,\mathrm{Hz}$ is detected with a much lower amplitude, which is self-evident given that it only rotates at any one speed only for a fraction of the signal duration.

RSD evaluations using shorter successive time segments are shown in Fig. 3.9, revealing the temporal progression of the rotational speeds occurring in two simulated data sets featuring four sources. Figure 3.9a evaluates case Sim-2, where all sources radiate at the same level throughout the time. While the detected f_{rot} peaks are not as sharp as when evaluating the entire time in one segment, the rotational speeds are still well distinguishable. Moreover, the time-dependent variation of the rotational speed of source 4 can clearly be seen.

In Fig. 3.9b, the RSD performance is investigated for case Sim-2a, where the level of the white noise signal from source 4 is varied. In this case, the level is decreased by 1 dB per second to get a continuous impression of how good secondary sources can be detected. It can be seen that the rotational speed of the source remains visible up to 6 dB below the levels of the other sources. It has to be kept in mind, however, that a white noise signal is not the typical case for realistic sources. It is therefore conceivable to also detect rotational speeds of minor sources using appropriate bandpass filters around frequencies at which these sources are expected to be dominant.

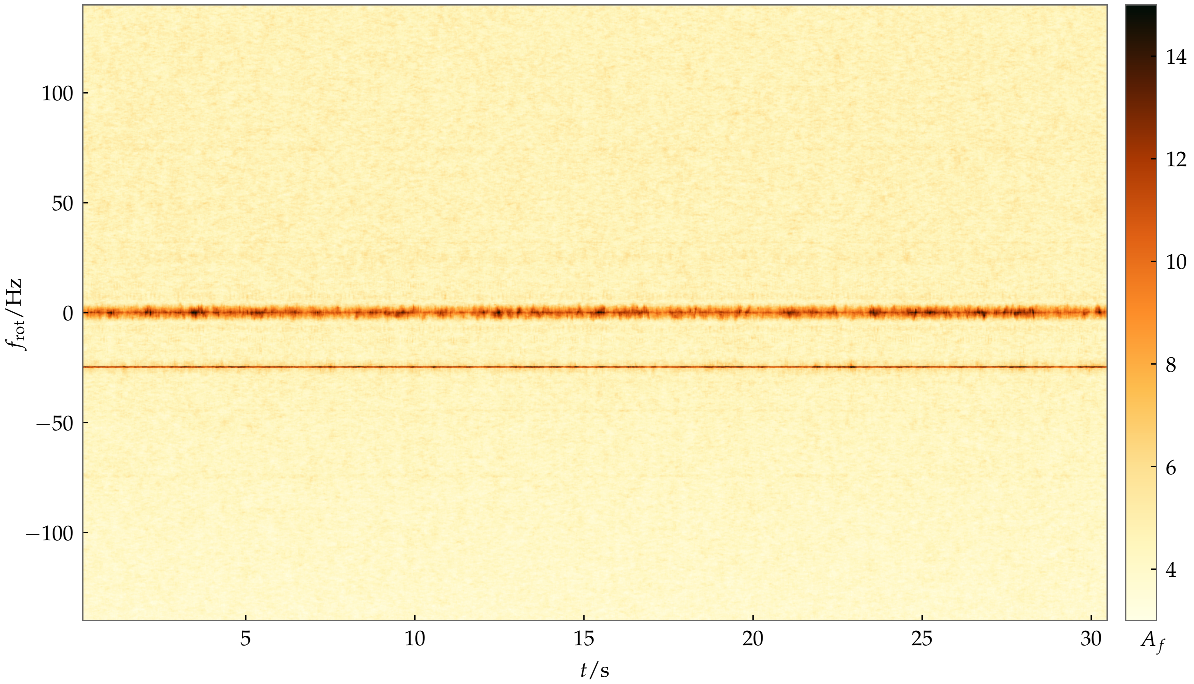

Figure 3.10. Time-dependent RSD for the freefield fan operating at its design point ($\Phi = 0.18$). Evaluation parameters in Table 3.2.

3.2.2. RSD on the freefield fan

Rotational speed detection is done for the fan measured under freefield conditions at two different operating points.

In Fig. 3.10, the RSD result is shown for the operation at a flow rate coefficient of $\Phi = 0.18$, which marks the fan's design point. For the considered frequency range above 2.5 kHz, two kinds of sources are dominant: stationary or almost non-moving sources ($f_{\mathrm{rot}} \approx 0\,\mathrm{Hz}$) and sources rotating at 24.8 Hz, which is identical to the rotational rate measured via the trigger signal. As can be seen, the rotational speed of the fan remains constant throughout the entire 30 s measurement.

At a flow rate coefficient of $\Phi = 0.105$, the occurrence of stalling is to be expected [11]. The corresponding RSD diagram is shown in Fig. 3.11. Apart from stationary sources and sources rotating with the fan, it can be seen that non-continuous sources rotating with a little less than half the speed of the fan occur. This can happen when flow separations from one blade lead to detachment of the flow of the following blades, which results in a rotating stall [56]. Kameier and Neise [68] pointed out that a fully developed rotating stall constitutes a "frozen" flow field without much variation of the stall cell over time. Even though at $\Phi = 0.105$, the fan is operating far in the stall region, thus making the occurrence of such a cell likely, the rotation of the stall phenomena appears to be transient in time. Similar phenomena with intermittently occurring rotations were described by Inoue et al. [69], though in connection with only mild stall conditions.

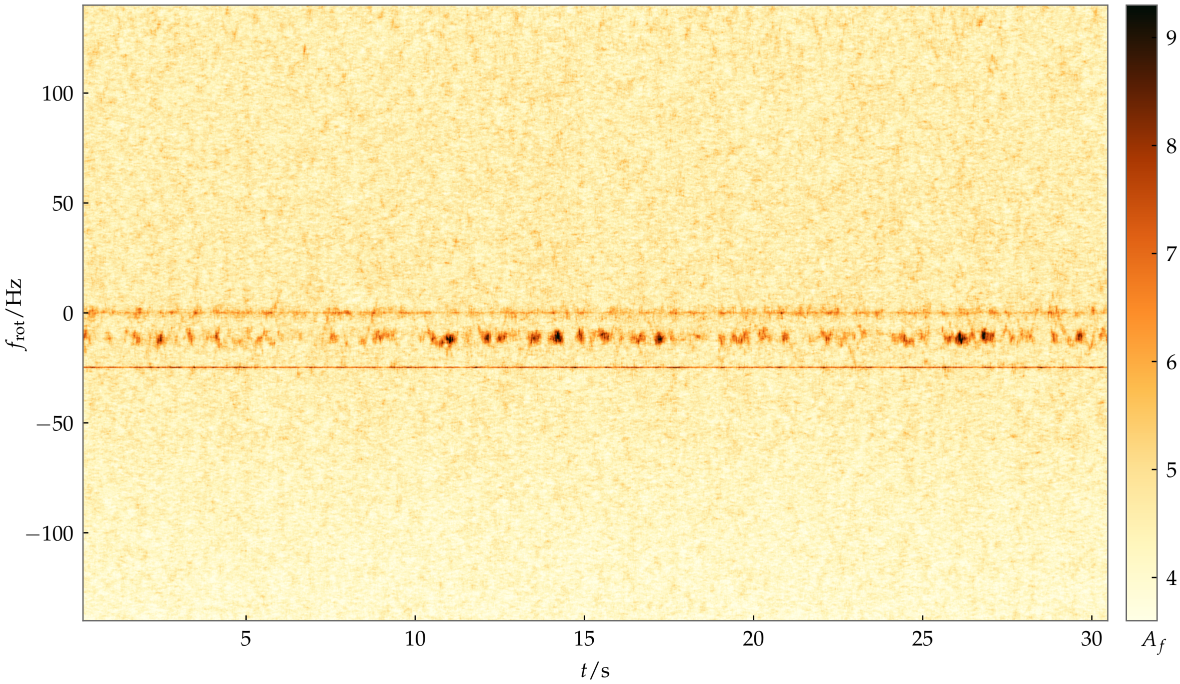

Figure 3.11. Time-dependent RSD for the freefield fan operating in the stall region ($\Phi = 0.105$). Evaluation parameters in Table 3.2.

With the RSD method, the repeated onset of the rotating flow separations and their duration can be tracked via their acoustic signatures.

3.2.3. RSD on the ducted fan

The sound field in a cylindrical duct can be expressed as a superposition of differently rotating mode patterns [66]. Therefore, a detection of rotational speeds can be expected to yield several frequencies, representing the respective spinning modes.

Figure 3.12 shows the detected rotational speeds for the sound field generated by the ducted fan over a period of 60 seconds. It can be seen that all acoustically visible rotating features are continuous. The displayed upper range limit is clipped at 10.5 for a better visualization of occurring rotational speeds aside from 0 Hz, which is dominant with $A_f > 30$. If the whole spectrum is used for the RSD (Fig. 3.12a), the most prominent patterns aside from stationary sources rotate at $f_{rot} = 301$ Hz, which corresponds to $6 \cdot f_{rot,rotor}$, and at $f_{rot} = 257.5$ Hz. With approximately $5.15 \cdot f_{rot,rotor}$, the latter rotating phenomenon is not a direct multiple of the rotor speed. Furthermore, while centered at $5.15 \cdot f_{rot,rotor}$, some acoustic energy is distributed to rotational speeds around that frequency. In the f_{rot}-f diagram (Fig. 3.7), no tonal lines originate at this frequency, hinting to this being a broadband effect.

If only frequencies above 10 kHz are taken into account for the RSD (Fig. 3.12b), the noisiness disappears and other rotational speeds become important. Stationary sources are still dominant here, followed by the $f_{rot} = \pm 301$ Hz sources and sources rotating synchronously with the rotor at $f_{rot} = 50$ Hz.

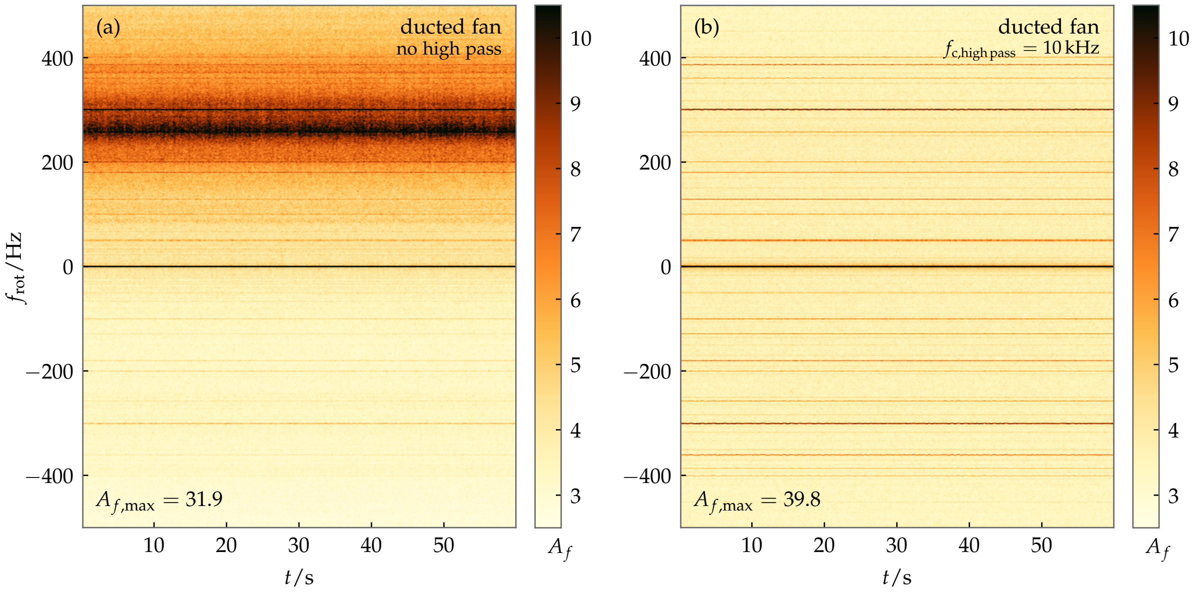

Figure 3.12. Time-dependent RSD of the ducted fan (a) without band pass and (b) with 10 kHz high pass. Further evaluation parameters in Table 3.2.

3.3. Separation of features with different rotational speeds

As has been established, it is common that in practical measurements, rotating and stationary sources, or even multiple features with different rotational speeds, occur at the same time. Using virtual array rotation for transforming moving phenomena into the stationary domain can help with their visualization, as is shown in section 3.1. However, features not rotating at the same rate still introduce unwanted "rotation noise", which may significantly affect the result.

In the following sections, these effects are demonstrated with the help of the simulated and measured data sets. Moreover, the application of the CSM de-noising method (see sec. 1.1.5) for removing rotation noise is investigated. The data processing for this is:

1. transforming the time data from spatial into mode domain
2. performing the virtual rotation with VRA-M
3. calculating the CSM in the mode domain
4. de-noising the CSM with DREF-M.

Subsequent beamforming is also done in the mode domain. If only spectra are evaluated, these are averaged over all channels, i. e. microphones or modes.

3.3.1. Separation of simulated rotating sources

Separation of source locations

The effect multiple occurring rotational speeds have on beamforming results is demonstrated in Fig. 3.13. Two simulated data sets are evaluated here: Sim-1c with one source and Sim-2a with four sources. Both data sets have one source with identical rotation and level in common. In Sim-2a, rotation noise caused by the three sources not rotating at the regarded rotational speed of $f_{\mathrm{rot}} = (25 \pm 4)\,\mathrm{Hz}$ is present (see sec. 2.1). With $\Delta L_{p,4} = -10\,\mathrm{dB}$, the source of interest radiates below each of the other sources. The evaluation is done with VRA-M and frequency-domain beamforming at the third-octave band around 4 kHz. The thin bluish ring marks the radial position of the sources. The displayed dynamic range includes levels down to 15 dB below the respective maximum.

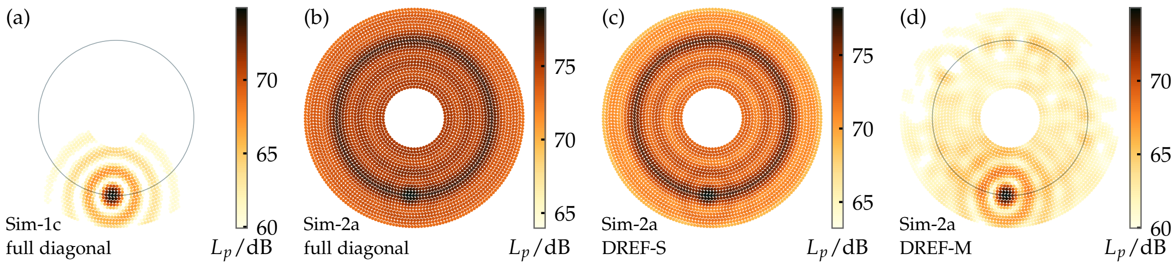

Figure 3.13. Beamforming sound maps at 4 kHz third-octave, VRA-M. (a) Sim-1c with 1 rotating source ($\Delta f_{\mathrm{rot}} = 4\,\mathrm{Hz}$), (b-d) Sim-2a with 4 rotating sources and rotation with source 4 ($\Delta L_{p,4} = -10\,\mathrm{dB}$), (b) full diagonal, (c) DREF-S, (d) DREF-M.

Figure 3.13a shows the beamforming result from the single-source data set for reference. Since no deconvolution method like CLEAN-SC was used, artefacts like side lobes and the extended width of the source are visible. The beamforming was done in the spatial domain; however, the result of a calculation in the mode domain is identical – as is the result with the diagonal reconstruction method – since no spurious noise or other rotating sources are present in this data set.

In Fig. 3.13b, the exact same data processing is applied for the case with rotation noise caused by the three additional sources. All sources rotate at the same radius, which manifests in the dark ring at $r = 0.25\,\mathrm{m}$. The position of the source of interest at 6 o'clock is still visible. However, due to the rotation noise, the dynamic range along the source trajectory ring is much lower, and the maximum level of the source is increased. The "smearing" of the beamforming artefacts of the relatively moving sources also leads to a generally decreased dynamic in the map.

Figure 3.13c shows the result obtained using the CSM in the spatial domain (CSM-S) with diagonal reconstruction (DREF-S). While the general dynamic range appears to be a little higher and the maximum level is a little decreased, the map is qualitatively highly similar to the result calculated with the original CSM diagonal. The broad ring caused by the three additional sources is still visible and the achievable dynamic is well below the displayed 15 dB.

If the CSM diagonal reconstruction is done on the CSM-M, i. e. the CSM calculated from time data in the mode domain, the removal of rotation noise is a lot more effective, as predicted in section 1.1.5. This is shown in Fig. 3.13d, where Sim-2a with 4 sources is evaluated after applying DREF-M. The source of interest is clearly visible here, with similar beamforming artefacts to the case with only a single rotating source. While the dynamic range is not as high as for Sim-1c, it is significantly increased. The rotation noise ring is no longer visible as such. Along the sources' trajectory, several artefacts about 10 dB below the maximum still remain visible. The maximum level itself is the same as in the case of on source, indicating the removal of a significant part of the rotation noise.

The capability of the DREF-M method for the removal of rotation noise is visualized qualitatively in Fig. 3.14 for different $\Delta L_{p,4}$. The evaluation is similar to that in Fig. 3.13. in that the same beamforming methods are applied for the same frequency band (4 kHz, third-octave). Here, however, the focus area is constrained to the circle containing the sources' radial positions, whose angles are plotted on the x-axis. The source of interest is positioned at $\varphi = 270°$. On the y-axis, the variation of $\Delta L_{p,4}$ from 0 to −20 dB is indicated. The resulting maps are normalized to the respective maximum.

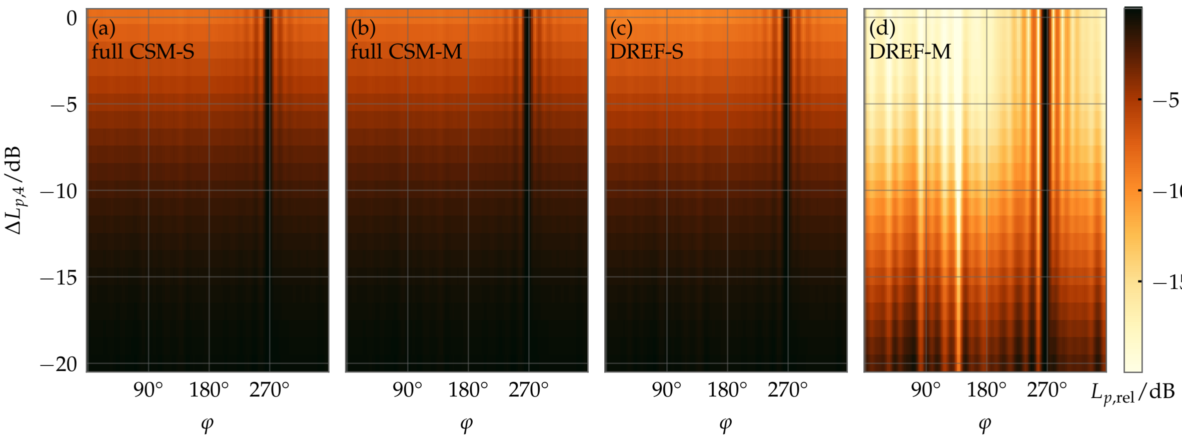

Figure 3.14. Sim2a (4 sources, varying $\Delta L_{p,4}$): 1D beamforming sound maps for one focus ring at $r = 0.25$ m. Evaluated at 4 kHz third-octave using VRA-M and different CSM calculation methods. Results stacked vertically and normalized per row ($\Delta L_{p,4}$) to the respective maximum in the map.

As mentioned earlier, the beamforming results are exactly the same in the spatial and the mode domain if the original CSM diagonal is used for the calculations (Fig. 3.14a & b). While the source of interest is still easily visible down to $\Delta L_{p,4} = -7$ dB, it is not as easily detected below $\Delta L_{p,4} = -10$ dB and is practically masked by rotation noise below $\Delta L_{p,4} = -15$ dB.

A CSM diagonal reconstruction in the spatial domain has little to no effect regarding the removal of rotation noise, as can be seen in Fig. 3.14c, which is almost identical to the cases using the original CSM.

As expected, the calculation with the DREF-M method yields a better qualitative separation of the source of interest (see Fig 3.14d). The dynamic range for every $\Delta L_{p,4}$ is much higher than in the other cases, and the source remains visible well below $\Delta L_{p,4} = -15$ dB, albeit with several artefacts appearing at lower $\Delta L_{p,4}$.

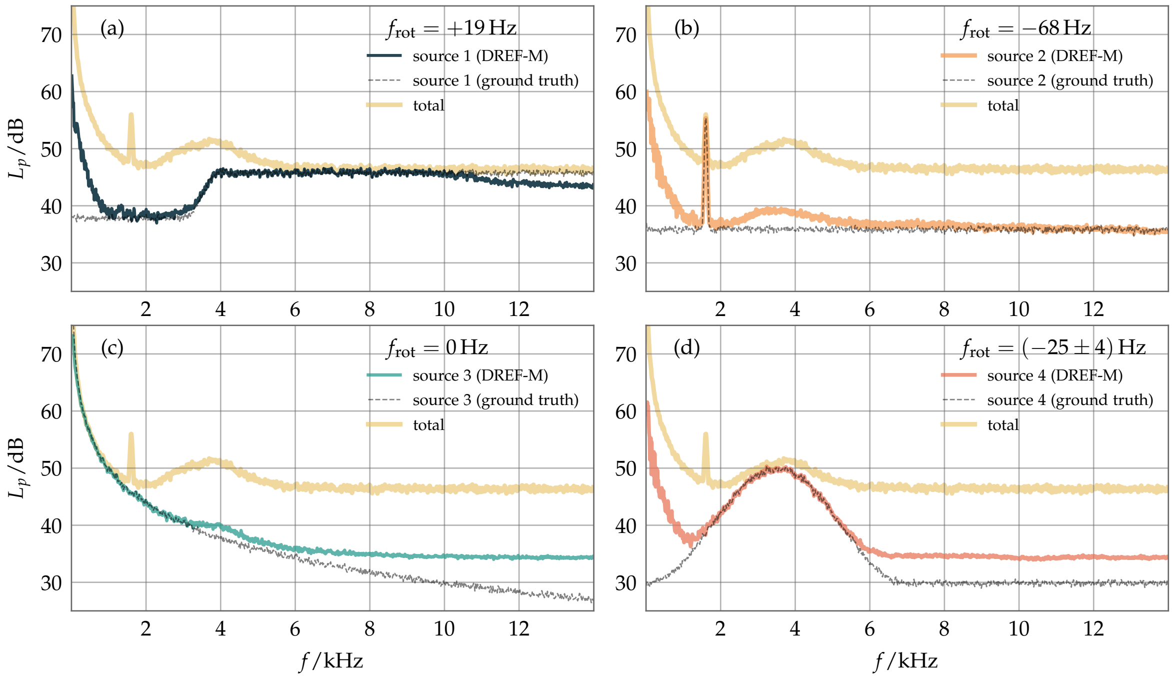

Figure 3.15. Sim-2b – source-specific narrow-band spectra calculated using VRA-M and DREF-M.

Separation of spectral characteristics

If spectral characteristics rotating at a distinct speed are of interest but no explicit spatial separation of synchronously rotating sources is needed, it is not necessary to use beamforming methods. Instead, the direct evaluation of the CSM in the mode domain denoised using the DREF-M method suffices. For each frequency, the reconstructed CSM diagonal entries are averaged to obtain the squared sound pressure.

This is done for the simulated data set Sim-2b, which consists of four sources with different rotational speeds and individual spectral characteristics (see also Fig. 2.2b). The resulting reconstructed spectra are shown in Fig. 3.15. Dashed gray lines indicate the spectral characteristic with which the respective source was simulated. Yellow curves show the overall spectrum as measured by the microphones. The other colors are the spectra as reconstructed with DREF-M at the rotational speed indicated at the upper right corner of each plot.

As can be seen, the spectra reconstruction is successful for levels up to about 12 dB below the overall level. This is most prominently visible for low frequencies, where the contribution of stationary source 4 is high. The level increase for lower frequencies is present in all reconstructed spectra, even if not part of the initial signal. By contrast, the narrow-band peak around 1.6 kHz from source 2 is successfully removed for the other sources, but perfectly reconstructed at the according rotational speed (Fig. 3.15b).

It is worth mentioning that the spectra reconstruction is limited at higher frequencies as well. This can be seen in Fig. 3.15a, where the reconstructed level for frequencies above 10 kHz drops below the ground truth. The underlying reason for this are the limitations of the VRA-M method, which were investigated in section 3.1 (e. g. see Fig. 3.2d). A possible solution for resolving higher frequencies would be to use a higher number of microphones (see Fig. 3.3d). For a better "signal-to-rotation-noise" ratio, i. e. the reconstruction of spectral features that lie more than 12 dB below the overall spectrum, a higher number of averaging elements to get a better CSM approximation is necessary. This can be achieved by decreasing the FFT block size or by using a longer duration of the evaluated signal, as is demonstrated in the appendix section F.1.

3.3.2. Separation of measured rotating sources

Source localization after rotational speed separation: freefield fan

The impact rotation noise filtering using DREF-M has on beamforming results is illustrated with measurements of the freefield fan operating in stall conditions with a flow rate coefficient of $\Phi = 0.105$. As was shown in section 3.2.2, at this operating point, sources rotating at different speeds can be detected using the RSD method.

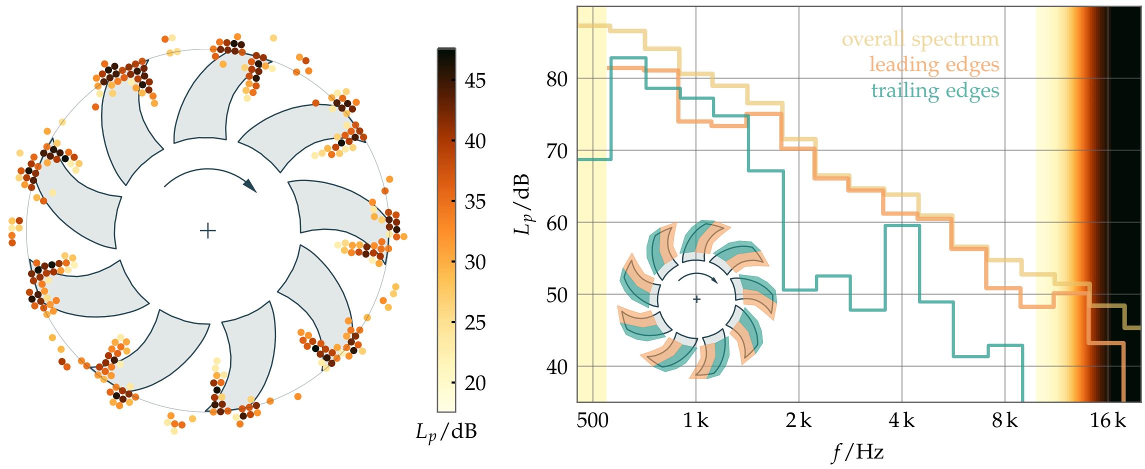

Figure 3.16. Fan in freefield, $\Phi = 0.105$, VRA-M, CLEAN-SC with CSM-M (full). Left: sound map (4 kHz third-octave band). Right: Integrated third-octave band spectra of leading and trailing edges. Values in shaded frequency ranges not reliable.

In Figure 3.16, the 4 kHz CLEAN-SC sound map and integrated spectra calculated in the mode domain – but without DREF-M – are shown. For the most part of the spectrum, the dominant sources can be found at the leading edges. At 4 kHz, the trailing edges of the blade tips are detected to contribute considerably to the noise generation as well.

In Fig. 3.17, the data is evaluated using the same processing, but with the DREF-M method applied to the CSM prior to beamforming. This leads to an overall decrease of the detected levels from about 15 dB for higher third-octave bands to about 25 dB for lower frequencies. In the 4 kHz sound map, the leading edge region is dominant for noise generation. With the removal of rotation noise, sound radiation from the blade tips is not as prominent any more. This indicates the existence of noise generating mechanisms at the tip region which do not rotate at the same rate as the fan, as is the case with the rotating stall phenomenon. Without

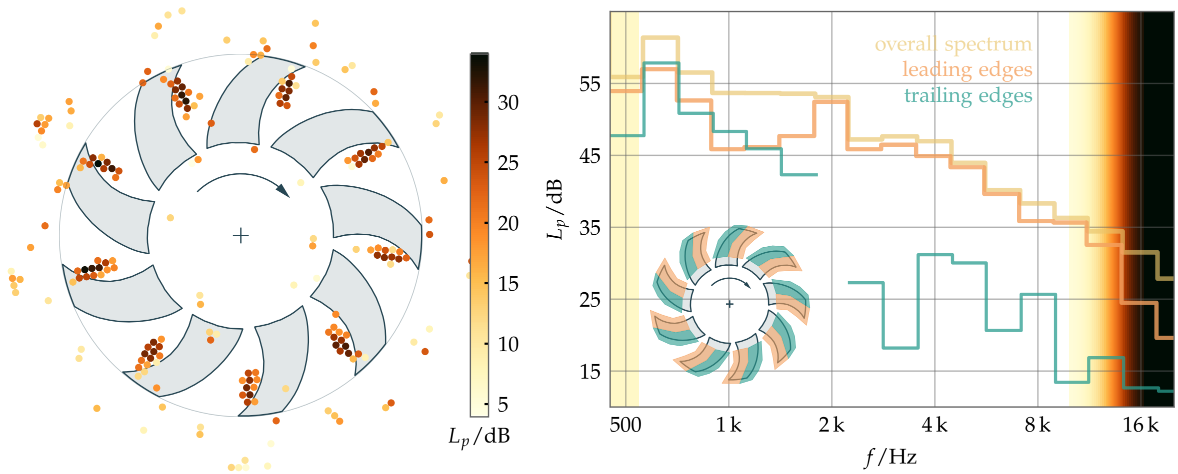

Figure 3.17. Fan in freefield, $\Phi = 0.105$, VRA-M, CLEAN-SC with CSM-M (DREF-M). Left: sound map (4 kHz third-octave band). Right: Integrated third-octave band spectra of leading and trailing edges. Values in shaded frequency ranges not reliable.

removal by DREF-M, any rotation noise is added as ring to the sources rotating with the speed of the fan, visibly raising the blade tip noise to relevant levels.

Spectra reconstruction after rotational speed separation: ducted fan

The separation of spectral features rotating at different speeds is demonstrated with the help of the ducted fan measurement. Figure 3.18 shows the spectral characteristics for the (a) stationary case and (b) rotor-synchronously rotated case. The unfiltered spectra (orange lines) can also be found in Fig. 3.7 at $f_{\mathrm{rot}}/f_{\mathrm{rot,rotor}} = 0$ and $f_{\mathrm{rot}}/f_{\mathrm{rot,rotor}} = 1$ respectively. A corresponding f_{rot}-f diagram with DREF-M-filtered spectra is shown in appendix section F.3.

In both the stationary and the rotated case, de-noising with DREF-M considerably decreases the levels, with up to 15 dB for broadband components. In general, the tones at the BPFs (Fig. 3.18a) and VPFs (Fig. 3.18b) remain at higher levels. In this aspect, the stationary results are similar to the rotor-locked components in the cyclostationary analysis done by Behn et al. [70]. However, further tonal components present in that study (namely between 1.4 kHz and 1.7 kHz) are not found here, while the broader peak at 1.3 kHz, which remains at a high level after de-noising, is not found to be significant by the cyclostationary processing. A possible interpretation is that the former are caused by sources rotating at different rates, whereas the latter indicates a non-rotating source with significant stochastic signal content.

The spectrum for the virtually rotated case (Fig. 3.18b) exhibits significantly more tonal components than the stationary spectrum, which become more prominent with DREF-M application. These tones appear in a regular fashion with a distance of 50 Hz. This corresponds to the rotor speed, indicating modes carrying stationary spectral components or artefacts, which become visible with the shifting of the modes for the virtual rotation synchronous to the rotor.

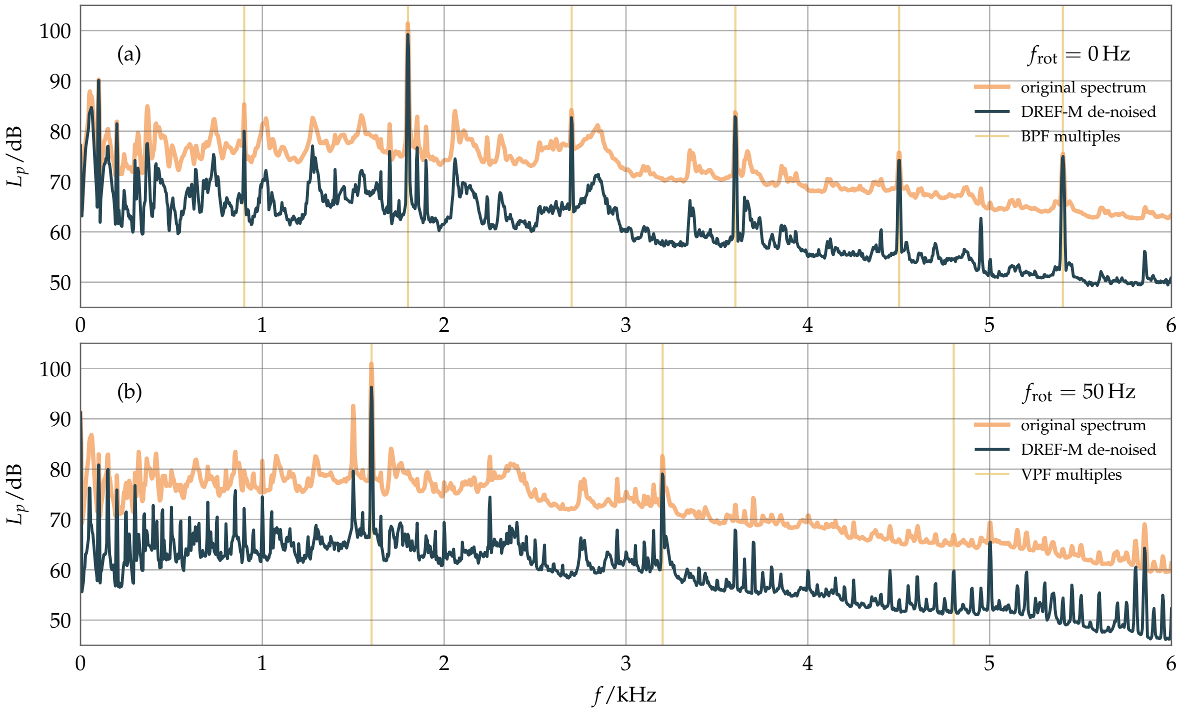

Figure 3.18. Spectra of the ducted fan, (a) in the stationary reference frame and (b) synchronously rotating with the fan (VRA-M), without and with de-noising using the DREF-M method.

It was mentioned in section 3.1.5 that the BPF/VPF tones are carried by modes that rotate, but at a different speed as the fan. Thus, the remaining high levels of these tones after DREF-M application appear to somewhat contradict the claim that the diagonal reconstruction in the mode domain removes the contribution of sources which rotate at different speeds. However, rotating noise is only removed if the signal content in question is uncorrelated noise. Tapken et al. [63] pointed out that for tonal noise components, the modes are correlated with each other. Thus, these components are also present in the CSM's off-diagonal entries, leading to their perseverance after diagonal reconstruction. A possible strategy for reducing these tones could lie in combining the DREF-M method and the cyclostationary analysis, as the latter can also be used for revealing the broadband components by subtracting the tonal parts [70, 71].

Spectra reconstruction after rotational speed separation: freefield fan

In Fig. 3.19, the freefield fan is evaluated in a similar fashion as the ducted fan in Fig. 3.7, plotting the spectra for different rotational speeds on top of each other. For the two operation points, the f_{rot}-f diagrams are calculated both without and with the DREF-M de-noising technique.

The range of evaluated rotational speeds was chosen to not be as extensive as for the ducted fan, since the sound field here is not expected to have such an elaborate modal structure. In fact, the f_{rot}-f diagrams computed using the full CSM (Fig. 3.19a & c) do not indicate any rotational speeds being present in the data set aside from $f_{\mathrm{rot}} = 0$, from whose zero-frequency multiple modal lines emerge. This indicates an unequal loading of the microphones, e. g. due to reflections or uneven flow conditions.

If the DREF-M method for the reduction of rotation noise is applied at the different rotational speeds, visibly more energy remains in the spectra at $f_{\mathrm{rot}} = 0$ and $f_{\mathrm{rot}} = f_{\mathrm{rot,rotor}}$ (Fig. 3.19b & d). This shows that in combination with the removal of rotation noise, the f_{rot}-f visualization can be used to reveal rotational speeds of broadband sources as well, even though at lower frequencies, the number of averages for the CSM-M calculation is not sufficiently high to let DREF-M “see” through the rotation noise.

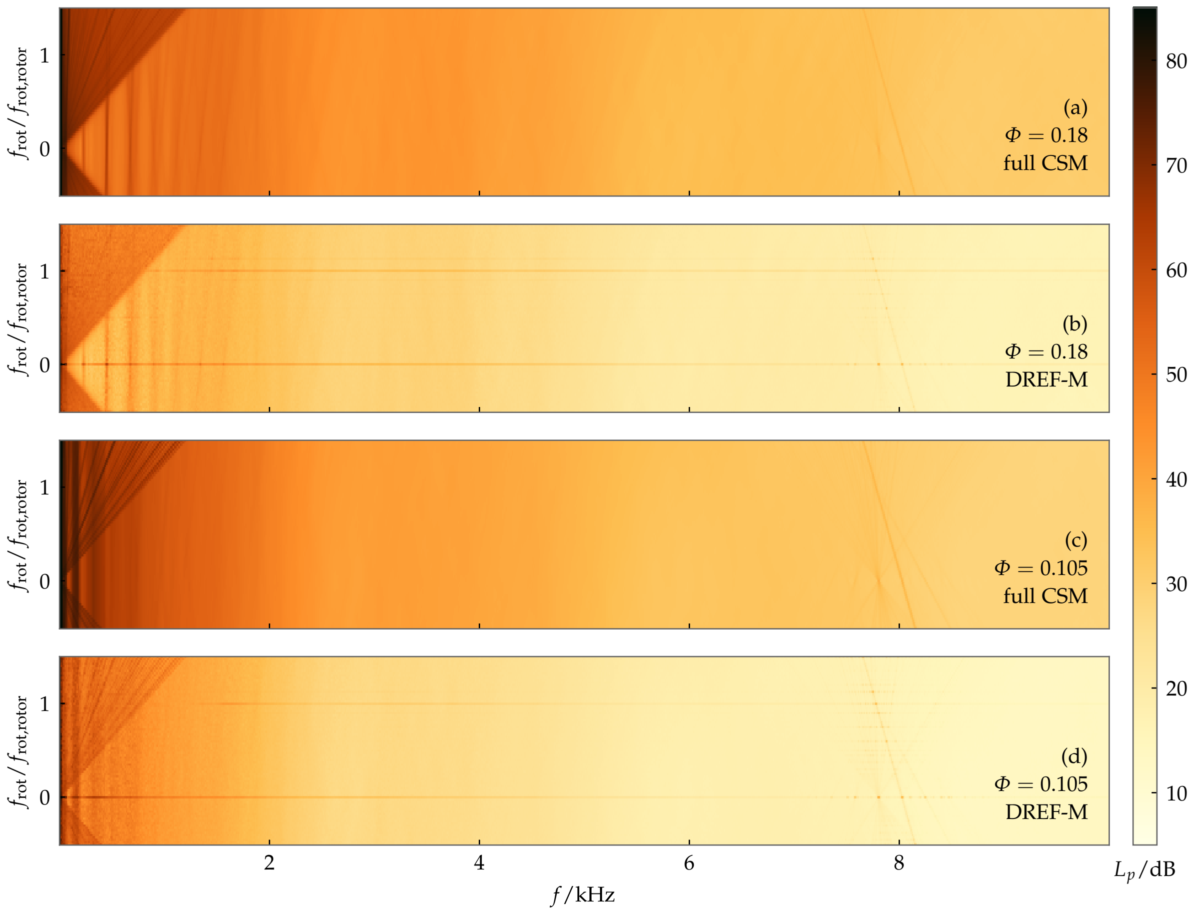

Figure 3.19. f_{rot}-f diagrams of the freefield fan at two different operating points and without & with CSM diagonal reconstruction in the mode domain.

The components rotating at a lower speed that have been detectable with the RSD method (as shown in Fig. 3.11) cannot be seen in the corresponding Fig. 3.19d here. This is to be expected, however, since the observed transient stall phenomena appear only sporadically and do not rotate at a perfectly constant speed.

4. Conclusion

Rotating machines are a normal part of our everyday lives, as is the noise they generate. Ongoing efforts to reduce the nuisances they cause require effective diagnostic tools. The virtual rotating array (VRA) method has emerged in recent years as a powerful technique for detecting and characterizing sound sources that move synchronously to rotating components. In the preceding chapters, this technique as well as other methods and data processing steps related to it were substantially advanced and then examined for their applicability. The essence of the findings shall be summarized in the following by answering the initial research questions and providing an outlook on their potential for application and further development.

What are the conditions under which the virtual rotating array method is suitable for observing rotating sources?

The catalog of rotating array methods has been extended by a formulation in the mode-time domain via the VRA-M method. It implicitly takes into account the entirety of the array signals when synthesizing a signal at a virtual sensor position, while the classic VRA-S formulation with linear interpolation only uses two microphones for this. With the formulation in the time domain, VRA-M is also capable of handling non-constant rotational speeds in the data, which is not readily possible with VRA formulated in the mode-frequency domain.

Both the VRA-S and VRA-M methods were examined with respect to application constraints regarding source location, number of array microphones, and rotational speed variation. Method performance evaluations were done based on sound maps and cross-spectral matrix coherence. It was shown that VRA-M is generally applicable in a wider frequency range than VRA-S. Furthermore, the limitations of the method were observed to be predictable by relative wavelength considerations and depend on the source positions and the number of microphones. A variation of the rotational speed was found to have no significant impact on the method performance in typical scenarios.

How can occurring rotational speeds be determined on the basis of acoustic array measurement data?

With the time-dependent rotational speed detection (RSD), a novel data processing technique was introduced. Based on evaluations in the mode domain, it is possible to detect rotating phenomena emitting broadband noise purely from acoustic measurements. The applicability of the RSD was verified using data with known rotational speeds. It was demonstrated that multiple and even varying rotations can be detected and resolved in time.

The evaluation of measured data of a fan radiating into freefield has shown that, aside from stationary and permanently rotating sources, the on- and offset of transient rotating phenomena can also be revealed using the RSD method. For a sound field generated by a fan in a duct, it was shown that the rotational speeds of modes carrying tonal components can be derived from an f_{rot}-f diagram, while the RSD method is capable of discerning additional rotational speeds of broadband phenomena.

For sources with differing rotational speeds in a data set, how can their acoustic features be characterized separately?

In addition to the commonly used beamforming formulations in the spatial domain, an equivalent formulation in the mode domain was derived via a spatial Fourier transform of the steering vectors and the cross-spectral matrix (CSM). Together with a novel CSM de-noising algorithm (DREF-M), it is then possible to reduce the interfering influence of uncorrelated sources rotating at speeds different from the one of interest.

DREF-M was successfully applied to simulated and measured data, both in combination with beamforming and for pure spectrum reconstruction. It was shown that the separation of acoustic features is not easily achieved for tonal sources, but works well for broadband signals.

Outlook

With VRA-M, RSD, and DREF-M, three powerful tools are now available for the evaluation of acoustic measurements featuring rotating sound sources. Their application on existing or yet to be measured experimental data promises new and detailed insights into sound generating phenomena. One area where the application of methods such as VRA-M or RSD would be of great benefit is for monitoring or diagnostic purposes, e. g. to detect rotational speeds whose occurrence indicates undesirable phenomena or operating conditions. Future measurement setups will benefit from the ability to predict their theoretical application limits, enabling an efficient design process of array geometries adapted to the expected sources and their properties of interest.

Since many of the methods presented here operate in the mode domain, a logical continuation of this work would address ways to better resolve azimuthal modes, e. g. by using irregular microphone arrangements along with compressed-sensing approaches.

Even though the DREF method was initially developed with CSM-M de-noising in mind, it can also be applied in the spatial domain. Further research potential here lies in exploring the capabilities of this method for classic measurements of stationary objects in noisy environments and comparing it with other diagonal reconstruction methods besides DRAP.

Conversely, an investigation of the employment of different algorithms for reducing rotation noise will also prove to be of value, particularly with respect to the inclusion of tonal components. Candidates for this are other diagonal reconstruction algorithms applied to the CSM-M or a combination of DREF-M with a cyclostationary analysis.

Finally, the RSD method was introduced along with an extensive set of parameters. While the values chosen for these parameters have produced meaningful results in the cases evaluated here, a systematic study of the influence of each of these parameters would be of great value to optimize the performance of the method.

Bibliography

[1] R. P. Dougherty. "Beamforming in acoustic testing". *Aeroacoustic Measurements*. Ed. by T. J. Mueller. Berlin, Heidelberg: Springer, 2002. DOI: 10.1007/978-3-662-05058-3_2 (cited on pp. 1, 8).

[2] R. Merino-Martínez, P. Sijtsma, M. Snellen, T. Ahlefeldt, J. Antoni, C. J. Bahr, D. Blacodon, D. Ernst, A. Finez, S. Funke, T. F. Geyer, S. Haxter, G. Herold, X. Huang, W. M. Humphreys, Q. Leclère, A. Malgoezar, U. Michel, T. Padois, A. Pereira, C. Picard, E. Sarradj, H. Siller, D. G. Simons, and C. Spehr. "A review of acoustic imaging methods using phased microphone arrays". *CEAS Aeronautical Journal* 10.1 (2019). DOI: 10.1007/s13272-019-00383-4 (cited on pp. 1, 3).

[3] I. J. Sharland. "Sources of noise in axial flow fans". *Journal of Sound and Vibration* 1.3 (1964). DOI: 10.1121/1.1977649 (cited on p. 1).

[4] S. E. Wright. "The acoustic spectrum of axial flow machines". *Journal of Sound and Vibration* 45.2 (1976). DOI: 10.1016/0022-460X(76)90596-4 (cited on p. 1).

[5] R. P. Dougherty and B. E. Walker. "Virtual rotating microphone imaging of broadband fan noise". *Proceedings of the 15th AIAA/CEAS Aeroacoustics Conference*. Reston, Virigina, 2009. DOI: 10.2514/6.2009-3121 (cited on pp. 1, 13).

[6] W. Pannert and C. Maier. "Rotating beamforming – motion-compensation in the frequency domain and application of high-resolution beamforming algorithms". *Journal of Sound and Vibration* 333.7 (2014). DOI: 10.1016/j.jsv.2013.11.031 (cited on pp. 1, 14, 17).

[7] G. Herold and E. Sarradj. "Microphone array method for the characterization of rotating sound sources in axial fans". *Noise Control Engineering Journal* 63.6 (2015). DOI: 10.3397/1/376348 (cited on pp. 1, 13, 14, 17).

[8] G. Herold and E. Sarradj. "Frequency domain deconvolution for rotating sources on an axial fan". *Proceedings of the 6th Berlin Beamforming Conference*. Berlin, Germany, 2016 (cited on pp. 1, 14, 36).

[9] F. J. Zenger, G. Herold, S. Becker, and E. Sarradj. "Sound source localization on an axial fan at different operating points". *Experiments in Fluids* 57.8 (2016). DOI: 10.1007/s00348-016-2223-8 (cited on pp. 1, 14, 26, 27).

[10] F. Zenger, G. Herold, and S. Becker. "Acoustic characterization of forward- and backward-skewed axial fans under increased inflow turbulence". *AIAA Journal* 55.4 (2017). DOI: 10.2514/1.J055383 (cited on pp. 1, 14, 34).

[11] G. Herold, F. Zenger, and E. Sarradj. "Influence of blade skew on axial fan component noise". *International Journal of Aeroacoustics* 16.4-5 (2017). DOI: 10.1177/1475472X17718740 (cited on pp. 1, 14, 25–27, 34, 35, 41).

[12] F. J. Krömer. "Sound emission of low-pressure axial fans under distorted inflow conditions". PhD thesis. Friedrich-Alexander-Universität Erlangen-Nürnberg (FAU), 2018. DOI: 10.25593/978-3-96147-089-1 (cited on p. 1).

[13] G. Herold and E. Sarradj. "Detection and visualization of fan noise sources and excited modes in a circular duct". *Proceedings of the 25th AIAA/CEAS Aeroacoustics Conference*. Delft, Netherlands, 2019. DOI: 10.2514/6.2019-2441 (cited on pp. 1, 14, 36, 37).

[14] G. Herold, C. Ocker, E. Sarradj, and W. Pannert. "A comparison of microphone array methods for the characterization of rotating sound sources". *Proceedings of the 7th Berlin Beamforming Conference*. Berlin, Germany, 2018 (cited on pp. 1, 12, 14, 18, 30).

[15] C. Ocker, G. Herold, F. Krömer, W. Pannert, E. Sarradj, and S. Becker. "A comparison of frequency-domain microphone array methods for the characterization of rotating broadband noise sources". *Acta Acustica united with Acustica* 105.1 (2019). DOI: 10.3813/aaa.919288 (cited on pp. 1, 14).

[16] M. Lehmann, C. Spehr, M. Schneider, and D. Ernst. "Investigations on limitations of the virtual rotating array method". *Proceedings of the 8th Berlin Beamforming Conference*. Berlin, Germany, 2020 (cited on pp. 1, 15, 30).

[17] Q. Leclère, A. Pereira, C. Bailly, J. Antoni, and C. Picard. "A unified formalism for acoustic imaging based on microphone array measurements". *International Journal of Aeroacoustics* 16.4-5 (2017). DOI: 10.1177/1475472X17718883 (cited on pp. 3, 12).

[18] D. H. Johnson and D. E. Dudgeon. *Array Signal Processing: Concepts and Techniques*. Englewood Cliffs, New Jersey: Prentice Hall, 1993 (cited on p. 3).

[19] M. Heckl and H. A. Müller. *Taschenbuch der Technischen Akustik*. Berlin, Heidelberg: Springer, 1994. DOI: 10.1007/978-3-642-97356-7 (cited on p. 4).

[20] E. Sarradj. "Three-dimensional acoustic source mapping with different beamforming steering vector formulations". *Advances in Acoustics and Vibration* 2012 (2012). DOI: 10.1155/2012/292695 (cited on pp. 4, 5).

[21] R. B. Randall. "Spectral Analysis and Correlation". *Handbook of Signal Processing in Acoustics*. Ed. by D. Havelock, S. Kuwano, and M. Vorländer. New York: Springer Science+Business Media, 2008. DOI: 10.1007/978-0-387-30441-0 (cited on pp. 5, 36).

[22] A. V. Oppenheim, R. W. Schafer, and J. R. Buck. *Discrete-Time Signal Processing*. 2nd ed. Upper Saddle River, New Jersey: Prentice Hall, 1999 (cited on pp. 6, 15).

[23] M. Behn, R. Kisler, and U. Tapken. "Efficient azimuthal mode analysis using compressed sensing". *Proceedings of the 22nd AIAA/CEAS Aeroacoustics Conference*. Lyon, France, 2016. DOI: 10.2514/6.2016-3038 (cited on p. 7).

[24] J. S. Bendat and A. G. Piersol. *Random Data: Analysis and Measurement Procedures*. 4th ed. New York, USA: John Wiley & Sons, 2010 (cited on p. 8).

[25] P. Stoica and R. Moses. *Spectral analysis of signals*. Upper Saddle River, New Jersey: Prentice Hall, 2005 (cited on pp. 8, 20).

[26] P. Daniell. "Discussion on 'On the theoretical specification and sampling properties of autocorrelated time-series'". *Journal of the Royal Statistical Society* 8 (1946). DOI: 10.1111/j.2517-617X.1946.tb00117.x (cited on p. 8).

[27] P. D. Welch. "The use of fast Fourier transform for the estimation of power spectra: a method based on time averaging over short, modified periodograms". *IEEE Transactions on Audio and Electroacoustics* 15.2 (1967). DOI: 10.1109/TAU.1967.1161901 (cited on p. 8).

[28] C. Ocker and W. Pannert. "Calculation of the cross spectral matrix with Daniell's method and application to acoustical beamforming". *Applied Acoustics* 120 (2017). DOI: 10.1016/j.apacoust.2017.01.011 (cited on p. 8).

[29] A. Dinsenmeyer, J. Antoni, Q. Leclère, and A. Pereira. "A probabilistic approach for cross-spectral matrix denoising: Benchmarking with some recent methods". *The Journal of the Acoustical Society of America* 147.5 (2020). DOI: 10.1121/10.0001098 (cited on p. 8).

[30] J. Hald. "Removal of incoherent noise from an averaged cross-spectral matrix". *The Journal of the Acoustical Society of America* 142.2 (2017). DOI: 10.1121/1.4997923 (cited on p. 9).

[31] R. P. Dougherty. "Cross spectral matrix diagonal optimization". *Proceedings of the 6th Berlin Beamforming Conference*. Berlin, Germany, 2016 (cited on p. 9).

[32] A. Finez, A. Pereira, and Q. Leclère. "Broadband mode decomposition of ducted fan noise using cross-spectral matrix denoising". *FAN 2015 – International Conference on Fan Noise, Technology and Numerical Methods*. Lyon, France, 2015 (cited on p. 9).

[33] P. Sijtsma, A. Dinsenmeyer, J. Antoni, and Q. Leclère. "Beamforming and other methods for denoising microphone array data". *Proceedings of the 25th AIAA/CEAS Aeroacoustics Conference*. Delft, Netherlands, 2019. DOI: 10.2514/6.2019-2653 (cited on p. 9).

[34] Q. Leclère, N. Totaro, C. Pézerat, F. Chevillotte, and P. Souchotte. "Extraction of the acoustic part of a turbulent boundary layer from wall pressure and vibration measurements". *Novem 2015 - Noise and vibration - Emerging technologies*. Dubrovnik, Croatia, 2015 (cited on pp. 9, 65).

[35] J. Antoni. “Cyclostationarity by examples”. *Mechanical Systems and Signal Processing* 23.4 (2009). DOI: 10.1016/j.ymssp.2008.10.010 (cited on p. 11).

[36] T. F. Brooks and W. M. Humphreys. “A deconvolution approach for the mapping of acoustic sources (DAMAS) determined from phased microphone arrays”. *Journal of Sound and Vibration* 294 (2006). DOI: 10.1016/j.jsv.2005.12.046 (cited on p. 12).

[37] T. Yardibi, J. Li, P. Stoica, and L. N. Cattafesta. “Sparsity constrained deconvolution approaches for acoustic source mapping.” *The Journal of the Acoustical Society of America* 123.5 (2008). DOI: 10.1121/1.2896754 (cited on p. 12).

[38] G. Herold and E. Sarradj. “Performance analysis of microphone array methods”. *Journal of Sound and Vibration* 401 (2017). DOI: 10.1016/j.jsv.2017.04.030 (cited on pp. 12, 30, 31).

[39] J. Högbom. “Aperture synthesis with a non-regular distribution of interferometer baselines”. *Astronomy and Astrophysics Supplement* 15.3 (1974) (cited on p. 12).

[40] P. Sijtsma. “CLEAN based on spatial source coherence”. *International Journal of Aeroacoustics* 6.4 (2007). DOI: 10.1260/147547207783359459 (cited on p. 12).

[41] P. Sijtsma, S. Oerlemans, and H. Holthusen. “Location of rotating sources by phased array measurements”. *Proceedings of the 7th AIAA/CEAS Aeroacoustics Conference*. Maastricht, Netherlands, 2001. DOI: 10.2514/6.2001-2167 (cited on p. 12).

[42] O. Minck, N. Binder, O. Cherrier, L. Lamotte, and V. Budinger. “Fan noise analysis using a microphone array”. *Fan 2012 - International Conference on Fan Noise*. Senlis, France, 2012 (cited on p. 12).

[43] M. Debrouwere and D. Angland. “Airy pattern approximation of a phased microphone array response to a rotating point source”. *The Journal of the Acoustical Society of America* 141.2 (2017). DOI: 10.1121/1.4976068 (cited on p. 12).

[44] R. Cousson, Q. Leclère, M. A. Pallas, and M. Bérengier. “A time domain CLEAN approach for the identification of acoustic moving sources”. *Journal of Sound and Vibration* 443 (2019). DOI: 10.1016/j.jsv.2018.11.026 (cited on p. 12).

[45] N. Chu, Q. Huang, L. Yu, Y. Ning, and D. Wu. “Rotating acoustic source localization: a power propagation forward model and its high-resolution inverse methods”. *Measurement* January (2021). DOI: 10.1016/j.measurement.2021.109006 (cited on p. 12).

[46] D. L. Sutliff. “Rotating rake turbofan duct mode measurement system”. *The Journal of the Acoustical Society of America* 118.3 (2005). DOI: 10.1121/1.4779000 (cited on p. 12).

[47] S. Jekosch and E. Sarradj. “An Extension of the Virtual Rotating Array Method Using Arbitrary Microphone Configurations for the Localization of Rotating Sound Sources”. *Acoustics* 2.2 (2020). DOI: 10.3390/acoustics2020019 (cited on p. 13).

[48] G. Herold, F. Zenger, and E. Sarradj. "Analyzing noise components on skewed fans with a virtual rotating microphone array". *22nd AIAA/CEAS Aeroacoustics Conference*. Lyon, France, 2016. DOI: 10.2514/6.2016-2761 (cited on p. 14).

[49] E. T. Whittaker. "XVIII.—On the functions which are represented by the expansions of the interpolation-theory". *Proceedings of the Royal Society of Edinburgh* 35.x (1915). DOI: 10.1017/s0370164600017806 (cited on pp. 14, 61).

[50] W. Ma, H. Bao, C. Zhang, and X. Liu. "Beamforming of phased microphone array for rotating sound source localization". *Journal of Sound and Vibration* 467 (2020). DOI: 10.1016/j.jsv.2019.115064 (cited on p. 14).

[51] C. R. Lowis and P. Joseph. "A focused beamformer technique for separating rotor and stator-based broadband sources". *Proceedings of the 12th AIAA/CEAS Aeroacoustics Conference*. Cambridge, Massachusetts, 2006. DOI: 10.2514/6.2006-2710 (cited on pp. 14, 19).

[52] C. Lowis and P. Joseph. "Determining the strength of rotating broadband sources in ducts by inverse methods". *Journal of Sound and Vibration* 295.3-5 (2006). DOI: 10.1016/j.jsv.2006.01.031 (cited on p. 17).

[53] C. Ocker and W. Pannert. "Acoustic ray method derived with the concept of analogue gravity for the calculation of the sound field due to rotating sound sources". *Applied Acoustics* 168 (2020). DOI: 10.1016/j.apacoust.2020.107422 (cited on p. 17).

[54] E. Sarradj, S. Jekosch, and G. Herold. "An efficient ray tracing approach for beamforming on rotating sources in the presence of flow". *Proceedings of the 8th Berlin Beamforming Conference*. Berlin, Germany, 2020 (cited on pp. 17, 18).

[55] E. Sarradj. "A fast ray casting method for sound refraction at shear layers". *International Journal of Aeroacoustics* 16.1-2 (2017). DOI: 10.2514/6.2016-2762 (cited on p. 17).

[56] G. Herold and E. Sarradj. "Detection of rotational speeds of sound sources based on array measurements". *Applied Acoustics* 157 (2020). DOI: 10.1016/j.apacoust.2019.107002 (cited on pp. 19, 20, 24, 39, 41).

[57] G. Herold. *Microphone array benchmark b11: Rotating point sources*. 2017. DOI: 10.14279/depositonce-8460 (cited on p. 23).

[58] E. Sarradj and G. Herold. "A Python framework for microphone array data processing". *Applied Acoustics* 116 (2017). DOI: 10.1016/j.apacoust.2016.09.015 (cited on p. 23).

[59] E. Sarradj, G. Herold, S. Jekosch, A. Kujawski, and M. Czuchaj. *Acoular: v21.05*. 2021. DOI: 10.5281/zenodo.4740537 (cited on p. 23).

[60] F. E. Terman. *Radio Engineer's Handbook*. New York, London: McGraw-Hill Book Co., 1943 (cited on p. 24).

[61] Deutsches Institut für Normung e.V. *DIN EN ISO 5801:2007 - Industrieventilatoren – Leistungsmessung auf genormten Prüfständen*. 2008 (cited on p. 25).

[62] F. J. Zenger, A. Renz, M. Becher, and S. Becker. "Experimental investigation of the noise emission of axial fans under distorted inflow conditions". *Journal of Sound and Vibration* 383 (2016). DOI: 10.1016/j.jsv.2016.07.035 (cited on p. 25).

[63] U. Tapken, B. Pardowitz, and M. Behn. "Radial mode analysis of fan broadband noise". *Proceedings of the 23rd AIAA/CEAS Aeroacoustics Conference*. Denver, Colorado, 2017. DOI: 10.2514/6.2017-3715 (cited on pp. 28, 35, 36, 49).

[64] G. Herold, T. Gensch, B. Pardowitz, and E. Sarradj. "Charakterisierung von Schallquellen am Rotor im Strömungskanal mithilfe eines Mikrofonarrays". *Fortschritte der Akustik - DAGA*. München, Germany, 2018 (cited on p. 28).

[65] C. Ocker, G. Herold, F. Krömer, W. Pannert, E. Sarradj, and S. Becker. "Comparison of microphone array methods for the characterization of rotating broadband noise sources". *Proceedings of Fan 2018 - International Conference on Fan Noise, Aerodynamics, Applications and Systems*. Darmstadt, Germany, 2018 (cited on p. 30).

[66] J. M. Tyler and T. G. Sofrin. *Axial flow compressor noise studies*. Tech. rep. SAE Technical Paper 620532. 1962. DOI: 10.4271/620532 (cited on pp. 35, 38, 42).

[67] M. Behn, B. Pardowitz, and U. Tapken. "Compressed sensing based radial mode analysis of the broadband sound field in a low-speed fan test rig". *Proceedings of the 7th Berlin Beamforming Conference*. Berlin, Germany, 2018 (cited on p. 35).

[68] F. Kameier and W. Neise. "Rotating blade flow instability as a source of noise in axial turbomachines". *Journal of Sound and Vibration* 203.5 (1997). DOI: 10.1006/jsvi.1997.0902 (cited on p. 41).

[69] M. Inoue, S. Yoshida, K. Yamada, M. Kuroumaru, T. Minami, and M. Furukawa. "Effect of tip clearance on stall evolution process in a low-speed axial compressor stage". *Proceedings of the ASME Turbo Expo 2004*. Vol. 5 A. Vienna, Austria, 2004. DOI: 10.1115/gt2004-53354 (cited on p. 41).

[70] M. Behn, B. Pardowitz, and U. Tapken. "Separation of tonal and broadband noise components by cyclostationary analysis of the modal sound field in a low-speed fan test rig". *Proceedings of Fan 2018 - International Conference on Fan Noise, Aerodynamics, Applications and Systems*. Darmstadt, Germany, 2018 (cited on pp. 48, 49).

[71] L. Grizewski, M. Behn, S. Funke, and H. A. Siller. "Cyclostationary analysis of fan noise influenced by an inflow control device". *AIAA Journal* (2021). DOI: 10.2514/1.j059493 (cited on p. 49).

[72] S. W. Rienstra and A. Hirschberg. *An Introduction to Acoustics: IWDE Report 92-06 (revised)*. Eindhoven University of Technology, Instituut Wiskundige Dienstverlening, 2004. DOI: 10.1063/1.3067395 (cited on p. 67).

List of Figures

List of Tables

List of Algorithms

A. VRA-S – Interpolation with the sinc function

An alternative to linear interpolation for synthesizing virtual signals at positions between physical sensor positions is the Whittaker-Shannon interpolation [49]. In contrast to using only two microphones immediately adjacent to the desired position, all microphones are included here. The central element of the interpolation is the sinc function:

$$\mathrm{sinc}(\mathrm{x}) \equiv \begin{cases} \frac{\sin \pi x}{\pi x} & \text{for } x \neq 0 \\ 1 & \text{for } x = 0 \end{cases} \tag{A.1}$$

The formulation of the virtual rotation in the spatial domain (see also Eq. (1.27)) is:

$$p_{\mathrm{rot}}(l_{\circlearrowleft}, t) = p(l_{\circlearrowleft} + M \cdot \frac{\varphi(t)}{2\pi}, t) \; . \tag{A.2}$$

To obtain signals for virtual microphones also between the physical sensor positions, the following weighted interpolation is done using *all* signals:

$$p_{\mathrm{rot}}(l_{\circlearrowleft}, t) = \boldsymbol{w}^{\mathrm{T}} \cdot \boldsymbol{p}(\boldsymbol{l}_{\mathrm{ind}}, t) \tag{A.3}$$

with the microphone index vector

$$\boldsymbol{l}_{\mathrm{ind}}(t) = \begin{pmatrix} \left\lfloor l_{\circlearrowleft} - \frac{M}{2} + M \cdot \frac{\varphi(t)}{2\pi} \right\rfloor \\ \vdots \\ \left\lfloor l_{\circlearrowleft} + M \cdot \frac{\varphi(t)}{2\pi} \right\rfloor \\ \vdots \\ \left\lfloor l_{\circlearrowleft} + \frac{M}{2} - 1 + M \cdot \frac{\varphi(t)}{2\pi} \right\rfloor \end{pmatrix} \mod M \; . \tag{A.4}$$

The vector containing the interpolation weights is calculated via:

$$\boldsymbol{w}(t) = \mathrm{sinc}\left(\begin{pmatrix} -\frac{M}{2} \\ \vdots \\ 0 \\ \vdots \\ \frac{M}{2} - 1 \end{pmatrix} + M \cdot \frac{\varphi(t)}{2\pi} - \left\lfloor M \cdot \frac{\varphi(t)}{2\pi} \right\rfloor \right) \; . \tag{A.5}$$

With this interpolation technique, the performance of VRA-S in terms of the virtual rotating signals is comparable to that of VRA-M. However, the signal processing of VRA-M with computationally efficient DFTs is considerably faster.

B. Fourier transforms of the virtual array rotation

The different formulations of the virtual rotation can be transformed into each other via Fourier transformations. In this section, this is summarized.

The transformation from spatial into the mode domain was described in Eq. (1.12):

$$p(m) = \frac{1}{\sqrt{M}} \sum_{\forall l} p(l)\, \mathrm{e}^{-\mathrm{j}\,2\pi\, m \frac{l}{M}} \ . \tag{B.1}$$

Furthermore, the transformation from time to frequency domain is done via Eq. (1.6):

$$p(f) = \frac{1}{\sqrt{N_\mathrm{s}}} \sum_{\forall t} p(t) \mathrm{e}^{-\mathrm{j}\,2\pi f \frac{t}{N_\mathrm{s}}} \ , \tag{B.2}$$

with the sample number t and the frequency index f. The stationary frame of reference is indicated by index $_{⏻}$ and the rotating frame of reference by index $_{\circlearrowleft}$. The **virtual rotation in space and time** formulation (see Eq. (1.27)) is:

$$\boxed{p_\mathrm{rot}(l_{\circlearrowleft}, t) = p(l_{⏻} + M \cdot \frac{1}{2\pi}\varphi(t), t)} \tag{B.3}$$

or, in case of constant rotational speed with $\varphi(t) = 2\pi f_\mathrm{rot} \cdot t$:

$$\boxed{p_\mathrm{rot}(l_{\circlearrowleft}, t) = p(l_{⏻} + t \cdot M \cdot f_\mathrm{rot}, t)} \tag{B.4}$$

Substituting of Eq. (B.4) in Eq. (B.1) yields

$$p_\mathrm{rot}(m, t) = \frac{1}{\sqrt{M}} \sum_{\forall l} p(l_{⏻} + t \cdot M \cdot f_\mathrm{rot}, t)\, \mathrm{e}^{-\mathrm{j}\,2\pi\, m \frac{l_{⏻}}{M}} \tag{B.5}$$

Substitution of the rotating microphone position $l_{\circlearrowleft}$ with the stationary position $l_{⏻}$ shifted according to the rotational speed by $t \cdot M \cdot f_\mathrm{rot}$:

$$l_{\circlearrowleft} = l_{⏻} + t \cdot M \cdot f_\mathrm{rot} \quad \Rightarrow \quad l_{⏻} = l_{\circlearrowleft} - t \cdot M \cdot f_\mathrm{rot} \tag{B.6}$$

Inserting of (B.6) into (B.5):

$$\begin{aligned} p_\mathrm{rot}(m, t) &= \frac{1}{\sqrt{M}} \sum_{\forall l} p(l_{\circlearrowleft}, t)\, \mathrm{e}^{-\mathrm{j}\,2\pi\, m \frac{1}{M}(l_{\circlearrowleft} - t\, M\, f_\mathrm{rot})} \\ &= \mathrm{e}^{\mathrm{j}\,2\pi\, m \frac{1}{M} t\, M\, f_\mathrm{rot}} \cdot \frac{1}{\sqrt{M}} \sum_{\forall l} p(l_{\circlearrowleft}, t)\, \mathrm{e}^{-\mathrm{j}\,2\pi\, m \frac{l_{\circlearrowleft}}{M}} \end{aligned} \tag{B.7}$$

The last term containing the sum again corresponds to the formulation for the DFT in Eq. (B.1). Thus the **virtual rotation in modes and time** results to:

$$\boxed{p_{\mathrm{rot}}(m,t) = \mathrm{e}^{\mathrm{j}\,2\pi\,m\,t\,f_{\mathrm{rot}}} \cdot p(m,t)} \tag{B.8}$$

and with $\varphi(t) = 2\pi\, f_{\mathrm{rot}} \cdot t$:

$$\boxed{p_{\mathrm{rot}}(m,t) = \mathrm{e}^{\mathrm{j}\,m\,\varphi(t)} \cdot p(m,t)} \tag{B.9}$$

Transformation of (B.8) into the frequency domain using Eq. (B.2) and $t = \frac{t}{f_{\mathrm{s}}}$:

$$\begin{aligned} p_{\mathrm{rot}}(m,f) &= \frac{1}{\sqrt{N_{\mathrm{s}}}} \sum_{\forall t} \mathrm{e}^{\mathrm{j}\,2\pi\,m\,\frac{t}{f_{\mathrm{s}}}\,f_{\mathrm{rot}}} \cdot p(m,t) \cdot \mathrm{e}^{-\mathrm{j}\,2\pi\,f\,\frac{t}{N_{\mathrm{s}}}} \\ &= \frac{1}{\sqrt{N_{\mathrm{s}}}} \sum_{\forall t} p(m,t)\,\mathrm{e}^{-\mathrm{j}\,2\pi\,\frac{t}{N_{\mathrm{s}}}\left(f - m\,\frac{N_{\mathrm{s}}}{f_{\mathrm{s}}}\,f_{\mathrm{rot}}\right)} \end{aligned} \tag{B.10}$$

With the definition in (B.2) and $f = \frac{f}{f_{\mathrm{s}}}\,N_{\mathrm{s}}$, this directly yields the **virtual rotation in modes and frequency**:

$$\boxed{p_{\mathrm{rot}}(m,f_{\circlearrowleft}) = p(m,f_{\text{⏻}} - m\,f_{\mathrm{rot}})} \tag{B.11}$$

The conversion from the "rotating frequency" to the stationary is given by

$$f_{\circlearrowleft} = f_{\text{⏻}} - m\,f_{\mathrm{rot}} \quad \Rightarrow \quad f_{\text{⏻}} = f_{\circlearrowleft} + m\,f_{\mathrm{rot}}\;, \tag{B.12}$$

so that the transformation from the rotating into the stationary reference frame can be done via

$$\boxed{p(m,f_{\text{⏻}}) = p(m,f_{\circlearrowleft} + m\,f_{\mathrm{rot}})}\;, \tag{B.13}$$

which corresponds to Eq. (1.45).

C. Parseval's theorem

The validity of eq. (1.14) shall be proved:

$$\sum_{\forall l} p(l)\, h(l)^* \stackrel{?}{=} \sum_{\forall m} p(m)\, h(m)^* \tag{C.1}$$

With the inverse transform from the mode into the spatial domain (see also Eq. (B.1))

$$p(l) = \frac{1}{\sqrt{M}} \sum_{\forall m} p(m)\, \mathrm{e}^{\mathrm{j}\, 2\pi\, l\, \frac{m}{M}} \,. \tag{C.2}$$

the left side of (C.1) can be expanded and reformulated:

$$\begin{aligned}
\sum_{\forall l} p(l)\, h(l)^* &= \sum_{\forall l} \left(\frac{1}{\sqrt{M}} \sum_{\forall m} \left(p(m)\, \mathrm{e}^{\mathrm{j}\, 2\pi\, l\, \frac{m}{M}} \right) \cdot h(l)^* \right) \\
&= \sum_{\forall m} \left(p(m) \cdot \frac{1}{\sqrt{M}} \sum_{\forall l} \left(h(l)^*\, \mathrm{e}^{\mathrm{j}\, 2\pi\, l\, \frac{m}{M}} \right) \right) \\
&= \sum_{\forall m} \left(p(m) \cdot \frac{1}{\sqrt{M}} \sum_{\forall l} \left(h(l)^* \left(\mathrm{e}^{-\mathrm{j}\, 2\pi\, l\, \frac{m}{M}} \right)^* \right) \right) \\
&= \sum_{\forall m} \left(p(m) \cdot \left(\frac{1}{\sqrt{M}} \sum_{\forall l} h(l)\, \mathrm{e}^{-\mathrm{j}\, 2\pi\, m\, \frac{l}{M}} \right)^* \right) \\
&= \sum_{\forall m} p(m)\, h(m)^*
\end{aligned} \tag{C.3}$$

$\square$

The last step results from the definition of the transformation from the spatial into the mode domain (Eq. (B.1)).

As a special case, Parseval's theorem can be evaluated with the sound pressure as the only quantity considered:

$$\sum_{\forall l} p(l)\, p(l)^* = \sum_{\forall m} p(m)\, p(m)^* \quad \Leftrightarrow \quad \sum_{\forall l} |p(l)|^2 = \sum_{\forall m} |p(m)|^2 \tag{C.4}$$

From this follows that the choice of a normalization factor $\frac{1}{\sqrt{M}}$ in the definition of the Fourier transforms leads to the sound energy contained in p remaining exactly the same after the transformation.

D. On de-noising the CSM diagonal

In this section, the performance of the newly introduced method for diagonal reconstruction through energy fitting “DREF” (see section 1.1.5) shall be compared to that of the alternating projections (DRAP) algorithm proposed by Leclère et al. [34]. The basic principle of DRAP is to set the diagonal entries of the CSM to zero in an initial step and then iteratively computing the eigenvalues of the matrix, calculating a new CSM with all negative eigenvalues set to zero and re-inserting its diagonal into the original CSM.

The evaluations are done using a simulated data set with a point source emitting white noise and additional uncorrelated white noise (with a level of approximately 15 dB above that of the source) being added to all channels. The beamforming result of the ground truth is shown in Fig. D.1a for an exemplary narrow band at 4 kHz. The simulation and evaluation parameters correspond to those of the other simulated data (see tables 2.1 and 3.1).

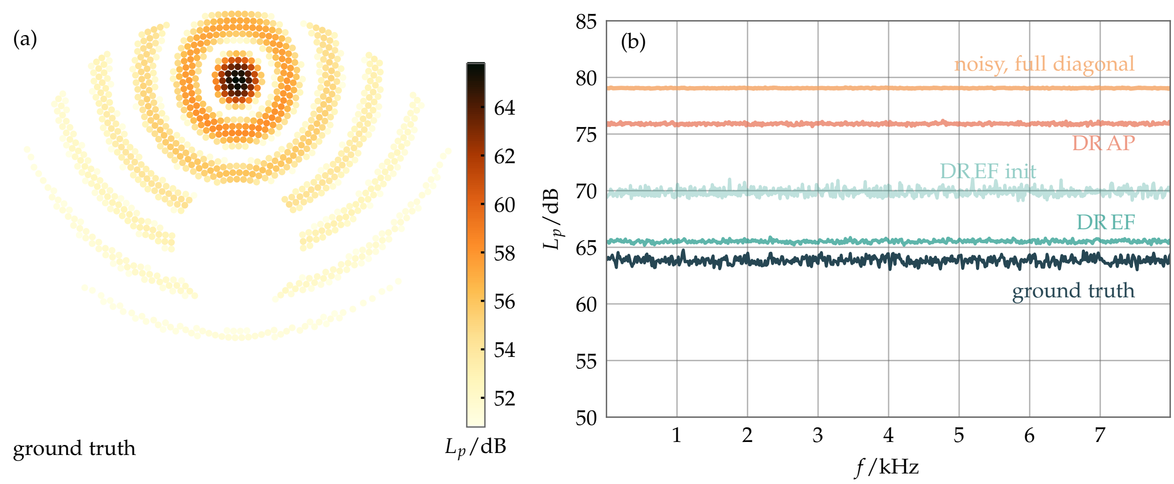

Figure D.1. Simulated data of a stationary source. (a) Sound map of the undisturbed data at 4 kHz. (b) Averaged spectra of the noisy data using different diagonal reconstruction techniques.

Figure D.2 shows sound maps of the point source with additional background noise at the microphones. A beamforming evaluation using the full CSM (Fig. D.2a) shows that the source is still visible in the sound map, however with a decreased signal-to-noise ratio (SNR). When applying the diagonal reconstruction using DRAP to the CSM (Fig. D.2b), the SNR is a little better, but not as high as when using the DREF method (Fig. D.2d), which results in a map where the SNR is comparable to the ground truth. Even when only calculating the initial DREF step without any iteration, the source emerges more clearly than when using DRAP (Fig. D.2c). In Fig. D.3a, the sound map resulting from beamforming without using the CSM diagonal is shown for comparison. As expected, the SNR is much better here as well.

When comparing the spectral characteristic (Fig. D.1b), the result is basically the same throughout the spectrum. It may be noted that when using only the initial DREF step, the spectral characteristic is not as smooth as in the other cases.

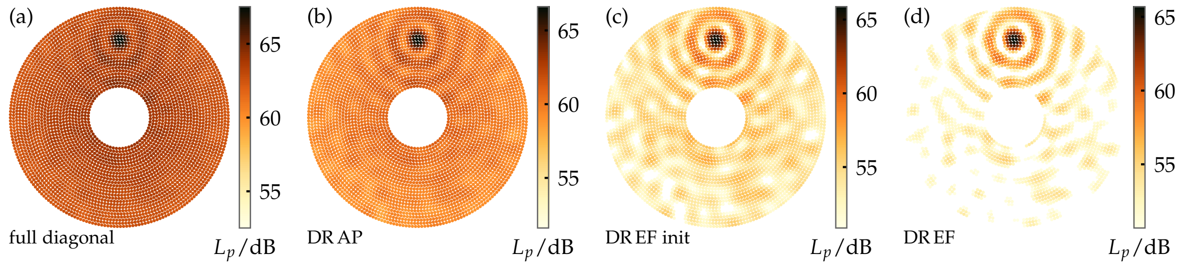

Figure D.2. Sound maps (4 kHz narrow band) of a point source with additional background noise using different diagonal reconstruction techniques.

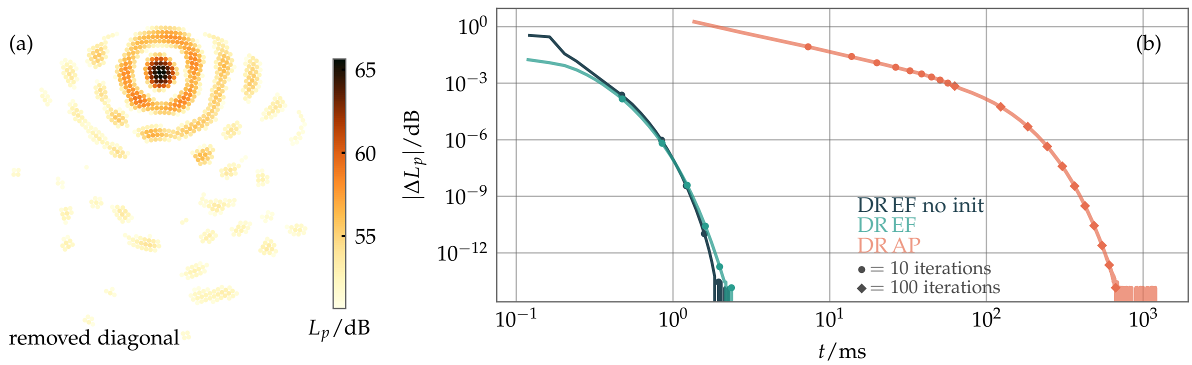

Figure D.3. (a) Sound map at 4 kHz for the point source with additional background noise, calculated omitting the CSM diagonal. (b) Convergence visualization of DREF and DRAP for the CSM diagonal at 4 kHz.

In Fig. D.3b, the convergence properties of the two methods are visualized for the CSM diagonal reconstruction at 4 kHz. The convergence is characterized here by the absolute changes of the averaged sound pressure levels in the CSM diagonal. For DREF, the cases with and without initial normalization are considered separately. All evaluations were done on the same computer within a Python framework. The displayed times are averaged over 10 runs, with durations of the individual computations being similar.

The initial normalization does not appear to have a significant influence on the DREF convergence performance. In the case evaluated here, the computation without initialization converges even a little faster in the end. Convergence is reached for DREF after about 50 iterations and 2 ms. In contrast to this, about 1100 iterations and 670 ms are necessary before the DRAP algorithm has converged, showing that this method is considerably less computationally efficient than DREF.

E. Rotating medium with axial flow

Section 1.3 describes how the sound travel times between a focal point $\boldsymbol{x}_s$ and a microphone position $\boldsymbol{x}_l$ can be calculated iteratively if a rotation is imposed on the medium in between. The method can easily be extended to consider a constant flow along the rotation axis with a velocity v_x, or written as vector:

$$\boldsymbol{v} = \begin{pmatrix} v_x \\ 0 \\ 0 \end{pmatrix} \; . \tag{E.1}$$

To derive an expression for the relative speed of sound from source to receiver, we start from the convective wave equation [72]:

$$\nabla^2 p - \frac{1}{c^2}\left(\frac{\partial}{\partial t} + \boldsymbol{v} \cdot \nabla\right)^2 p = 0 \tag{E.2}$$

For the purposes here, an ansatz of the form

$$p(\boldsymbol{x}_{sl}, t) = f\left(t - \frac{\boldsymbol{n} \cdot \boldsymbol{x}_{sl}}{c_\mathrm{p}}\right) \tag{E.3}$$

suffices, where $\boldsymbol{n}$ is any unit vector pointing in the direction of the phase velocity c_p. The vector

$$\boldsymbol{x}_{sl} \equiv \boldsymbol{x}_l(t) - \boldsymbol{x}_s(t - \Delta t_{s,l}) \tag{E.4}$$

connects the focus point with the microphone position.

With $\boldsymbol{n} \cdot \boldsymbol{n} = 1$ and $\boldsymbol{v} \cdot \boldsymbol{v} = |\boldsymbol{v}|^2$, inserting (E.3) into (E.2) yields

$$\begin{aligned} \frac{1}{{c_\mathrm{p}}^2} f'' - \frac{1}{c^2}\left(f'' - 2\,\boldsymbol{v}\,\frac{\boldsymbol{n}}{c_\mathrm{p}} f'' + \frac{|\boldsymbol{v}|^2}{{c_\mathrm{p}}^2} f''\right) &= 0 \\ \frac{1}{{c_\mathrm{p}}^2} - \frac{1}{c^2} + 2\,\boldsymbol{v}\,\frac{\boldsymbol{n}}{c^2\,c_\mathrm{p}} - \frac{|\boldsymbol{v}|^2}{c^2\,{c_\mathrm{p}}^2} &= 0 \\ {c_\mathrm{p}}^2 - 2\,\boldsymbol{v}\,\boldsymbol{n}\,c_\mathrm{p} + |\boldsymbol{v}|^2 - c^2 &= 0 \end{aligned} \tag{E.5}$$

With the relative flow velocity between focus point and microphone

$$v_\mathrm{rel} = \frac{1}{|\boldsymbol{x}_{sl}|}\,\boldsymbol{v} \cdot \boldsymbol{x}_{sl} = \boldsymbol{v}\,\boldsymbol{n} \tag{E.6}$$

and the velocity vector in Eq. (E.1), the solution of Eq. (E.5) can be written as

$$c_\mathrm{p} = v_\mathrm{rel} + \sqrt{c^2 - {v_x}^2 + {v_\mathrm{rel}}^2} \; . \tag{E.7}$$

With this, the sound travel time between the two positions can be calculated, replacing Eq. (1.41) with

$$\Delta t_{s,l} = \frac{|\boldsymbol{x}_{sl}|}{c_\mathrm{p}} = \frac{|\boldsymbol{x}_{sl}|}{v_\mathrm{rel} + \sqrt{c^2 - {v_x}^2 + {v_\mathrm{rel}}^2}} \; . \tag{E.8}$$

The correspondingly adapted iterative procedure for determining the sound travel time is shown in Algorithm E.1.

Require: $\boldsymbol{x}_l, \boldsymbol{x}_s, f_\mathrm{rot}, c, v_x$
$\boldsymbol{x}_{sl} \leftarrow \boldsymbol{x}_l - \boldsymbol{x}_s$ ▷ vector between focus point and microphone
$v_\mathrm{rel} \leftarrow v_x \cdot \Delta x_{sl1} / |\boldsymbol{x}_{sl}|$ ▷ velocity component along vector, Eq. (E.6)
$\Delta t_{s,l} \leftarrow |\boldsymbol{x}_{sl}| / (v_\mathrm{rel} + \sqrt{c^2 - {v_x}^2 + {v_\mathrm{rel}}^2})$ ▷ initialize sound travel time with Eq. (E.8)
while not converged **do**
    $\Delta\varphi_s \leftarrow 2\pi f_\mathrm{rot} \cdot \Delta t_{s,l}$ ▷ angular shift after Eq. (1.43)
    $\boldsymbol{x}_s \leftarrow$ Eq. (1.42) with $\Delta\varphi_s$ ▷ update focus point
    $\boldsymbol{x}_{sl} \leftarrow \boldsymbol{x}_l - \boldsymbol{x}_s$
    $v_\mathrm{rel} \leftarrow v_x \cdot \Delta x_1 / |\boldsymbol{x}_{sl}|$
    $\Delta t_{s,l} \leftarrow |\boldsymbol{x}_{sl}| / (v_\mathrm{rel} + \sqrt{c^2 - {v_x}^2 + {v_\mathrm{rel}}^2})$ ▷ update with Eq. (E.8)
end while
Return: $\Delta t_{s,l}$ ▷ sound travel time from $\boldsymbol{x}_s$ to $\boldsymbol{x}_l$

Algorithm E.1. Calculation of the sound travel time in a rotating medium with axial flow.

F. Further evaluation results

F.1. Better DREF-M performance with more averaging

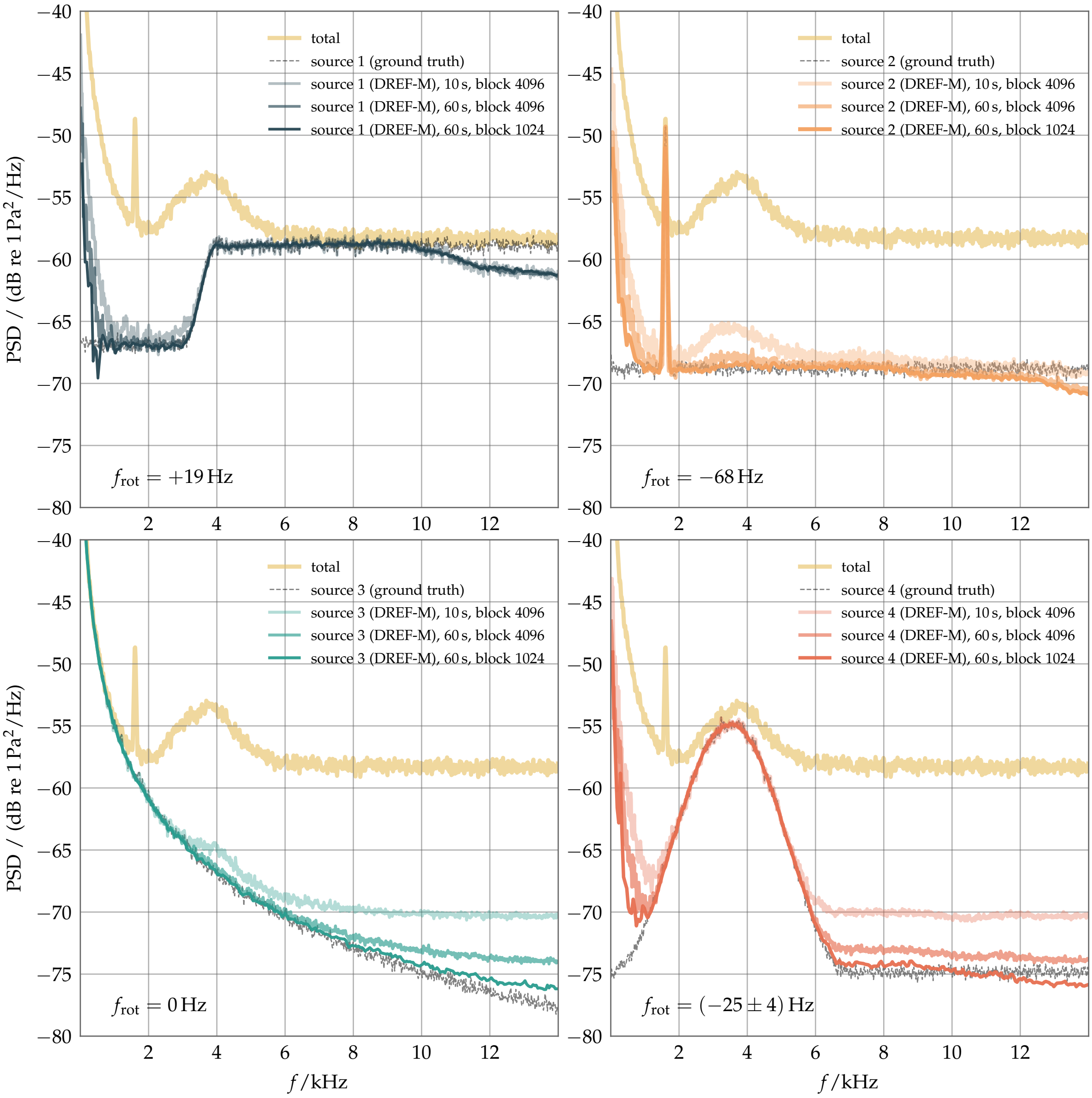

Figure F.1. Sim-2b – source-specific spectra calculated using VRA-M and DREF-M with different numbers of averagings.

Figure F.1 shows the power spectral densities of the DREF-M processed data set Sim-2b featuring four sources with different rotational speeds (see Fig. 2.2b). The respective curve colors are represented in three shades. The curve with the lightest shade in each subplot corresponds to the reconstruction of spectral characteristics as shown in Fig. 3.15. It can be seen that using six times as many averaging blocks for the CSM calculation leads to an improved signal-to-rotation-noise ratio by up to 3 dB. Decreasing the FFT block size by a factor of four (displayed by the curves with the darkest shades) also decreases the frequency resolution but leads to a further gain of about 1 dB.

With higher SNR, the degrading performance of VRA-M at higher frequencies is now also seen in the spectra of sources 2 and 4. Furthermore, at about and below 1 kHz, the spectra of sources 1, 2 and 3 exhibit an uneven characteristic, hinting at the DREF-M method being less reliable at low frequencies.

F.2. Sound maps of the freefield fan

In this section, selected evaluations of the two measurements of the freefield fan using different beamforming methods are documented in the form of sound maps at different frequencies. All de-rotations were done using the VRA-M method. The maps are calculated for third-octave bands around the indicated frequencies.

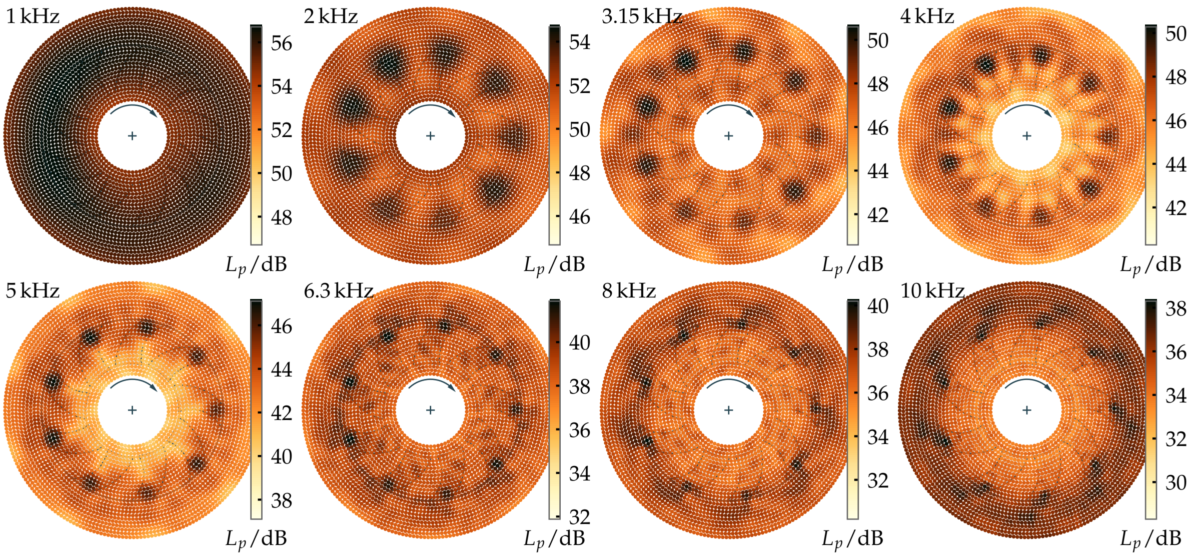

Figure F.2. Sound maps of the freefield fan at $\Phi = 0.18$, calculated using conventional frequency domain beamforming. Since the full initial CSM diagonal was used, evaluations in the spatial and mode domain are identical here.

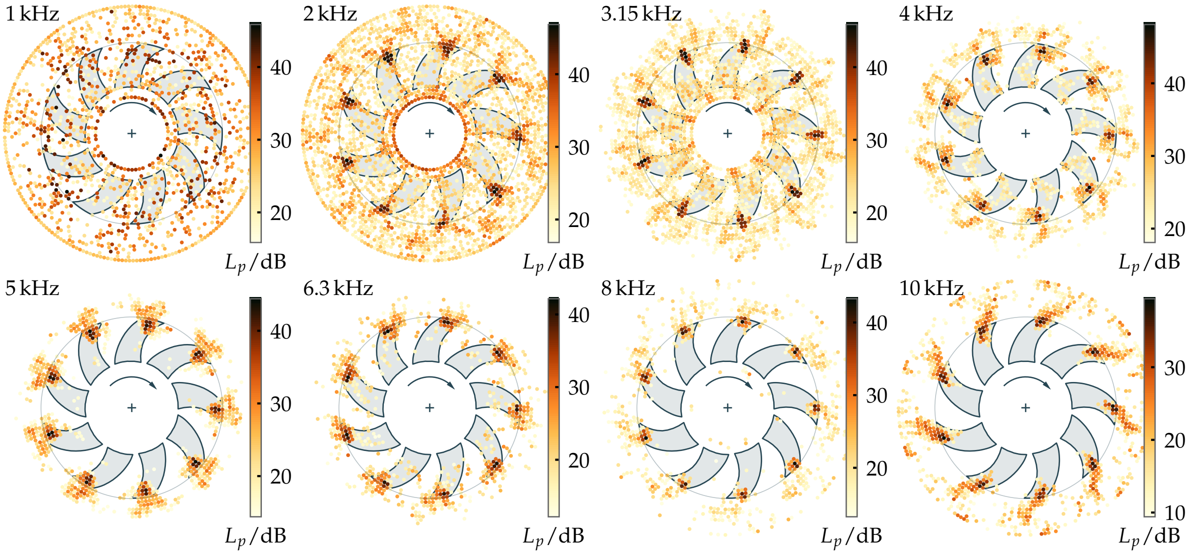

Figure F.3. Sound maps of the freefield fan at $\Phi = 0.18$, calculated using CLEAN-SC in the spatial domain with the full CSM. The map at 4 kHz corresponds to the map displayed in Fig. 3.5.

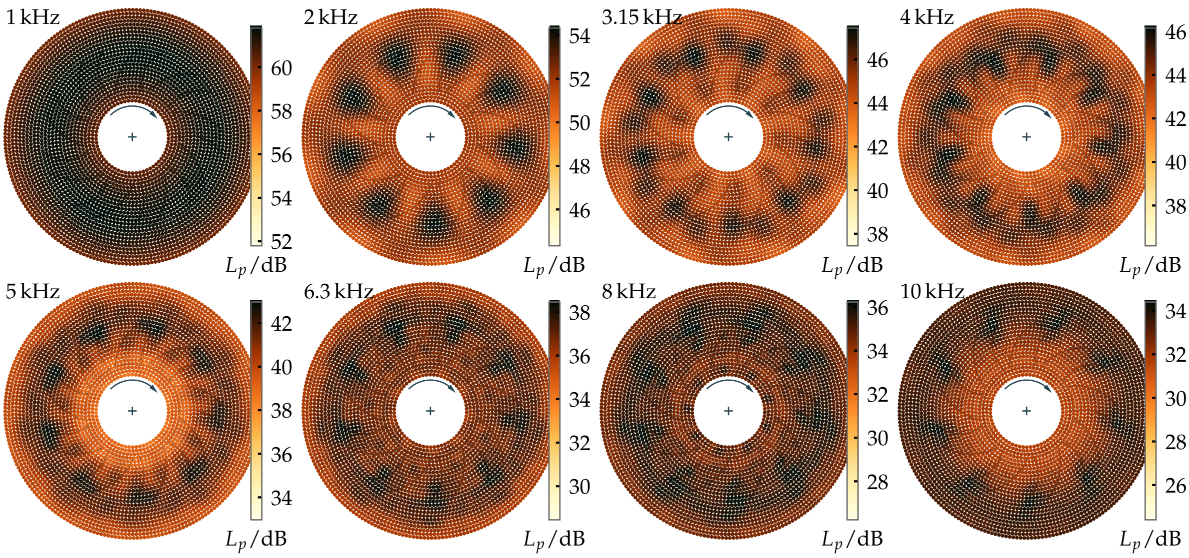

Figure F.4. Sound maps of the freefield fan at $\Phi = 0.105$, calculated using conventional frequency domain beamforming. Since the initial CSM diagonal was used, evaluations in the spatial and modal domain are identical here.

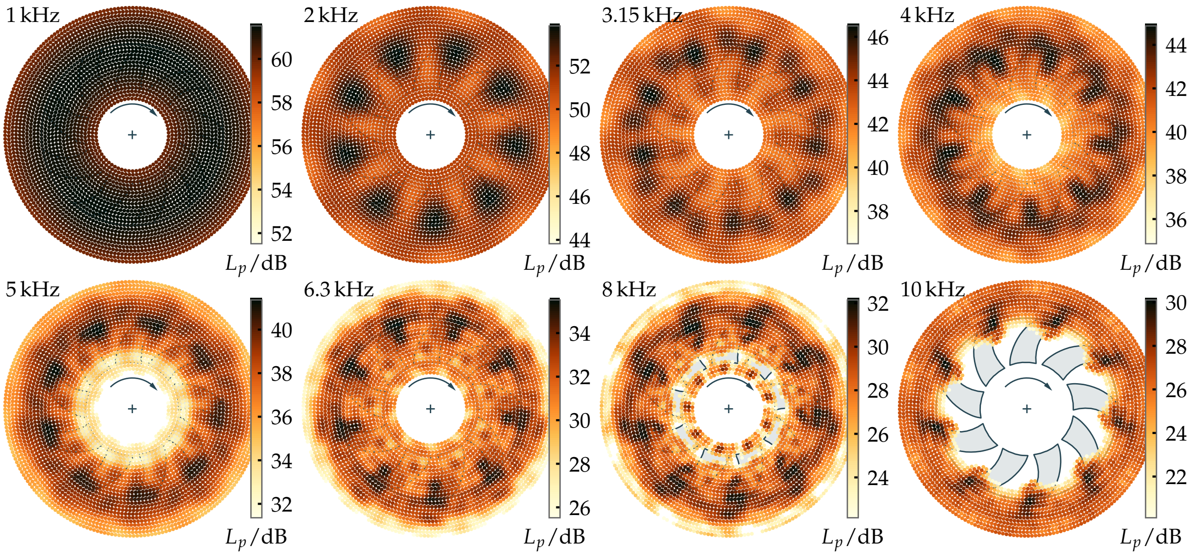

Figure F.5. Sound maps of the freefield fan at $\Phi = 0.105$, calculated using conventional frequency domain beamforming in space with the CSM de-noised by DREF-S.

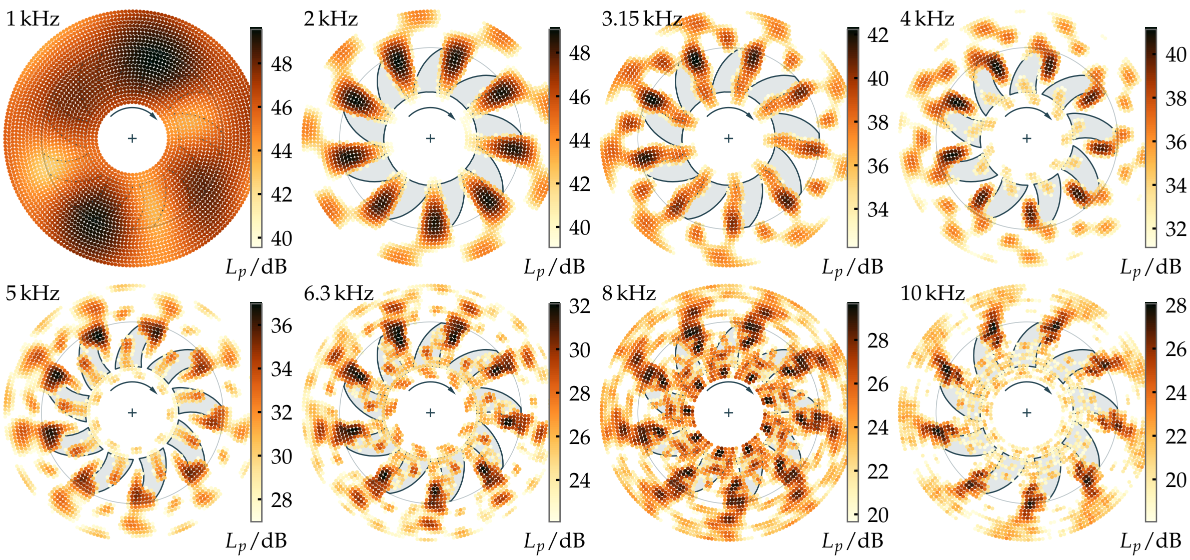

Figure F.6. Sound maps of the freefield fan at $\Phi = 0.105$, calculated using conventional frequency domain beamforming in modes with the CSM de-noised by DREF-M.

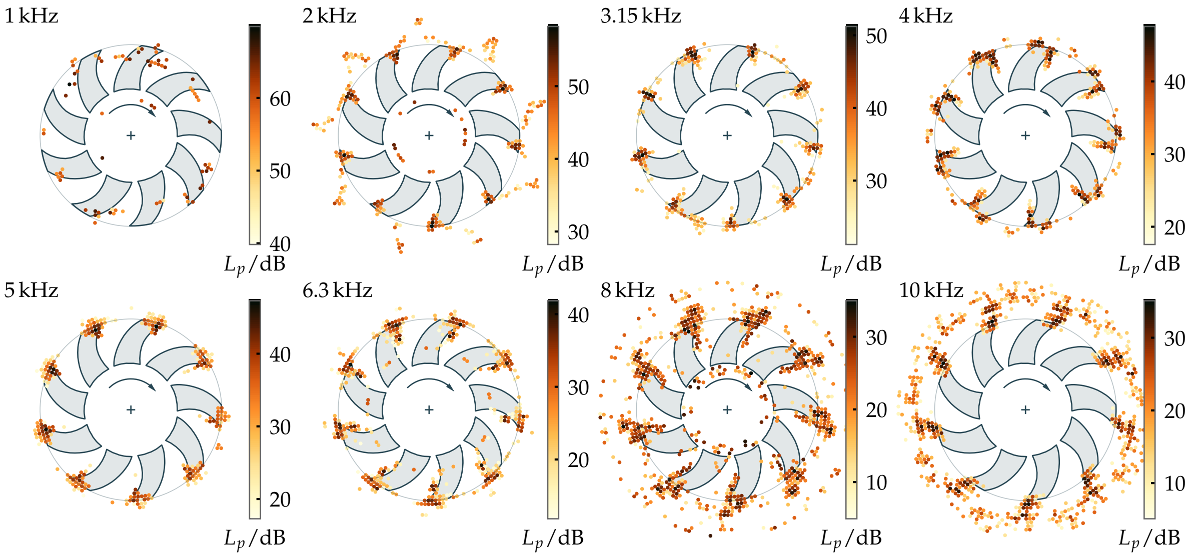

Figure F.7. Sound maps of the freefield fan at $\Phi = 0.105$, calculated using CLEAN-SC in the mode domain with the full CSM. The map at 4 kHz corresponds to the map displayed in Fig. 3.16.

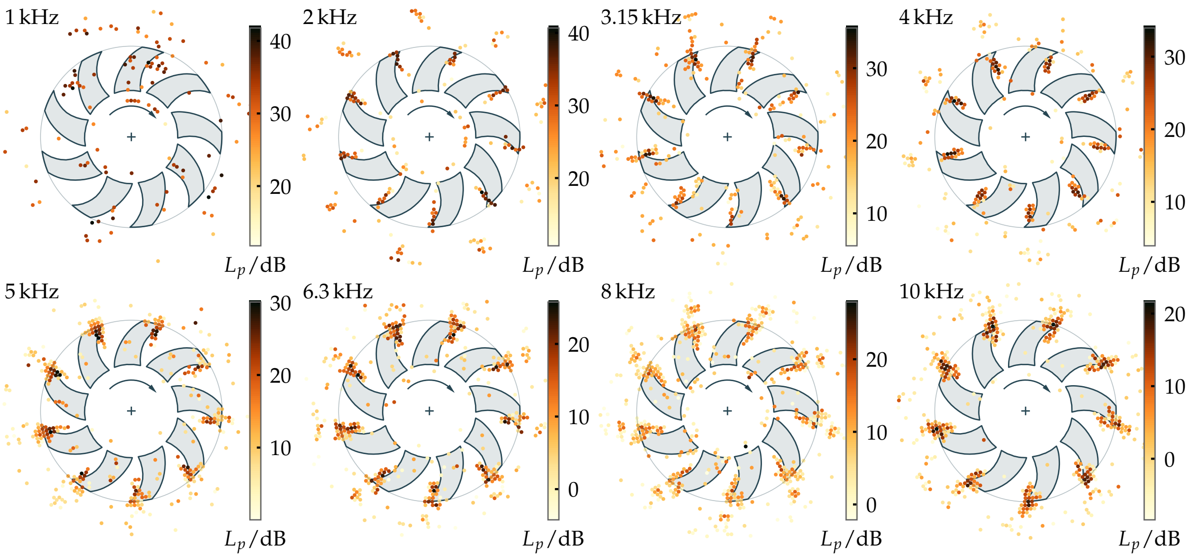

Figure F.8. Sound maps of the freefield fan at $\Phi = 0.105$, calculated using CLEAN-SC in the mode domain with the CSM de-noised using DREF-M. The map at 4 kHz corresponds to the map displayed in Fig. 3.17.

F.3. One more f_{rot}-f diagram

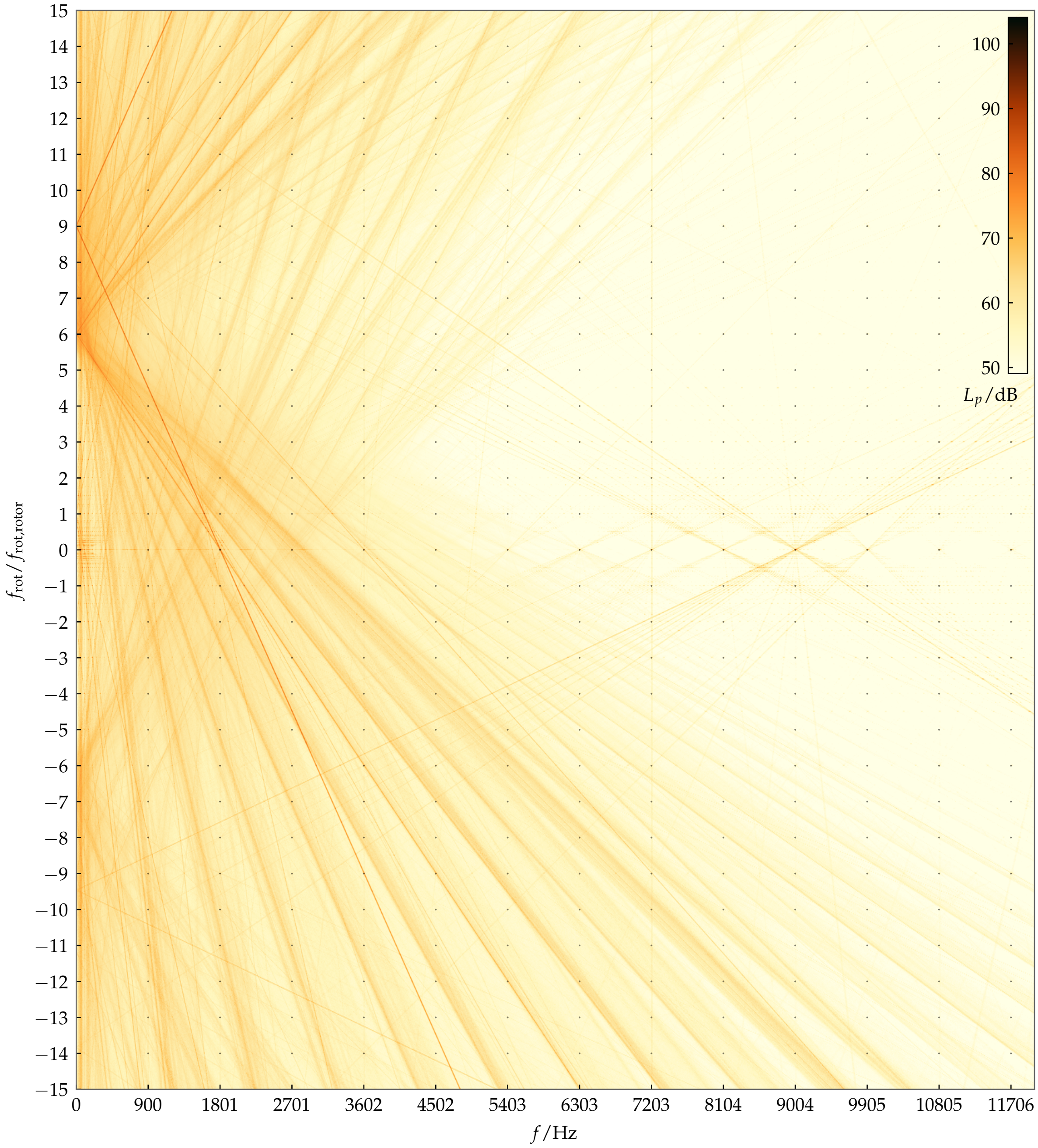

Figure F.9. f_{rot}-f diagram of the ducted fan with DREF-M.

Figure F.9 shows a visualization of the respective spectra present at different rotational speeds of the ducted fan. This evaluation is similar to the f_{rot}-f diagram in Fig. 3.7, but here, the DREF-M de-noising method is applied to the CSM at each rotational speed. It can be seen that spectral components at occurring rotational speeds are raised. The respective spectra represented in dark blue in Fig. 3.18 can be found at $f_{\mathrm{rot}} = 0$ and $f_{\mathrm{rot}} = 1 \cdot f_{\mathrm{rot,rotor}}$ respectively.